

**Optoelectronic polymer devices for biomimicking
visual response and developing neuronal interfaces
for artificial retina applications**

A thesis submitted in partial fulfillment for the degree of

Doctor of Philosophy

by

Vini Gautam



Chemistry and Physics of Materials Unit,
Jawaharlal Nehru Centre for Advanced Scientific Research
(Deemed University)
Bangalore - 560 064,
India.

FEBRUARY 2014

Dedicated to my Parents...

Declaration

I hereby declare that the matter embodied in the thesis entitled “Optoelectronic polymer devices for biomimicking visual response and developing neuronal interfaces for artificial retina applications” is the result of investigations carried out by me at the Chemistry and Physics of Materials Unit, Jawaharlal Nehru Centre for Advanced Scientific Research, Bangalore, India under the supervision of Prof. K. S. Narayan and that it has not been submitted elsewhere for the award of any degree or diploma.

In keeping with the general practice in reporting scientific observations, due acknowledgment has been made whenever the work described is based on the findings of other investigators.



Nini Gautam

Certificate

I hereby certify that the matter embodied in this thesis entitled “Optoelectronic polymer devices for biomimicking visual response and developing neuronal interfaces for artificial retina applications” has been carried out by Ms. Vini Gautam at the Chemistry and Physics of Materials Unit, Jawaharlal Nehru Centre for Advanced Scientific Research, Bangalore, India under my supervision and that it has not been submitted elsewhere for the award of any degree or diploma.

Prof. K. S. Narayan
(Research Supervisor)

Acknowledgement

I would like to acknowledge my research supervisor, Prof. K. S. Narayan for the freedom in research, encouragement to work hard and support at various difficult stages in research. I also acknowledge his family for providing me with a nice second home in Bangalore.

I thank all the faculty members in CPMU, TSU, NCU and ICMS for various course-works and scientific interactions. I also thank Prof. S. K. Sikdar (IISc, Bangalore) for a great foundation course on Neuroscience.

I would like to thank Prof. CNR Rao and Prof. MRS Rao for their encouraging and inspiring words whenever I met them personally.

I thank Prof. N. K. Dhingra and his group at NBRC, Haryana (India) for helping me learn the art and tricks related to the retina.

I thank Prof. Yael Hanein and her group at Tel Aviv University (Israel) for a fruitful collaboration on the retina work and hosting me wonderfully in Israel. Special thanks to Dr. David Rand for being a great colleague and a friend. Thanks to Sara for her helping hand with everything. Thanks to

I am grateful to Prof. Udaykumar Ranga (MBGU) and his group for discussions, and lab resources for retinal cell culture. I also thank Prof. Maneesha Inamdar for her help and discussions at various stages during my research.

I thank Dr. Prakash (Animal House, JNCASR) for his cooperation and help.

It has been a long stay for me, and I find myself lucky to have overlapped with so many people in the lab. I have got to learn a lot of stuff from them, scientifically and otherwise. I thank my lab seniors: Drs. Dinesh, Dhritiman, Arun, Shruti, Monojit, Sabyasachi, Anshuman, Balaraju, Kishore. I further thank my current lab mates Prashant, Ashar, Raaghesh, Swathi, Dhruv, Vikas, Rishav. I specially acknowledge the company of Satya

and Ravi in the lab, which has been memorable. I also thank Nishit, Vijay, Arun D., Srinidhi, Poonam, Ranbir, Matthew and Murthy for their company.

I thank Mr. A. N. Jayachandra for his help during any official or personal need. Also, I thank his family for being extremely friendly and welcoming me at their house on various occasions.

I would like to thank the staff at Admin, Purchase and Academic section. I also thank the doctors and staff at Dhanvantari and the staff at Hostel and the Hostel Mess.

I thank all my friends in JNCASR – everyone whom I played sports, had meals, hung out, chatted or danced with. Thanks to my IntPhD 2007 batchmates for all the fun we had together in our early years in JNC. Special thanks to Dhiraj – I didn't realize how such a long time passed by – I learnt a lot from you and had the best times with you during my stay in Bangalore. I will miss your company the most.

I thank my teachers with whom I attended Dance, Music and Yoga classes. My stay was more enjoyable due to these activities.

Most importantly, I thank my Mom, Dad and Brother for being the pillars of love in my life. Their constant support and encouragement has made me what I am today. I also thank my grandparents who always encourage me to reach great heights.

I thank all my other family members for being around with their love and encouragement and for always pampering me. I also thank my friends from school and college who are still bonded with me for all the fun we have whenever we meet.

Last but not the least, I thank my husband, Bishakh, and his family for their love, care and support.

List of Publications

1. "Dynamics of Bulk Polymer Heterostructure/Electrolyte Devices"
Vini Gautam, M. Bag & K. S. Narayan. *J. Phys. Chem. Lett.*, 1, 3277 - 3282 (2010).
2. "Conducting polymer coated MEAs for enhanced signal recording and stimulation".
Vini Gautam & K. S. Narayan. *Proceedings of 7th international Meeting of Substrate Integrated MEAs* (2010).
3. "Single-Pixel, Single-Layer Polymer Device as a Tri-color Sensor with Signals Mimicking Natural Photoreceptors"
Vini Gautam, M. Bag & K. S. Narayan. *J. Am. Chem. Soc.*, 133, 17942 - 17949 (2011).
Highlighted in *Laser Focus World*, "Organic Photodetectors: Single layer polymer pixel senses three colors".
4. "Organic Electronics in Aqueous Environment"
Vini Gautam and K.S. Narayan, *National Academy of Science in India* [In Press] (2012).
5. "Water gated Phospholipid - Monolayer organic field effect transistor through modified Mueller-Montal method"
K. S. Narayan, B.N. Madhushankar, Vini Gautam, P.S. Satyaprasad & Ravichandran S.
IEEE Electron Device Lett., 34, 310 - 312 (2013).
6. "A polymer optoelectronic interface provides visual cues to a blind retina"
Vini Gautam, David Rand, Yael Hanein & K. S. Narayan. *Adv. Mater.* DOI: 10.1002/adma.201304368 (2013).
7. "Polymer optoelectronic structures for retinal prosthesis"
Vini Gautam and K. S. Narayan [submitted].

List of Patents

1. "Artificial Retina Device"

K. S. Narayan, Vini Gautam, Monojit Bag. PCT/IB2010/002170.

2. "Bulk Heterojunction/Electrolyte Polymers As Novel Biocompatible Photoactive Multi Color-Sensing Technology"

K. S. Narayan, Vini Gautam, Monojit Bag. PCT/IB2012/053711.

Contents

Outline.....	v
List of Abbreviations	ix
List of Figures	xi
Chapter 1 Introduction.....	1
1.1 Conducting and semiconducting polymers	2
1.2 Photoinduced charge generation and the bulk heterojunction concept	5
1.3 Semiconducting polymer/electrolyte interface	7
1.4 Introduction to the processes in neural and visual systems.....	10
1.4.1 Origin of action potentials.....	11
1.4.2 Recording of electrical signals from nerve cells	12
1.4.3 Introduction to the retina.....	15
1.5 Approaches for Retinal prosthesis.....	20
Chapter 2 Optoelectronic Polymer Device Structures for Intelligent Sensing and Biomimicking Visual Response	25
2.1 Details of Materials, Device Fabrication and Measurement Methods	26
2.1.1 Materials and device fabrication.....	26
2.1.2 Fabrication of bilayer devices.....	28
2.1.3 Measurement of device photoresponse	28
2.1.4 Device fabrication on MEA.....	29
2.1.5 Electrical recordings from visual photoreceptors.....	30
2.2 Results – Photoinduced current measurements.....	31
2.2.1 Direction of Photoexcitation.....	32
2.2.2 Thickness dependent photocurrent response	32
2.2.3 Two-color sensing procedure	33
2.2.4 Three-color sensing using characteristic response features	38
2.2.5 Numerical representation of photocurrent profiles	39
2.2.6 Possible demosaicing logic.....	40
2.2.7 Yellow and white color detection	41
2.2.8 Multi-color Detection.....	42
2.2.9 Sensitivity and resolution.....	43

2.2.10	Response from bilayer devices	44
2.2.11	Photoresponse of biological photodetectors	45
2.2.12	Photocurrent spectra in antagonistic backgrounds	46
2.3	Results - Photocapacitance Measurements	46
2.3.1	Differential photocapacitance	47
2.3.2	Capacitance-Voltage Measurements	49
2.4	Microscopic origin of the photoinduced response.....	50
2.5	Similarities to naturally occurring photoreceptors.....	58
2.6	Summary.....	61
Chapter 3 Optoelectronic Polymer Structures for Artificial Retina		
Applications.....		63
3.1	Details of device fabrication, retina preparation and recording methods ..	65
3.1.1	Polymer coating and characterization	65
3.1.2	Retina Preparation	66
3.1.3	Multi-unit (extracellular) recordings from retina	66
3.1.4	Optical Stimulation of the BHJ/retina.....	67
3.2	Results of control experiments and retina stimulation with BHJ.....	67
3.2.1	Background and control experiments.....	68
3.2.2	Typical response of retina to BHJ photostimulation	72
3.2.3	Intensity and duration dependence of the response	76
3.2.4	Temporal resolution.....	78
3.2.5	Spatial stimulation	79
3.3	Origin of the features of retinal response to BHJ photoexcitation	80
3.4	Summary.....	83
Chapter 4 Optoelectronic Polymer Structures as Active Biocompatible		
Interfaces for Neuronal Networks.....		85
4.1	Introduction	85
4.2	Experimental Methods	88
4.2.1	Preparation of polymer-coated substrates	88
4.2.2	Ornithine/Laminin coating.....	88
4.2.3	Cell Culture Protocol	89
4.2.4	TUNEL assay protocol	90
4.2.5	Photoillumination set-up.....	91

4.2.6 Neuronal staining protocol.....	91
4.3 Results - Cytotoxicity and Biocompatibility	91
4.4 Results - Cell culture under illumination	93
4.5 Summary	98
Chapter 5 Summary and Future Perspective	101
List of References	105

Outline

Semiconducting polymers are an attractive choice as active materials for a variety of optoelectronic applications. The merits of organic semiconducting materials include facile processing routes, conformal substrates and the choice of wide range of absorption wavelengths. These materials have a unique combination of mechanical and optoelectronic properties, which offer the possibility of seamless integration of these materials with biological systems. Although these devices have been utilized for applications such as organic solar cells, oFETs and oLEDs, the utilization of optoelectronic properties of organic semiconductors for biological applications has been quite limited. This thesis focuses on the optoelectronic characteristics of organic semiconductor based polymer bulk heterojunction (BHJ) layers in contact with physiological media and the utilization of these structures as neuronal interfaces, in particular for artificial retina application.

Introduction to the basic concepts related to conjugated polymers, optoelectronic processes in organic semiconductors, and physiological properties of the visual system are presented in Chapter 1. The phenomenon of photoinduced charge carrier generation in Bulk Heterojunction (BHJ) polymer layers and the basic properties of semiconductor/electrolyte interface are discussed. The development of bioelectronic interfaces based on organic semiconductors involves an understanding of these materials properties, as well as biological phenomena and their interface characteristics. Some of the relevant topics related to signalling mechanisms and ion transport in biological systems are then discussed, specifically in relation to the visual system and the retina. The chapter covers some of the basics of electrophysiological techniques used to record action potentials from excitable cells. A brief overview of current retinal prosthetic approaches and the corresponding materials aspect and related issues are also discussed.

The interface and transport characteristics at the interface of polymer BHJ layer and physiological media are reflected in photocurrent and photocapacitance measurements across BHJ/electrolyte interfaces, which are presented in Chapter 2. The BHJ layer constituting a regio-regular poly-alkylthiophenes (rrP3AT) as donor and a naphthalene

derivative based acceptor (N2200) has been characterized. The observed results highlighted the role of bulk carrier concentration, diffusion length scales and the presence of different transport mechanisms prevalent in BHJ/electrolyte structures. The chapter further covers the specific optoelectronic features at the BHJ/electrolyte interfaces, which provide design rules for fabrication of novel, biomimicking photodetectors. The photocurrent profiles from BHJ/electrolyte structures are controlled by a combination of factors, which includes the interfacial boundary conditions, asymmetry in the electron and hole transport, and vertical distribution gradients of donor and acceptor components. The dynamics involved in the device response could be modeled with the combination of intrinsic processes and the macroscopic equivalent circuit parameters. For an optimum combination of these parameters, the device structures could be used as single-pixel color sensing elements. These device characteristics further revealed interesting similarities to the features observed in natural photosensitive systems including retinal cone cells and certain photosensitive membrane proteins. Such visual photoreceptor-type sensors operating in aqueous environment are suitable candidates to be used as stimulation elements upon interfacing with retinal neurons like the ganglion cells.

Chapter 3 presents the studies where the polymer BHJ layers with biomimicking photoresponse were interfaced with a blind retina to evoke visual cues. Degenerate mouse retinas were initially tried as the model for blind retina and patch clamp recordings from the RGCs were used to characterize the retinal response. However, utilizing an embryonic stage chick retina in the early stage of development where photoreceptors are not functional is advantageous over degenerate retina models where a large fraction of photoreceptors are still functional. The method presented in the thesis utilized coating the BHJ layer on a MEA for stimulating a developing chick retina epiretinally and recording its electrophysiological activity. Our studies demonstrated that the photoexcitation of the BHJ interface with the blind retina in physiological conditions resulted in a neuronal response in the retina, highlighting the efficacy of polymer semiconductors as artificial receptors for interfacing with the visual systems. The features of the elicited neuronal response (latency, spike rate and spike number) were observed to depend on the incident light parameters like intensity, pulse width and rate, spatial profile, and wavelength, which control the optoelectronic response of the polymer film. Interestingly, the evoked activity resembles the natural response of the retina to

light stimulation. The BHJ based stimulating platform and the methodology utilized for retinal stimulation has striking advantages over the conventional ways of retinal stimulation reported previously.

The Fourth chapter of the thesis discusses the biocompatibility and utilization of BHJ/electrolyte structures as smart interfaces for modifying neuronal growth patterns. The biocompatibility has been studied by studying the growth of dissociated retinal cell culture on the BHJ surfaces for over 10 days *in vitro* and quantifying the cell apoptosis using TUNEL assay. The BHJ surfaces are found to be non-cytotoxic and biocompatible to the retinal cells. Further, upon photoillumination of the BHJ surfaces during the cell culture period, it was observed that the photoelectric signals at the BHJ/EI interface modify the growth of retinal neurons and can be utilized to study the neuronal networks *in vitro*. The last chapter of the thesis covers the summary, future prospects and possible future directions of the work presented in this thesis.

List of Abbreviations

I_{ph}	Photocurrent
V_{ph}	Photovoltage
BHJ	Bulk Hetrojunction
EI	Aqueous electrolyte
cGMP	Cyclic Guanosine Monophosphate
RGC	Retinal Ganglion Cell
Aq	Aqueous
C	Capacitance
KCl	Potassium Chloride
MEA	Multi Electrode Array or Micro Electrode Array
ITO	Indium doped Tin Oxide
OLED	Organic Light Emitting Diode
OFET	Organic Field Effect Transistor
NIR	Near Infrared
bR	Bacteriorhodopsin
ACSF	Artificial Cerebospinal Fluid
PBS	Phosphate Buffer Saline
PFA	Paraformaldehyde
BSA	Bovine Serum Albumin
DIV	Days in Vitro
TUNEL	terminal deoxynucleotidyl transferase-mediated dUTP nick end-labeling

List of Figures

- Figure 1.1** Schematic showing various possible bioelectronic interfaces based on conjugated materials..... 2
- Figure 1.2** Chemical structures of some important conjugated polymers. 3
- Figure 1.3** Schematic of a donor/acceptor interface showing the processes in a BHJ device..... 7
- Figure 1.4** Depiction of a donor/acceptor interface through energy levels, the photoexcitation of donor and charge diffusion towards electrodes. 7
- Figure 1.5.** Schematic showing the behavior of space charge capacitances of an n-type semiconductor as a function of bias. C_{sc} is the space charge capacity of the semiconductor, C_H is the Helmholtz layer capacitance, C_d is the capacitance of the diffuse layer of charges in the electrolyte and C_T is the total capacitance. E_{fb} is the flat band potential of the semiconductor and E is the applied bias. AL, DL and DDL represent the accumulation, depletion and deep depletion regimes of the space charge capacitance respectively. Redrawn with permission from ⁵⁶. 8
- Figure 1.6.** Schematic showing the space charge layers in an n-type semiconductor in contact with an electrolyte. (a) Distribution of charge carriers; (b) Course of band edges (c) Course of electric potential. Redrawn with permission from 56. 9
- Figure 1.7** A typical Nerve Cell. (a) Basic Structure: The dendrites receive signals from other neurons; the cell body contains the DNA encoding neuronal proteins and the complex apparatus for synthesizing them; the axon projects over long distances to target cells (for example, other neurons or muscle cells); and the nerve terminals release neurotransmitters at synapses with targets. (b) Ion channels span the entire plasma membrane, regulate the flow of ions across it and determine the changes in membrane potential. Adapted with permission from 59. 10
- Figure 1.8** Equivalent circuit of a plasma membrane of a typical neuron, as from ⁵⁷. The lipid bilayer structure of the plasma membrane separates two conducting solutions of ions: the cytoplasm and the extracellular fluid and acts like a capacitor (C_m). The presence of ion channels provides a conductive path to certain ions. The concentration gradient of an ion determines the value of the battery corresponding to it (V) and the permeability of plasma membrane to certain ion type determines

the conductance (g) values. L represents the factors corresponding to the leaky membrane currents arising from the passive properties of the cell membrane and V_m denotes the resting membrane potential. 12

Figure 1.9 Schematic of a typical Action Potential (spike) and the sequence of events involved. 12

Figure 1.10 The Patch Clamp (a) Schematic of the voltage clamp technique. (b) The patch micropipette and gigaohm seal across a channel. (c) Typical action potentials measured across a neuronal membrane in current clamp mode. (d) Typical single channel current recordings: current drops to baseline when the channel gets closed in response to a stimulus or vice versa. Adapted with permission from ^{57,66} 13

Figure 1.11 Multi-Electrode Array system (a) A standard planer 8X8 MEA with 60 electrodes. (b) Single electrode: size can vary from 10 μ m to more than 200 μ m depending on application. (c) MEA recordings are extracellular; can be used to stimulate and simultaneously record from an entire tissue, thereby providing spatial information. Adapted with permission from ⁶⁸ 14

Figure 1.12 (a) Basic structure of Eye (b) layered arrangement of the retinal neurons. (c) Block diagram of the various connections that exist in between the neuronal layers. The block arrow shows the direction of signal transduction. Adapted with permission from ⁵⁸ 16

Figure 1.13 Morphology of the photoreceptors. (a) Rod and cone cells. (b) Incident light causes cis- to trans-retinal conformation change in the rhodopsin; this is the starting point of signal transduction in the retina. Adapted with permission from ⁵⁷ 17

Figure 1.14 Signal Transduction in the retina. (a) Various signal pathways across the layers (b) cGMP ion channels close in presence of light thereby hyperpolarizing the photoreceptors (c); (d) corresponding spike trains produced on an ON-center ganglion cell. Adapted with permission from ⁵⁷ 17

Figure 1.15 Schematic showing the placement of subretinal and epiretinal implants. With a subretinal implant, the subretinal space is placed with a silicon plate carrying light-sensitive microphotodiodes, each equipped with a stimulation electrode. Light from the image directly modulates the microphotodiodes, and the electrodes inject currents into the remaining neural cells (horizontal cells, bipolar cells, amacrine cells, and ganglion cells) of the retinal inner layer. In contrast, the epiretinal implant has no light-sensitive areas but receives electrical signals from a distant camera and processing unit outside of the body. Electrodes in the epiretinal implant (small

black knobs) then directly stimulate the axons of the inner-layer ganglion cells that form the optic nerve [Adapted with permission from ⁹⁵]. 21

Figure 2.1 Chemical structures of (a) P3HT, (b) N2200 and (c) PCDTBT. (d) Work functions of various materials used in the experiments (e) Solution form of P3HT, N2200 and the BHJ prepared with a 4:1 P3HT:N2200 ratio in 10 mg/ml concentration (f) Absorption spectrum of a BHJ film (g) Schematic of the measurement set-up for photocurrent and photopotential characterization (h) Schematic of the device structure used for three-color sensing. 29

Figure 2.2 Photocurrent across ITO/polymer/PBS compared for 400 nm films of P3HT and BHJ (P3HT:N2200). Signals were measured for a 2.5 mm² area for blue incident light ($\lambda=450$ nm, 250 ms duration) intensity 2 mW/cm². 31

Figure 2.3 Photoresponse from P3HT:N2200 thick films (~ 4.5 μ m) in ITO/BHJ/EI structure with KCl (100 mM) electrolyte, shown for two sides of illumination. Inset: Response of the PCDTBT:N2200 based ITO/BHJ/EI device for similar active layer thickness. 32

Figure 2.4 (a) Photocurrent response of ITO/P3HT:N2200/EI device structures to a white light pulse incident from electrolyte side for different BHJ layer thickness. (a)-Inset. Photocurrent response of ITO/PCDTBT:N2200/EI device structure to a similar light pulse for BHJ layer thickness 3.5 μ m and 0.2 μ m, depicting no reversal in polarity. (b) Ratio of the magnitude of the photovoltage spike (I_{peak}) to the steady state potential (I_{ss}) and I_{ss} , as obtained from (a), as a function of film thickness. ... 33

Figure 2.5 Normalized photoresponse of ITO/P3HT:N2200/aq device in a two-color (red and green) detector configuration. The thickness of the BHJ film is ≈ 2 μ m and the light flash is switched 'on' at $t = 0$ s. The schematics in the inset depict the mechanism of polarity reversal in response to green (high absorbing) and red (low absorbing) λ s. The color gradient depicting BHJ layer between water and ITO represents the vertical phase segregation of donor and acceptor with acceptor concentration gradient towards the ITO. 34

Figure 2.6. Photovoltage vs. photocurrent mode of operation. (A) The photovoltage (V_{ph}) measurement across ITO/BHJ/EI(water) device in open circuit conditions; (B) The photocurrent (I_{ph}) measurement across the same ITO/BHJ/EI(water) device in short circuit conditions, using electrometer (Keithley 6512). The composition of BHJ layer is P3OT:N2200 (4:1 w/w), the thickness of the BHJ layer is ≈ 1.9 μ m and the illumination is from the aqueous-layer side. 35

- Figure 2.7** (a) The response of BHJ/waer device structure to an alternate red (690 nm) and green (525 nm) light pulse illumination under constant white background, measured using electrometer (Keithley 6512). One illumination cycle corresponds to one red and one green light flash, each for duration of 10 s. The composition of BHJ layer is P3OT:N2200 (4:1 w/w) and thickness of BHJ layer is $\approx 1.9 \mu\text{m}$. (b) The ratio of peak value of photocurrent in response to Red light (R_{peak}) to that of Green light (G_{peak}) is plotted as a function of time..... 36
- Figure 2.8** Comparison of water and aqueous KCl solution as the aqueous medium (a) The comparison of device response to illumination with $\lambda=525 \text{ nm}$ from the aqueous medium side. (b) The comparison of device response to illumination with $\lambda=525 \text{ nm}$ from the ITO side. BHJ composition is P3OT:N2200 (4:1) and thickness is $3.2 \mu\text{m}$. (c) Stability of device with de-ionized water and KCl solution. The peak value of $I_{\text{ph}}(t)$ in response to $\lambda=525$ is plotted as the number of cycles of illumination at a frequency of 3 Hz ($\sim 160 \text{ ms ON}, 160 \text{ ms OFF}$). Responsivity is normalized with the peak value of the $I_{\text{ph}}(t)$ at $t=0$. (d) Absorption spectrum of P3OT:N2200(1:1) BHJ structure coated on quartz in contact with water and 100 mM aqueous KCl. . 37
- Figure 2.9** Simulation of two-color detection scheme using circuit parameters. (A) The equivalent circuit of a BHJ/aq structure. (B) The simulated response for $\lambda \sim 525 \text{ nm}$ (green) and for $\lambda \sim 630 \text{ nm}$ (red)..... 38
- Figure 2.10** (a) Photoresponse of a three-color (red, blue, green) detector device fabricated using a blue selective ($\lambda=470\text{nm}$) Bragg reflector behind the ITO-coated glass. The solid lines correspond to the analog fit to the observed I_{ph} (see text). Inset shows the variation of the peak value of $I_{\text{ph}}(t)$ as a function of intensity of incident $\lambda = 532 \text{ nm}$. (b) The response of ITO/BHJ/aq(KCl) device structure to spectral yellow light (575 nm) and to the yellow color obtained from optically mixing the red (690 nm) and green (525 nm) colors. Thickness of the BHJ layer is $\approx 2.1 \mu\text{m}$. The light flash is switched 'on' at $t = 0 \text{ s}$ 39
- Figure 2.11** Proposed digital electronic circuit for demosaicing. (a) The digital logic circuit including comparators (comp) and 4-bit shift registers, where comp 1 is biased to detect positive photovoltage (V_{ph}) whereas comp 2 is used to detect negative V_{ph} . (b) The output response of comp 1 and comp 2 to the V_{ph} from the device to green, red and blue incident colors for certain clock pulse. (c) The

possible output bit pattern of the digital circuit shown for the three colors that can be obtained by using another set of 8-bit shift registers. 41

Figure 2.12 (a) The photoresponse of ITO/BHJ/EI(water) device to white light is compared with that to red and green light. The $I_{ph}(t)$ in this case is measured using an electrometer (Keithley 6512). (b) Unlike in response to the red and green light illumination, the charge carrier generation in case of white light illumination is uniform in the bulk of the BHJ layer and hence the transient spike feature is absent. 42

Figure 2.13 (a) Schematic of the 8X8 multi-electrode array (MEA) with 60 ITO electrodes coated with the BHJ layer of thickness $\approx 2 \mu\text{m}$ (equal to L_c , see text). 100 mM aqueous KCl solution is held on top of the polymer film. (b) Various wavelengths of the visible spectrum dispersed onto the array in the manner shown. (c) The photovoltage response of such ITO/P3OT:N2200/aq device as a function of the various λ s of the visible spectrum (λ error bar $\sim 10 \text{ nm}$). The light flash is switched 'on' at 80 ms. Eight windows correspond to the response from each row of the MEA. 43

Figure 2.14 Differential sensitivity as a function of wavelength. (A) Transition from positive polarity to negative polarity as a function of wavelength for a ITO/BHJ/aq(100 mM KCl) device. The response is recorded using an electrometer (Keithley 6512). (B) Differential sensitivity, defined as $\Delta S = I_{ph}^{max}(\lambda_2) - I_{ph}^{max}(\lambda_1)$, normalized and plotted as a function of λ . The BHJ composition is P3OT:N2200 (4:1) with a thickness of $\sim 2 \mu\text{m}$ 44

Figure 2.15 Photoresponse of bilayer structures. The response of P3HT/N2200 and N2200/P3HT bilayer structures is compared with that of P3HT:N200 (4:1) BHJ structure, in contact with water. Illumination is by $\lambda=525 \text{ nm}$ from the ITO side. Light pulse is ON at $t=125 \text{ ms}$ 45

Figure 2.16 (A) Photocurrent across an ITO/bR/electrolyte(100 mM KCl) device. (B) ERG recording from an isolated retina using MEA set-up. 45

Figure 2.17 Modulated photocurrent spectrum of BHJ/aq photodetector. (A) Modulated photocurrent spectrum of the ITO/BHJ/aq(water) device with BHJ thickness $\sim 2 \mu\text{m}$ in dark background. (B) The photocurrent across the ITO/BHJ/aq(100 mM KCl) device with critical BHJ film thickness ($\sim 2.1 \mu\text{m}$) in antagonistic color backgrounds. 46

- Figure 2.18** Frequency (ω) dependence of a ITO/P3HT/EI device for thin polymer film (~ 200 nm) with 100 mM KCl concentration in dark as well as under white light illumination. The crossover frequency (ω_c) is shown at 125 kHz. Capacitance follows a power law behavior as $C \propto \omega^{-\alpha}$ where $0 < \alpha < 1$ for low frequency and $1 < \alpha < 2$ for high frequency. Similar curves are obtained for thick films ($> 2 \mu\text{m}$) as well. 47
- Figure 2.19** (a) Photocapacitance observed for ITO/P3HT:N2200/EI structure at different ω . Inset- Photocapacitance observed for ITO/PCDTBT:N2200/EI structures. 100 mM KCl is used as electrolytes for both cases. (b) Differential photocapacitance $\Delta C/C_{\text{dark}}$ obtained from (a) plotted as a function of ω for various electrolyte concentrations..... 48
- Figure 2.20** Normalized photocapacitance of a ITO/P3HT/EI structure for PMII as the electrolyte and Pt as the counter electrode. The film thickness is ~ 400 nm. The response times are observed to be slower in comparison to the BHJ/EI structures. 48
- Figure 2.21** (a) The critical frequency (ω_c) shifts to a higher value with increasing thickness of the BHJ layer in ITO/P3HT:N2200/EI device with KCl electrolyte. The KCl concentration is 50 mM; thin film ~ 400 nm and thick film $\sim 4 \mu\text{m}$. (b) ω_c measured for different concentration of KCl solution for ITO/P3HT:N2200/EI device. ω_c shifts to a higher value with increasing electrolyte concentration. Also shown is the variation of differential photocapacitance ($\Delta C/C_{\text{dark}}$) with electrolyte concentration. At a fixed probe frequency (50 kHz), $\Delta C/C_{\text{dark}}$ increases with increasing electrolyte concentration..... 49
- Figure 2.22** C(V) plots obtained at various frequencies ω for P3HT/PMII polymer/EI structure, in non-illuminated conditions. The slope of the plot gets reversed at high ω 50
- Figure 2.23** Effective carrier concentration at the ITO/BHJ interface with light incident from EI side and the photocurrent peak value (I_{peak}) as modeled from the drift-diffusion equation..... 52
- Figure 2.24** Photocurrent response of ITO/BHJ/EI device compared for two types of electrolytes : 3-propyl 1-methyl imidazolium iodide (PMII) and 100 mM KCl. The BHJ layer consists of P3HT:N2200 (1:1) with film thickness $\sim 5.4 \mu\text{m}$. Device is illuminated from electrolyte side with white LED pulsed at 1 Hz (on duration - 500 ms). PMII is a room temperature ionic liquid constituting the regenerative redox

couple Γ/I_3^- . The higher magnitude of the steady state photovoltage and the absence of the transient response in BHJ/PMII devices point to the notion that the charge transport within PMII electrolyte layer is electronic, while that within KCl is ionic..... 54

Figure 2.25 Schematic showing the mechanism of polarity dependent color discrimination using the BHJ/EI devices. 55

Figure 2.26 Comparison of BHJ/aq device response with that of a solid-state device is depicted. The inset shows the response of ITO/BHJ/aq(water) and ITO/BHJ/Aluminum device with $\lambda=525$ nm from the ITO side, where the thickness of the BHJ layer is ~ 450 nm..... 56

Figure 2.27 The behavior of space charge capacitances of a p-type semiconductor as a function of bias^{56,119}. C_{SC} is the space charge capacitance of the semiconductor, C_H is the Helmholtz layer capacitance, C_d is the capacitance of the diffuse layer of charges in the electrolyte and C_T is the total capacitance. E_{fb} is the flat band potential of the semiconductor and E is the applied bias. AL, DL and DDL represent the accumulation, depletion and deep depletion regimes of the space charge capacitance respectively. At low ω , C_T follows the profile of C_{SC} . (b) At much higher ω , C_H dominates the total capacitance¹²⁰ and therefore C_T would follow the profile of C_H 58

Figure 3.1 (a) Schematic showing a degenerate retina from rd1 mouse. (b) Schematic of the experimental set-up. The ITO/BHJ glass were subretinally interfaced with the retina and RGC responses were recorded using the patch clamp apparatus. (c) Increased RGC activity upon photoexcitation of the underlying BHJ layer (d) Inhibited RGC activity upon photoexcitation of the BHJ layer recorded from another cell. The spikes in (c) and (d) represent individual action potentials from the cell, measured by extracellular single unit recordings in loose patch configuration. 64

Figure 3.2 (a) Schematic of the steps involved in retina isolation from an animal (b) Snapshot of a retinal explant on a MEA (c) Snapshot of BHJ coating on a MEA placed in the amplifier (d) Schematic of the experimental set-up used for interfacing BHJ-coated MEA with the retina explant from a chick eye. 68

Figure 3.3 Photovoltage, $V_{ph}(t)$ profiles from a $10 \mu\text{m}$ diameter TiN electrode at $\sim 500 \mu\text{W}/\text{mm}^2$, and $1000 \mu\text{W}/\text{mm}^2$ of incident light with $\lambda=405$ nm. Q_{th} and t represent the assumed threshold charge density required for eliciting neuronal activity and corresponding expected latency of the neuronal response, respectively. 69

Figure 3.4 Background experiments (a) MEA recordings without the retina, for uncoated and BHJ-coated MEA electrodes. Illumination data shown for a 100 ms light pulse of $\lambda=410$ nm at $200 \mu\text{W}/\text{mm}^2$. Upon photostimulation, there is no artifact on the uncoated MEA, while for the BHJ-coated MEA, the BHJ response appears as a transient signal at the instants of light On and Off. (b) Spontaneous wave-like activity recorded on an uncoated $30 \mu\text{m}$ TiN electrode of the MEA. (c) Light-induced neuronal activity from a retina on a BHJ-coated electrode, along with a spontaneous retinal wave. The existence of the spontaneous wave confirms that the retina in contact with the BHJ retains its natural activity. Data shown for light pulse of $\lambda=410$ nm at $500 \mu\text{W}/\text{mm}^2$ (d) S/N comparison of an uncoated and BHJ-coated TiN electrode. The average S/N ratio of the spontaneous retinal activity on the BHJ-coated and uncoated MEAs is 8.6 ± 1.1 and 10.3 ± 0.6 respectively. 70

Figure 3.5 Control experiment. A representative raster plot data showing the results of the control experiment compared with the BHJ/retina experiment. (a) Successive photoexcitation of the retina on uncoated MEA does not elicit any additional neuronal activity. Only spontaneous activity exists in the experiments without the BHJ. (b) Photoexcitation of the retina on BHJ-coated MEA elicits a neuronal activity. The elicited neuronal response is consistent with successive flashes. The spontaneous activity of the retina is independent of the elicited retinal response. Each flash of light represents a 100 ms wide pulse of $\lambda=410$ nm at $500 \mu\text{W}/\text{mm}^2$, time interval between successive flashes is 10 s..... 71

Figure 3.6 A recording snapshot of the BHJ-coated MEA system with the retina. Upon stimulation with a 50 ms wide light pulse, the BHJ response in form of initial transient spikes followed by retinal activity can be seen on many electrodes, for example, electrode #34..... 73

Figure 3.7 Typical neuronal response elicited in the retina upon polymer photoexcitation. The BHJ transient photovoltage signals are followed by the neuronal spikes. A magnified time window shown for $\lambda=410$ nm, at $400 \mu\text{W}/\text{mm}^2$, 200 ms pulse duration. 74

Figure 3.8 Neuronal responses to photoexcitation of the BHJ layer with green, orange and white incident light pulses. Inset shows the wavelength spectra of the incident colors..... 75

Figure 3.9 Elicited neuronal activity upon photoexcitation of the BHJ layer with a blue light pulse ($\lambda=410$ nm), under dark and white dc background (~ 200 lux) at a pulse intensity of (a) $150 \mu\text{W}/\text{mm}^2$ (b) $500 \mu\text{W}/\text{mm}^2$	76
Figure 3.10 (a) A raster plot of elicited action potentials with increasing light intensities. Each marker corresponding to a specific intensity represents an action potential. (b) PSTH of the elicited activity for 2 intensities, showing increased number of spikes and rate of occurrence at higher intensity. (c) The average response latency as a function of light pulse intensity; solid line represents the power-law fit. (d) The average number of evoked spikes as a function of light pulse intensity. All data was recorded with $\lambda=410$ nm illumination, pulse duration 200 ms.	77
Figure 3.11. Dependence of evoked activity on duration of light pulse. (a) Average number of spikes per second (b) Average latency of the neuronal activity. Data shown for blue light pulse at $500 \mu\text{W}/\text{mm}^2$	78
Figure 3.12 The number of action potentials as a function of time interval between successive light flashes. Light flashes of 200 ms duration, $\lambda=410$ nm, whole field illumination. Y-axis is normalized by the number of action potentials on the first flash for a specific intensity.	79
Figure 3.13 Spatial stimulation plot (2D map) of the retinal activity at a MEA electrode (# 43, marked with an open triangle). The map shows the average number of spikes/sec elicited. Inset- Response latency of the activity at the same electrode upon local photoexcitation of the BHJ layer on other MEA electrodes.	80
Figure 3.14 (a) Retinal ganglion cells' dual-peak response to optical stimulation from a chick retina seen in a PSTH plot. Light stimulus was given at 0 ms. Used with permission from ¹³² . (b) Responses of chick retina's ganglion cells evoked by single voltage pulses of pulse duration 0.5 ms - analog trace and PSTH. Spike response pattern consisting of initial response followed by a transient inhibition and a delayed response. Used with permission from ⁹¹	81
Figure 4.1 Schematic showing various factors determining the cell-material interactions. Adapted with permission from ¹⁴⁹	86
Figure 4.2 Experimental set-up used for stimulation of neurons with BHJ polymer layers during cell culture.....	90
Figure 4.3. Bright field images of retinal cells after 5 DIV and after 10 DIV on Glass and BHJ layer. Some neuronal cells are marked with red arrows.	92

Figure 4.4 Cell viability assay. Representative fluorescence images after TUNEL staining on retinal dissociated cell cultured on (a) Glass, (b) Glass/P3HT:N2200 (4:1) after 10 DIV. Scale bar = 50 μm . The mean percentage of apoptotic cells on the two substrates is $(17.2 \pm 5.6)\%$ and $(18.8 \pm 4.2)\%$ respectively. 93

Figure 4.5 Imaging neurons after nuclear and neuronal staining. Image shown for a culture on glass coverslip after 4 DIV. Scale bar = 20 μm 94

Figure 4.6 Retinal dissociated cells on a BHJ layer on two different substrates after 4 DIV. Scale bar = 20 μm 95

Figure 4.7 Representative images from a retinal cell culture after 4 DIV. Scale bar = 50 μm 96

Figure 4.8 (a) Schematic of the experiment for stimulation of retinal cells with BHJ layers (b) An increase in the average fraction of neurons on photoilluminated BHJ coated substrates. 97

Figure 5.1 Schematic showing (a) Optoelectronic features across the BHJ/electrolyte interface having characteristic transient pulse profiles. (b) The photoexcitation of the BHJ/electrolyte interface resulting in stimulation of a blind retina with dysfunctional photoreceptors. 101

Chapter 1

Introduction

The integration of biological systems at cellular and systems level with soft materials having electronic and sensory capabilities opens up interesting possibilities. Synthetic polymers have been extensively used for biomedical applications including biosensing, bio-diagnostics and therapy. For instance, the availability of soft polymer substrates, which mechanically mimic the in vivo conditions, has helped in rapid advances in the field of tissue engineering. Further introduction of electronic properties in these polymeric substrates makes it possible to couple them to electrically active tissues such as brain, heart and skeletal muscles to create various body-machine interfaces and implants. The unique combination of mechanical, electronic and optoelectronic properties of these polymeric systems opens up new vistas and possibilities and enables the development of novel bioelectronic interfaces (**Figure 1.1**).

The possibility of using conjugated polymers in aqueous environments for sensing, probing and controlling ionic transport around biological system points to the utility of these materials for novel bioelectronic hybrid devices. In biological systems, the intra- and inter-cellular transport are mediated by specific signalling mechanisms, which are regulated by ions and ion transport; e.g. in the case of neuronal signalling. Also, various molecules and protein complexes play a major role in the binding of the cells with an external surface. This thesis presents device architectures based on conjugated polymeric materials, which could be used for biomimicking certain processes in the visual system, evoking neuronal activity in a blind retina model, and manipulating neuronal networks in primary cell cultures. These problems constitute an interdisciplinary area of research, and involve an understanding of certain materials properties, biological phenomena and their interface characteristics. In the following sections, some of these relevant aspects are briefly discussed.

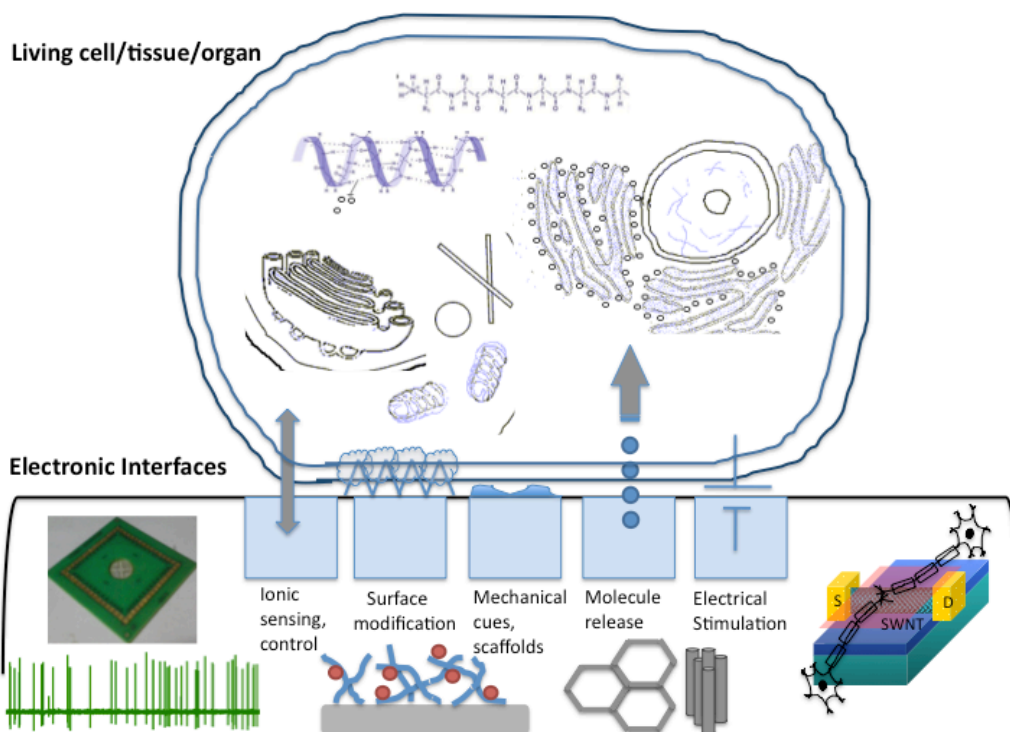


Figure 1.1 Schematic showing various possible bioelectronic interfaces based on conjugated materials.

1.1 Conducting and semiconducting polymers

Conjugated polymers can be divided into two classes – conducting and semiconducting – and have a unique set of properties, combining the electronic properties of metals and semiconductors with the processing advantages and mechanical properties of polymers¹⁻³. Chemical structures of some common conjugated polymers are shown in **Figure 1.2**. Conjugated polymers are unsaturated macromolecules having π -electron density delocalized along their backbone chain, which determine their electronic and optical properties. Chemical tailoring of the aromaticity or the backbone structure in these molecules gives a control of many of these properties. These polymers can be thought of as electronic inks, and devices based on such organic materials can be manufactured with features at μm - nm length scales using techniques, which are common to plastic processing, such as dip-coating, spin coating, and different forms of printing methods. The added advantage is that these methods can be used for depositing these materials on flexible and conformal substrates⁴.

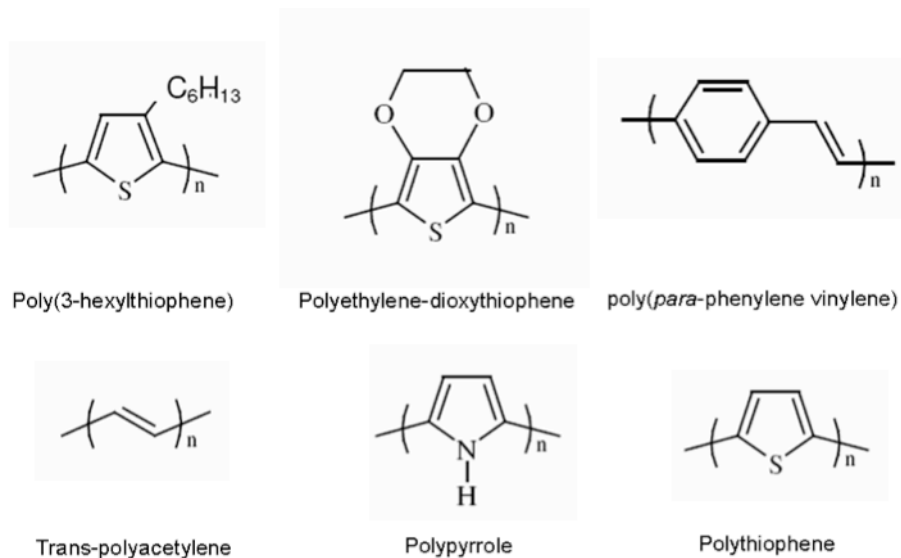


Figure 1.2 Chemical structures of some important conjugated polymers.

Conducting polymers have been demonstrated to have high electrical conductivities (>1500 S/cm)^{5,6}. This class of π -conjugated materials have both electronic and ionic conductivity, which arises from doping. The doping mechanism in conjugated polymers involves partial removal or addition of electrons/ions from the polymer π -backbone, which can be achieved through chemical or electrochemical means⁷. Examples of conducting polymers include polypyrroles, PEDOT:PSS and polyanilines. These conducting polymer forms have been extensively used for various purposes like actuators⁸, electrochemical transistors⁹⁻¹², electrode-cell communications¹³⁻¹⁵ and electrochromics¹⁶⁻¹⁸.

The semiconducting forms of conjugated polymers exhibit optoelectronic properties, and are utilized in a wide variety of electrical and optical devices such as organic photovoltaic cells (OPVs)¹⁹⁻²¹, organic light emitting diodes (OLEDs)²²⁻²⁴ and organic field-effect transistors (OFETs)^{25,26}. The band gap of most semiconducting polymers lies in the range 1-3 eV and hence they can be excited by visible-NIR photons. These polymers possess an unprecedented flexibility in the synthesis procedure, allowing for alteration of a wide range of properties, such as bandgap, molecular orbital energy

levels, wetting and structural properties, as well as doping. These materials are a less expensive alternative to inorganic semiconductors owing to simple processing techniques. Further, the high absorption coefficients of these materials allows for thin, transparent and light-weight structures, unlike the devices based on inorganic materials like Silicon.

These organic polymeric materials have many features that can be utilized for accessing physiological systems and developing biointerfaces. These materials mediate the large difference in mechanical modulus between the electrical circuit and the biological system and are also shown to be biocompatible. They can be modified with bio-molecular side-groups to promote cell viability. The conductivity towards ions and electrons renders these materials to be more selective and sensitive than metal-based or silicon-based materials. The semitransparent films of these conjugated polymers make them compatible with various optical microscopy techniques used to image biological components. Organic conducting materials are soft and can be self-assembled and organized to mimic biological structures. This property has been used to obtain 3-D scaffolds for directed cell growth. Various indicator/enzyme/neurotransmitter molecules can be incorporated on the surface or inside the bulk of these materials. Further, these materials are stable at physiological temperature and pH.

Although there have been many reports of utilizing the electronic properties of conducting polymers for bio-interfacing, the utilization of optoelectronic properties of semiconducting polymers is very recent. Certain semiconducting polymer systems have recently been utilized as active triggers for neuronal stimulation²⁷⁻³¹. The visual system of the retina, which has a combination of both light sensitive photoreceptors and signal transducing neurons, is a suitable platform for interfacing these optoelectronic materials and utilizing them for repairing or augmenting the physiological mechanism. In the work described in further chapters of the thesis, an active semiconducting layer was interfaced with a retina explant. The unique set of attributes of this layer could be used for evoking neuronal signals in a blind retina and has implications towards artificial retina applications. The semiconducting polymer layer constituted an interpenetrating mixture of donor and acceptor-type polymers (bulk heterojunction), which is discussed in the following section.

1.2 Photoinduced charge generation and the bulk heterojunction concept

The absorption of a photon in a semiconducting polymer results in the formation of a bound electron-hole pair (exciton). The photoinduced charge carrier generation in semiconducting polymers takes place through exciton creation, exciton diffusion, exciton dissociation into positive and negative charge carriers and finally transport of majority charge carriers under the influence of external electric field. The exciton binding energies, lifetimes and diffusion lengths in organic devices are typically in the range, 0.4-1 eV, 1-10 ns and 1-10 nm, respectively ³². Since the binding energy exceeds the thermal energy at room temperature by an order of magnitude, excitons are stable, and electron/hole acceptor molecules need to be added to an organic semiconductor donor to facilitate the generation of free charge carriers. For an electron acceptor added to the donor component of the BHJ layer, the difference in the lowest unoccupied molecular orbital energies (LUMO) or electron affinities of the donor and acceptor material creates the driving force for the rapid transfer of an electron from the donor to the acceptor. The relatively short exciton lifetimes in organic semiconductors require very fast charge separation. Further, owing to the low diffusion lengths, an intermixing of the donor and the acceptor moieties on the nanometer scale is required, which is satisfied in a BHJ system.

In the BHJ active layer film, the donor and acceptor material form an interpenetrating blend ^{3,33-35}. This results in a large interfacial area between the donor and the acceptor material in the phase-separated donor-acceptor network composite. In this structure, the length scale of the blend is similar to the exciton diffusion length and the exciton decay processes is dramatically reduced since in the proximity of every generated exciton there is an interface with an acceptor where fast dissociation takes place. Hence, charge generation takes place everywhere in the active layer. With appropriate transport pathways in each material from the interface to the respective electrodes, the photon to electron conversion efficiency in BHJ-based devices is higher compared to pristine or bilayer structures.

The luminescence quenching and ultrafast photoinduced electron transfer from a donor polymer to buckminsterfullerene(C₆₀) or its derivatives (like PC₆₀BM) as acceptor has

been extensively studied in BHJ PV cells ^{19,20,36}. Other acceptor materials like perylene based molecules and naphthalene based polymers are now being explored as alternatives to PCBM. These acceptor materials have optical absorption in the visible spectrum and contribute to a wider absorption spectrum of the BHJ active layer. Many of these materials have high electron mobilities, better photochemical stability than PCBM, and form appropriate donor-acceptor morphologies. The fundamental physical processes in a BHJ device are schematically represented in **Figure 1.3**. The absorbed photons excite the donor, leading to the creation of excitons in the conjugated polymer. The excitons then diffuse within the donor phase and if they encounter the interface with the acceptor then a fast dissociation takes place leading to charge separation. The resulting metastable electron-hole pairs across the D/A interface may still be coulombically bound and an electric field is needed to separate them into free charges. Subsequently, the separated free electrons(holes) are transported with the aid of the internal electric field, caused by the electrodes with different work functions, towards the cathode (anode) where they are collected by the electrodes and driven into the external circuit ³⁷. These processes can be depicted with an energy level diagram of the BHJ constituents (**Figure 1.4**). The morphology and composition of the BHJ layer, the choice of electrodes and recombination losses are some of the parameters that determine the incident photon to charge carrier efficiencies (IPCE), the photocurrents and photovoltages developed across BHJ-based photovoltaic device structures. Among the several limiting factors in the energy conversion process in the BHJ based photovoltaic devices, the BHJ/cathode interface plays an important role ^{21,38}. The replacement of the cathode by an electrolytic layer in the BHJ-based devices can provide valuable insight into the dynamics of the transport processes. These features are discussed in the next section.

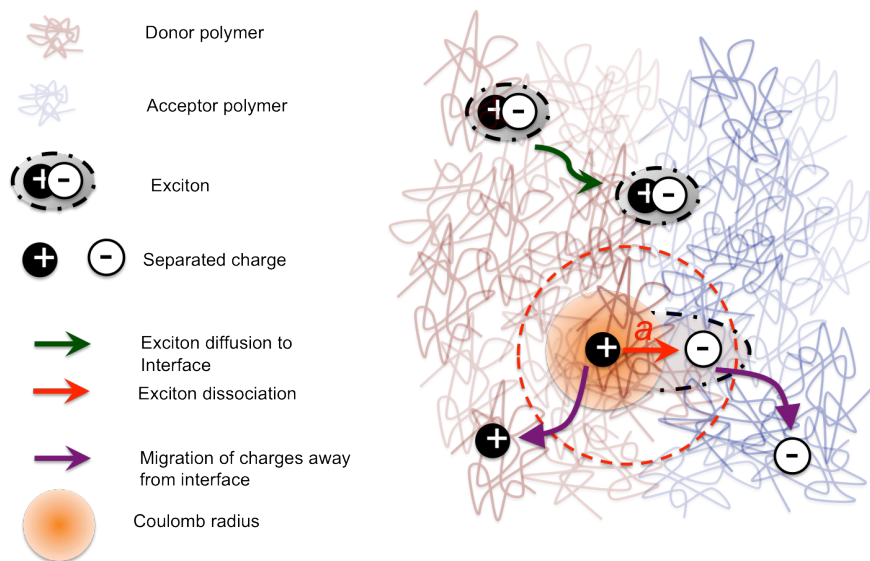


Figure 1.3 Schematic of a donor/acceptor interface showing the processes in a BHJ device.

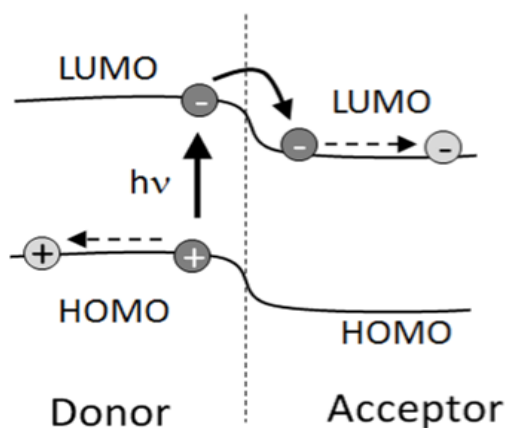


Figure 1.4 Depiction of a donor/acceptor interface through energy levels, the photoexcitation of donor and charge diffusion towards electrodes.

1.3 Semiconducting polymer/electrolyte interface

The use of organic semiconductors and BHJ layers in devices such as photoelectrochemical cells³⁹⁻⁴¹, electrolyte-gated field effect transistors⁴²⁻⁴⁴ hybrid tandem photovoltaic cells⁴⁵⁻⁴⁷ and neuromorphic devices⁴⁸ involve bringing the polymer

surfaces in contact with an electrolyte. Such hybrid semiconductor/EI systems have potential applications for interfacing with biological systems for augmenting or repairing the physiological processes. For this application, a detailed understanding of the various interfacial layers along with the nature and stability of the conjugated polymers in contact with electrolytes is critical.

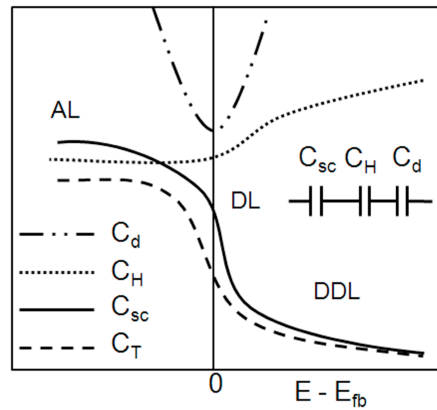


Figure 1.5. Schematic showing the behavior of space charge capacitances of an n-type semiconductor as a function of bias. C_{sc} is the space charge capacity of the semiconductor, C_H is the Helmholtz layer capacitance, C_d is the capacitance of the diffuse layer of charges in the electrolyte and C_T is the total capacitance. E_{fb} is the flat band potential of the semiconductor and E is the applied bias. AL, DL and DDL represent the accumulation, depletion and deep depletion regimes of the space charge capacitance respectively. Redrawn with permission from ⁵⁶.

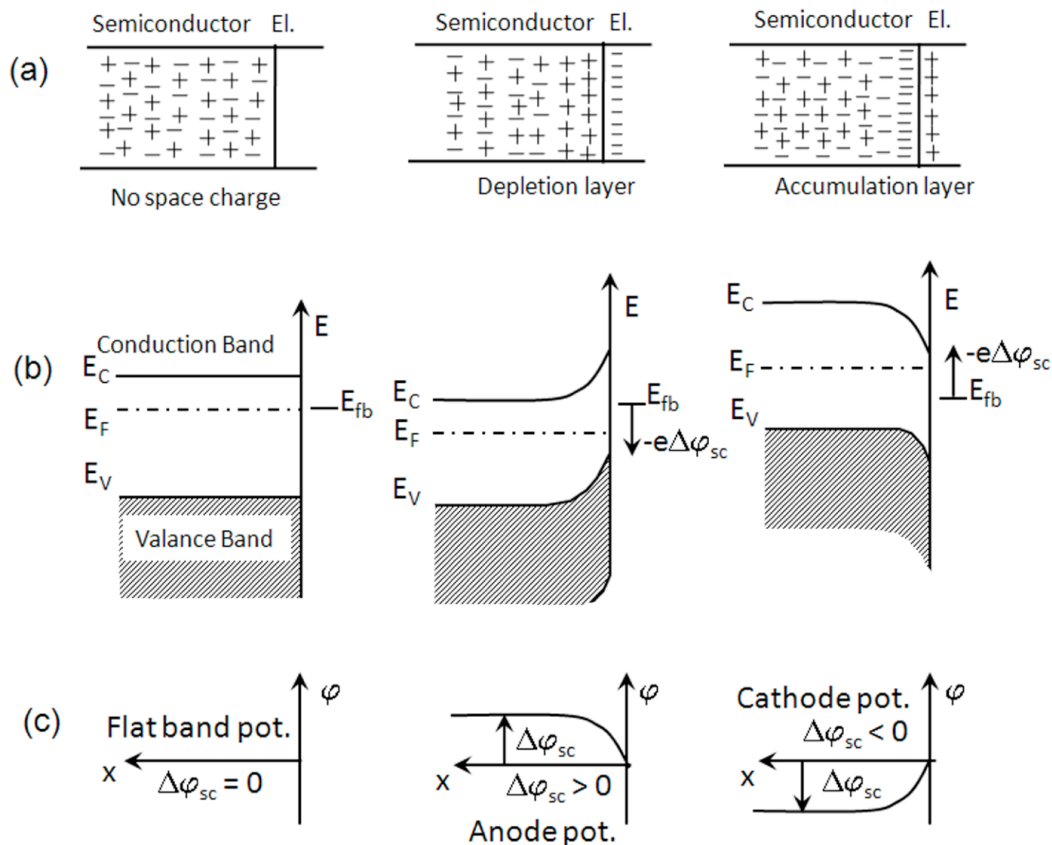


Figure 1.6. Schematic showing the space charge layers in an n-type semiconductor in contact with an electrolyte. (a) Distribution of charge carriers; (b) Course of band edges (c) Course of electric potential. Redrawn with permission from ⁵⁶.

The interfacing of semiconducting polymer layers with biological systems require non-faradaic optoelectronic processes, where negligible charge transfer and redox reactions occur across the semiconductor/EI interface. The device operation in photovoltaic mode with no applied bias, use of moderate light intensities for photoexcitation, and use of aqueous electrolytes and physiological buffers as the electrolyte layer are the suitable characterization parameters. These device conditions closely resemble the physiological environment offered by biological systems.

The visual sensory system is a suitable platform for interfacing optoelectronic BHJ layers. The retina has a combination of light sensing photoreceptors and signal

transducing neurons. The research problems carried out in this thesis involve characterizing the optoelectronic properties of BHJ interface in physiological environments and utilizing the BHJ layers as artificial photoreceptors for stimulating a blind retina explant. The following section briefly describes some of the relevant features related to the visual system and signal recording techniques, and covers only the minimum essential topics required for the understanding of results. A detailed description of these topics can be found in various textbooks and review articles available in literature⁵⁷⁻⁶⁰.

1.4 Introduction to the processes in neural and visual systems

Brain and other components of the nervous system communicate via electrical and chemical wiring networks, with nerve cells or neurons acting like the signal transmitting electric wires. The nerve cells or neurons are the basic unit of the central nervous system (**Figure 1.7a**). The response of a neuron to an external stimulus is a rapid change in its membrane potential, i.e. potential difference across the cell membrane. The rapid changes in the membrane potential are mediated by various types of ion channels (**Figure 1.7b**), which are a class of proteins that span the plasma membrane of all electrically excitable cells like neurons and muscles.

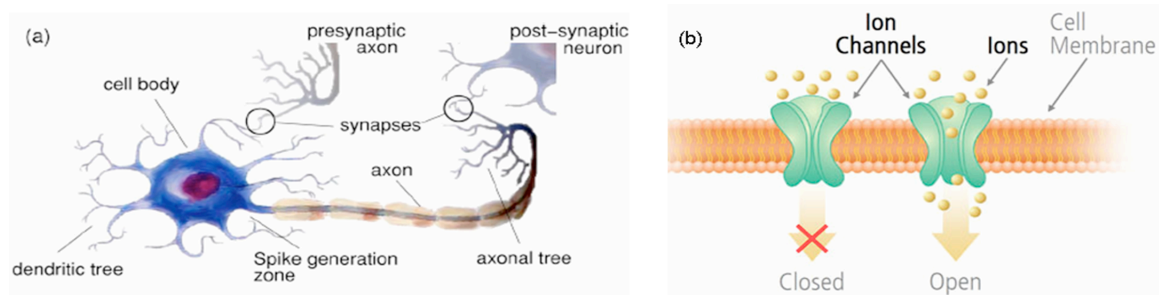


Figure 1.7 A typical Nerve Cell. (a) Basic Structure: The dendrites receive signals from other neurons; the cell body contains the DNA encoding neuronal proteins and the complex apparatus for synthesizing them; the axon projects over long distances to target cells (for example, other neurons or muscle cells); and the nerve terminals release neurotransmitters at synapses with targets. (b) Ion channels span the entire plasma membrane, regulate the flow of ions across it and determine the changes in membrane potential. Adapted with permission from⁵⁹.

1.4.1 Origin of action potentials

The plasma membrane of neurons is generally modeled with an equivalent circuit constituting voltage sources, conductors, a capacitor, and a current generator (**Figure 1.8**). The value of the resting membrane potential (V_m) in nerve cells is determined primarily by resting channels selective for various ions like K^+ , Ca^{2+} , Cl^- , and Na^+ , and is usually given by the Goldman's equation:

$$V_m = \frac{(E_{Na}Xg_{Na}) + (E_KXg_K) + (E_{Cl}Xg_{Cl})}{(g_{Na} + g_K + g_{Cl})}$$

where g represents the conductance of the ion calculated from its permeability, and the values of the E 's are estimated from the Nernst Potential of the corresponding ion, for example,

$$E_{Na} = \frac{RT}{F} \ln \frac{[Na^+]_o}{[Na^+]_i}$$

The Goldman equation estimates the resting membrane potential by taking into account the differential distribution and relative permeabilities of ions across the membrane. As shown in Figure 1.8, the electrogenic Na-K pump balances the passive flux of ions by maintaining their concentration gradients, and hence also contributes to the value of membrane potential estimated by the Goldman equation. At rest, the potential across a typical neural membrane ranges between -60 mV to -80 mV. Upon external stimulus, the changes in membrane potential (action potentials, synaptic potentials, and receptor potentials) during signaling are caused by substantial changes in the membrane's relative permeabilities to these three ions in turn leading to changes in the net charge separation across the membrane. The response of a nerve cell to external stimulus is in form of an action potential. An action potential (or a spike) arises from sequential changes in the membrane's selective permeability to Na^+ and K^+ ions **Figure 1.9**. Action potentials arise if the depolarizing stimulus crosses certain threshold, which is usually ~ 10 mV. The typical spike width in the nervous system are about 1–5 ms. The two electrophysiological techniques used for monitoring action potentials from electrically excitable cells like neurons are – patch clamp and microelectrode arrays.

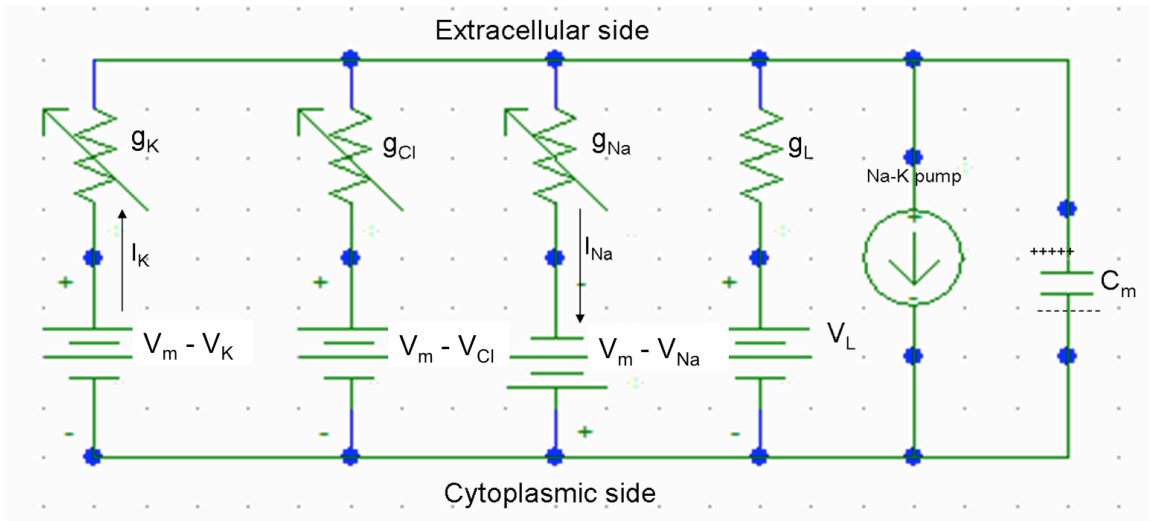


Figure 1.8 Equivalent circuit of a plasma membrane of a typical neuron, as from ⁵⁷. The lipid bilayer structure of the plasma membrane separates two conducting solutions of ions: the cytoplasm and the extracellular fluid and acts like a capacitor (C_m). The presence of ion channels provides a conductive path to certain ions. The concentration gradient of an ion determines the value of the battery corresponding to it (V) and the permeability of plasma membrane to certain ion type determines the conductance (g) values. L represents the factors corresponding to the leaky membrane currents arising from the passive properties of the cell membrane and V_m denotes the resting membrane potential.

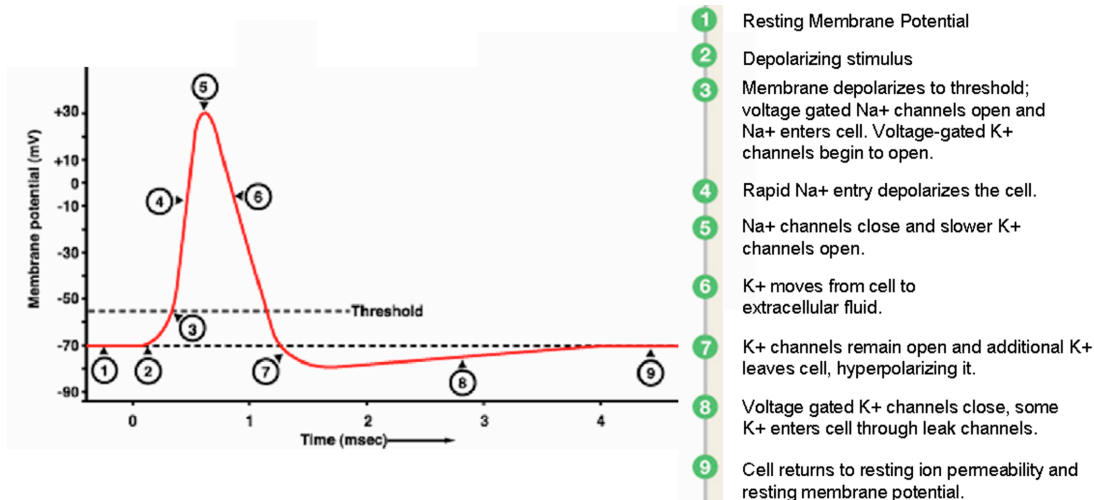


Figure 1.9 Schematic of a typical Action Potential (spike) and the sequence of events involved.

1.4.2 Recording of electrical signals from nerve cells

The studies on giant squid axon by Hodgkin and Huxley ⁶¹⁻⁶⁴ provide a fundamental insight into nerve cell excitability, ion channel kinetics and propagating action potentials.

A revolution in understanding the mechanism of ion flow across the cell membranes in excitable cells like neurons was the development of patch clamp technique by Neher and Sakmann in 1976⁶⁵. The patch-clamp technique has now made it possible to record the current flow through single open channels. *The Patch Clamp Technique* uses a single glass micropipette (tip diameter close to one micron) as an electrode, which is sealed onto the signalling cell (**Figure 1.10**). The interior of the pipette is filled with a solution matching the ionic composition of the bath solution, as in the case of cell-attached mode, or the cytoplasm for whole-cell recording mode. A chloridized silver wire is placed in contact with this solution and conducts electrical current to the amplifier. The patch clamp can be operated in voltage clamp (current recording) or current clamp (voltage recording) mode and can record both single ion channel currents as well as action potentials.

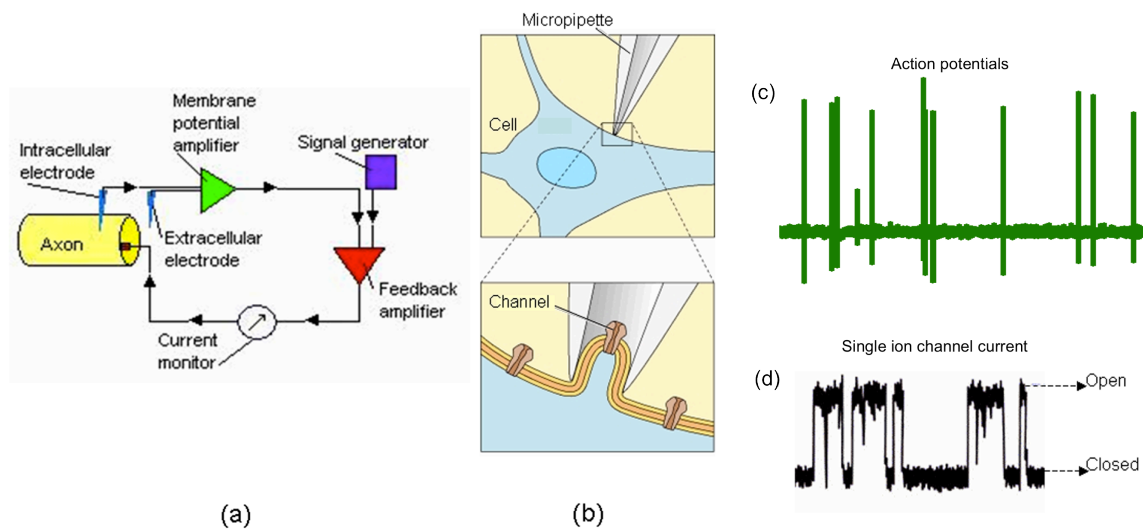


Figure 1.10 The Patch Clamp (a) Schematic of the voltage clamp technique. (b) The patch micropipette and gigohm seal across a channel. (c) Typical action potentials measured across a neuronal membrane in current clamp mode. (d) Typical single channel current recordings: current drops to baseline when the channel gets closed in response to a stimulus or vice versa. Adapted with permission from^{57,66}.

A comparatively recent method of recording cellular activity using *Micro-Electrode Arrays* (MEAs) was developed by Thomas *et. al*⁶⁷ with an aim of drug screening and discovery in cardiac and neural research. The technique involves a set of 60 or more planar metal electrodes on a glass chip, each electrode connected to a voltage and filter amplifier

(Figure 1.11). This is a field recording where the local changes in ion currents in the extracellular fluid are monitored around the signalling cell or a group of cells. MEAs can also be used to stimulate electrically excitable cells using stimuli like current or voltage pulses through these electrodes. MEAs score over the patch clamp technique in cases where both temporal as well as spatial resolution is required. The MEA technique provides the ability to record from several sites in parallel, and changes in the electrical activity can be monitored for long periods of time⁶⁸. The utility of MEA technique has been demonstrated for many interesting problems in biology⁶⁹. In the work carried out as part of this thesis, MEAs were coated with the semiconducting BHJ layers and interfaced with a retinal tissue. This assembly served as a platform for stimulation of tissue with the BHJ layers and signal recording from the retina simultaneously. The following section includes a brief description of the structure and photoinduced processes within the retina.

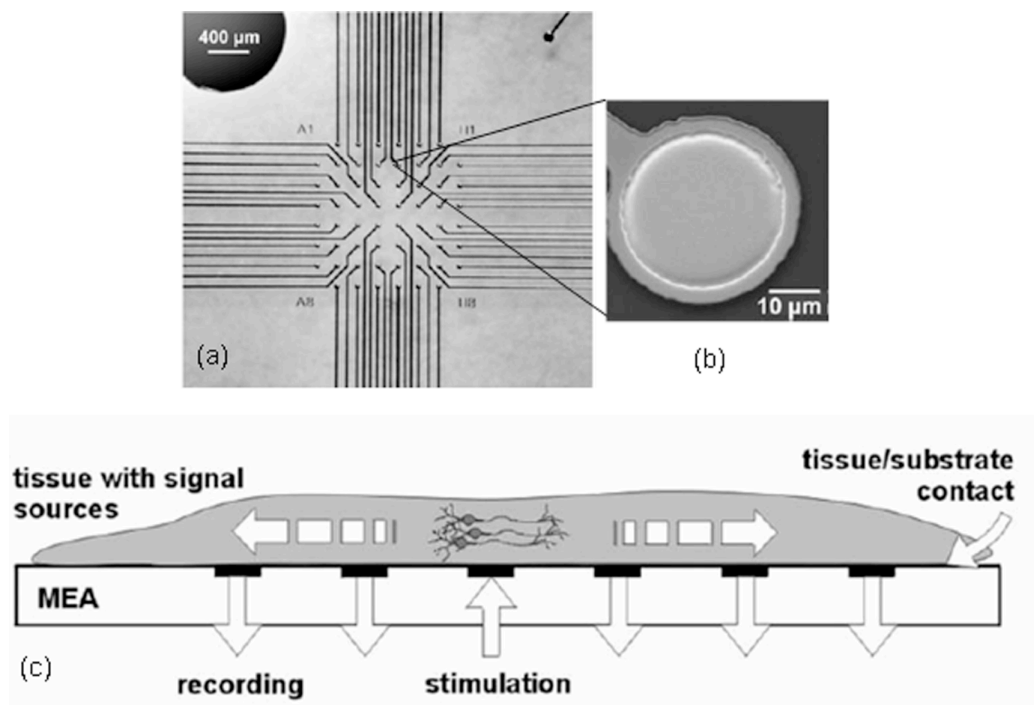


Figure 1.11 Multi-Electrode Array system (a) A standard planer 8X8 MEA with 60 electrodes. (b) Single electrode: size can vary from 10 μ m to more than 200 μ m depending on application. (c) MEA recordings are extracellular; can be used to stimulate and simultaneously record from an entire tissue, thereby providing spatial information. Adapted with permission from⁶⁸.

1.4.3 Introduction to the retina

The retina is the photosensitive sensory organ in the eye. It is a transparent layer of cells, consisting of a light sensitive photoreceptor layer and a complex network of neurons. It encodes the spatiotemporal light signals into neural signals (action potentials) and then transmits these signals through the optic nerve to the higher processing units of the brain for perception (**Figure 1.12**). The photoreceptors – rods and cones – are the input elements of the retina and form the outermost layer. The outer segments of these cells have membranous disks containing the light absorbing photopigments (**Figure 1.13**). The output electrical response of photoreceptors to a light stimulus is a graded change in membrane potential (instead of a spike). The integration times of cones are around 20 ms while for rods its around 100 ms. The next layers of cells are the bipolar, horizontal and amacrine cells that mediate the signals between the photoreceptors and the ganglion cells through various synapses and interconnections. The ganglion cells are the output elements of the retina and form the innermost cellular layer. The ganglion cells transmit the spatiotemporal information of the visual image in form of action potentials through their axons forming the optic nerve and extending to the brain.

Stimulation by light results in a complex signaling by neurons within the various layers of the retina. A three-stage cascade of biochemical events within the photoreceptor cells of the retina results in phototransduction. The key molecule in this process is the nucleotide cyclic guanosine 3-5 monophosphate (cGMP), which controls ionic fluxes across the plasma membrane of photoreceptors. In dark, the concentration of this molecule is in excess, the cGMP gated ion channels are in open state and there exists a constant inward Na^+ current. Hence, in dark, cells are in the depolarized state⁵⁷. Upon photoillumination, the visual pigment rhodopsin in the outer segment disks of rods and cones absorbs light and the chromophore retinal within this pigment changes from 11-cis to all-trans conformation. This activation of rhodopsin in presence of light causes the activation of enzyme phosphodiesterase, which hydrolyses the cGMP molecules and in turn causes the cytoplasmic concentration of cGMP to reduce. The light evoked decrease in cGMP causes the cGMP gated ion channels to close and results in hyperpolarisation of the photoreceptor membranes (**Figure 1.14**). The changes in membrane potential of the photoreceptors are transduced as electrical signals through

their synapses to the interneurons and then to the ganglions. These signals are encoded into action potentials (spikes) in the ganglion cells and then transferred to brain for higher visual processing.

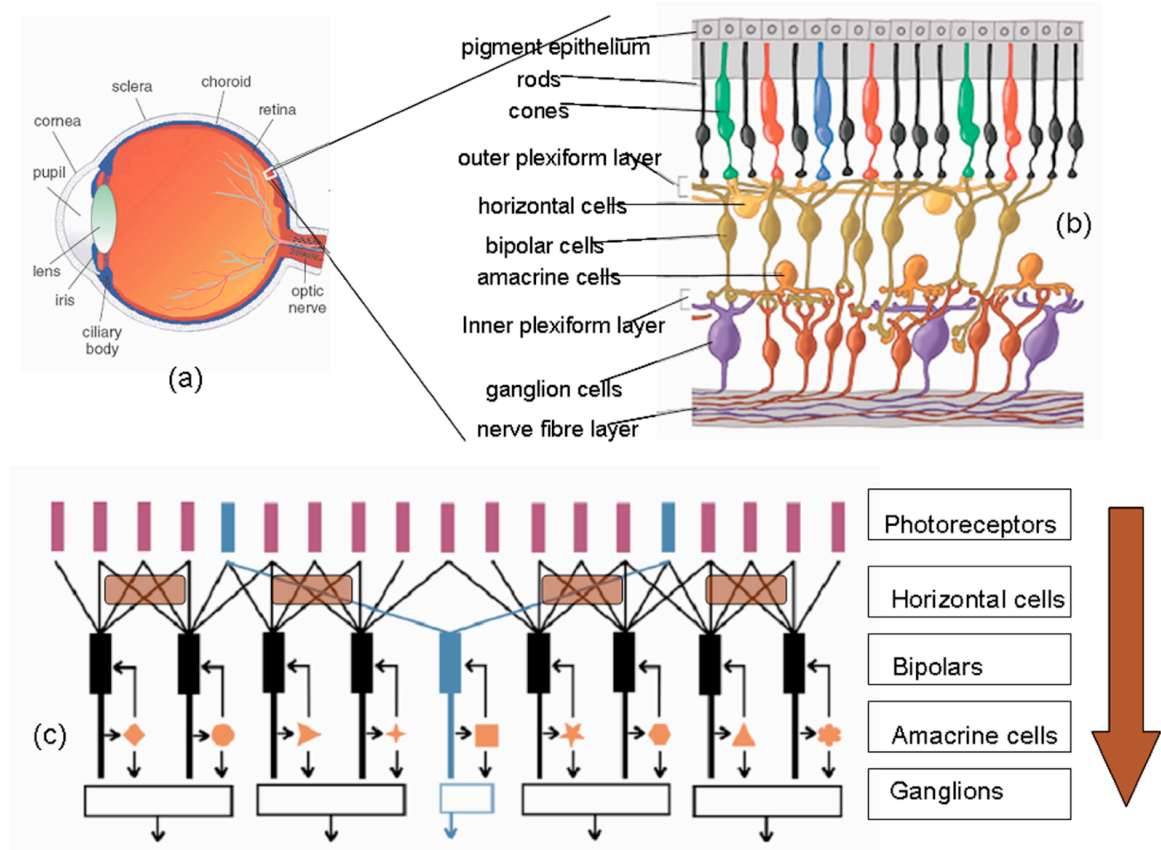


Figure 1.12 (a) Basic structure of Eye (b) layered arrangement of the retinal neurons. (c) Block diagram of the various connections that exist in between the neuronal layers. The block arrow shows the direction of signal transduction. Adapted with permission from ⁵⁸.

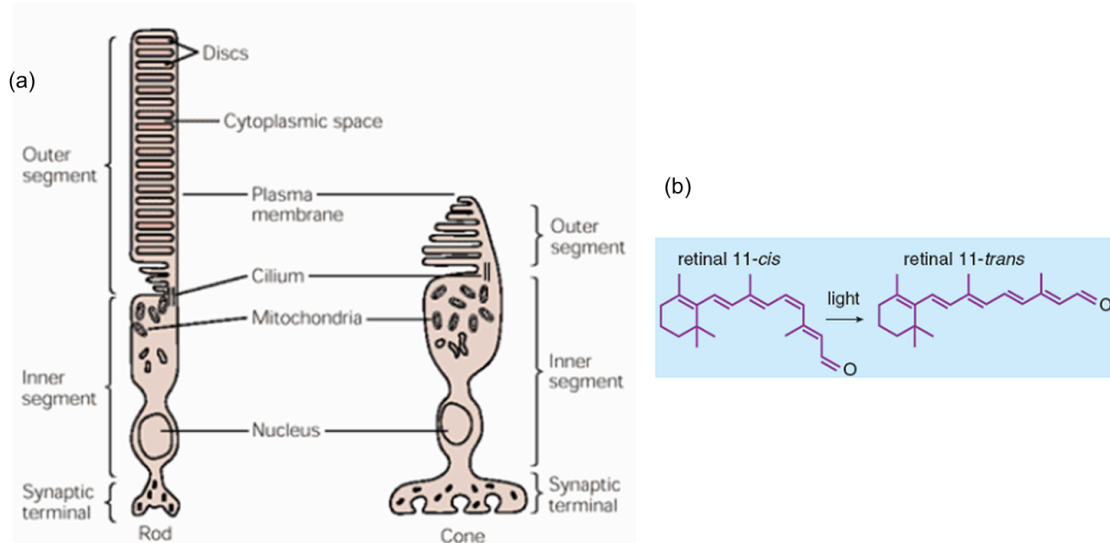


Figure 1.13 Morphology of the photoreceptors. (a) Rod and cone cells. (b) Incident light causes cis- to trans-retinal conformation change in the rhodopsin; this is the starting point of signal transduction in the retina. Adapted with permission from ⁵⁷.

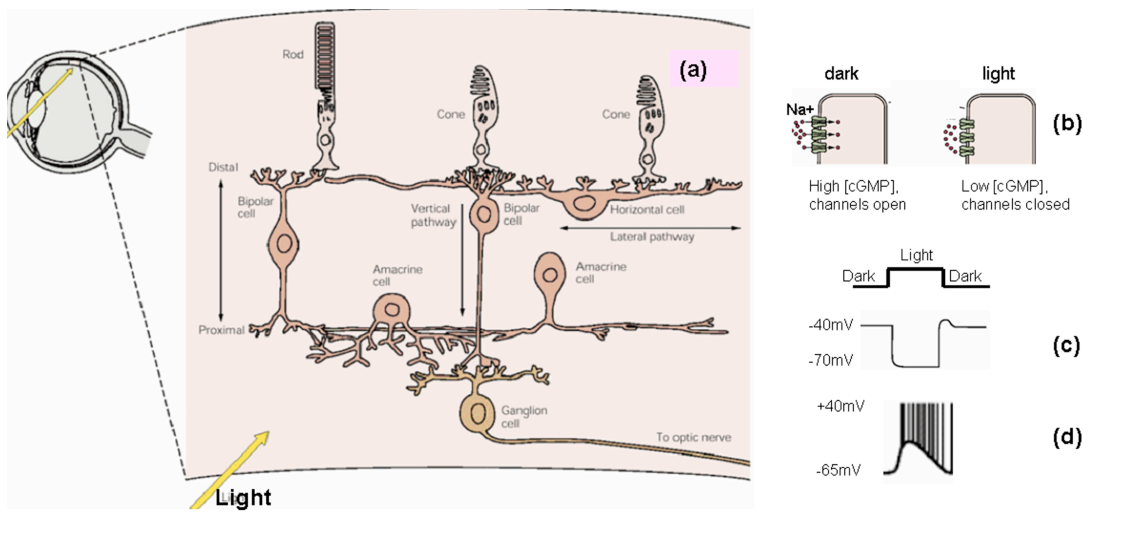


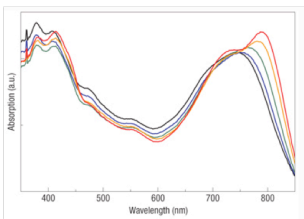
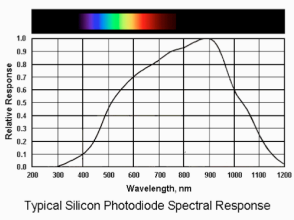
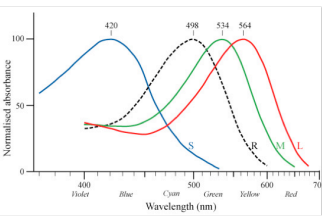
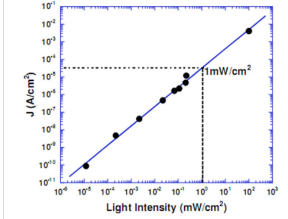
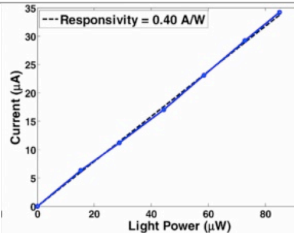
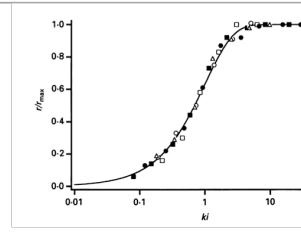
Figure 1.14 Signal Transduction in the retina. (a) Various signal pathways across the layers (b) cGMP ion channels close in presence of light thereby hyperpolarizing the photoreceptors (c); (d) corresponding spike trains produced on an ON-center ganglion cell. Adapted with permission from ⁵⁷.

A comparison between the optoelectronic photodetectors based on organic and inorganic semiconductors with the retina is summarized in **Table 1.1**. Though the photodetection of light by retinal photoreceptors is the first step to vision, the subsequent information processing in the retinal layers results in decoding the image into its specific features. For instance, different types of RGCs with specific receptive fields gather information from the photoreceptors to respond to features such as motion or contrast within the visual signals. Further, the ability of the visual system to decipher and perceive multiple colors is remarkable. The color perception is based on two theories. The trichromatic theory of vision relies on the existence of three types of cones (M, S, L) in the retina, each having peak sensitivity to green (M-type, peak sensitivity at 530 nm), blue (S-type, peak sensitivity at 430 nm) and red (L-type, peak sensitivity at 560 nm)⁶⁰. This theory is restricted to the first level of visual processing and detection of colors at the photoreceptor level. The second, opponent-process theory of color vision considers that the signals arising from the S, M and L cones undergo complex processing at the ganglion cell level, there being receptive fields and selective synaptic connections from photoreceptors to ganglions and ganglions to the visual processing centers of the brain. This theory explains most of the phenomena related to the perception of colors, with its main postulate that the visual system interprets color in an antagonistic way: red vs. green, blue vs. yellow and black vs. white^{60,75}.

Along with the optics and the curvature of the eye, the color sensing ability of the retina has been implemented in the design of many optical imaging devices and modern-age cameras. The color sensing procedure in conventional CCD or CMOS elements is based on two primary approaches. The first approach, similar to the trichromatic model of color vision, involves combining three separate elements or sub-pixels with photosensitivity tuned to three primary colors. The second approach involves color-filter arrays (CFAs) as a mask on the monochrome sensor. The CFAs absorb a sizeable percentage of the incoming light, and the color at each position is reconstructed through interpolation algorithms (demosaicing). There have been efforts towards alternate strategies for color sensing which resemble that of the visual system, and one of such design based on BHJ/electrolyte interface is presented in the next chapter of this thesis. The semiconducting polymers that constitute the BHJ layer have light absorption similar to the photoreceptors. The photopotentials and photocurrents across the BHJ/EI devices

upon photoexcitation are similar to those arising from various photoreceptors. Further, the structures presented have a polarity-based color sensing capability, which distinguishes colors in an antagonistic way, and fits in with the opponent color model of color vision. These device structures have implications towards the development of novel photodetectors that can be utilized in cases where retinal photoreceptors need to be repaired or augmented, for instance, retinal degeneration. The following section describes the presently used strategies for retinal prosthesis.

Table 1.1 Summary of the photodetection properties of the photodetectors based on organic and inorganic semiconductors and the retinal photoreceptors.

	Polymer photodetectors (excitonic processes)	Silicon photodetectors (band processes)	Retinal photoreceptors (chemical/ionic processes)
Photoresponsivity	~ 0.1 $\mu\text{A W}^{-1} \mu\text{m}^{-2}$ (calculated for a polymer photodetector with a responsivity of 0.1 mA/mW at 660 nm for 10 mm^2 area). Calculated from data presented in ⁷⁰ .	~ 0.5 $\mu\text{A W}^{-1} \mu\text{m}^{-2}$ (calculated for a silicon photodiode with a responsivity of 0.5 A/W at 560 nm for 1 mm^2 area). Data calculated for responsivity of Hamamatsu Si-photodetector S1337 series.	Rods: ~ 10 pA $\text{pW}^{-1} \mu\text{m}^{-2}$ (calculated from 10 pA current response of a cell to a 10 ms pulse of 3000 photons of 550 nm); Cones: ~ 1 pA $\text{pW}^{-1} \mu\text{m}^{-2}$. Calculated from data presented in ⁷¹ .
Spectral response	 (Data for the PCPDTBT:PC ₇₁ BM BHIJ based high responsivity photodetector presented in ⁷²).	 Typical Silicon Photodiode Spectral Response	 Data as shown in ⁷³ .
Intensity dependent response	 Data adapted from ⁷⁰ .	 --- Responsivity = 0.40 A/W	 Data adapted from ⁷¹ .
Temporal response	Rise/Fall time ~ 10-100 ns at 0 V for 10 mm^2 area. Data extracted from ⁷⁴ .	Rise/Fall time ~ 1 ns at 5 V for a 1 mm^2 area. Data for Thorlabs FDS010 silicon detector.	Integration time ~ 100 ms for rods, 20 ms for cones ⁵⁷ .

1.5 Approaches for Retinal prosthesis

Vision loss arising from the retinal degenerative diseases like retinal pigmentosa and age related macular degeneration is caused by the irreversible loss of the photoreceptor layer of the retina. In most of these cases, it has been observed that the inner neurons and their retinal circuitry are preserved^{76,77}. The efforts for eliciting visual perception in such cases are directed towards appropriately stimulating the still functional inner retina. Various research groups are investigating retinal therapeutic approaches like stem cell therapy⁷⁸⁻⁸⁰, gene therapy^{81,82}, optogenetics⁸³⁻⁸⁵, pharmacological solutions^{86,87} and transplants^{88,89}. An alternate visual prosthetic approach is that of the development of bioelectronic retinal implants, which involves electrical stimulation of retinal cells. The methods in this approach utilize the voltage sensitivity of ion channels and electrical signaling processes in the neuronal cells of the retina. The electric stimulation in form of current or voltage pulse excites one or more of the surviving cell classes, resulting in the generation of action potentials in RGCs.

Retinal prosthetic designs can be classified into two primary approaches (**Figure1.15**). The *subretinal approach* involves electrical stimulation of the outer retina at the degenerated photoreceptor side⁹⁰⁻⁹⁴. Silicon based photodetectors have been widely used for this approach. A microphotodiode array is usually implanted at the site of the deteriorated outer retina. When light falls onto the array's photodiodes, the microelectrodes residing in the center of each microphotodiode locally stimulate the preserved inner retinal cells and circuits, which in turn stimulate the ganglion cells. In this approach, the retinal network is stimulated at its natural input level near the photoreceptor layer. The Alpha IMS implant chip from Retina Implant AG (Germany) has been implanted and shown promising results in patients suffering from retinal degenerative diseases.

The *epiretinal approach* involves electrical stimulation of the inner retina by translating the visual field into electrical inputs to an array of metal electrodes located in proximity to the RGCs⁹⁶⁻⁹⁸. This approach results in electrical activation of the RGCs either directly, or indirectly by activation of one or more of the neurons that deliver synaptic input to the ganglion cell (eg. bipolar cells). In the epiretinal prosthesis system, an extraocular

assembly, consisting of an image detector or camera, an encoder and a transmitter, is used. A receiver and a decoder chip in the implant then translate these spatiotemporal signals to the electrode arrays, which in turn stimulate the RGCs with a corresponding stimulus pattern. This method aims to replace the major optical and intra-retinal functions, while directly generating light perceptions in the cortex. Some of these epiretinal implants, like the Argus II retinal prosthesis system from Second Sight Inc. (USA), are already approved for use with patients suffering from retinal degenerative diseases.

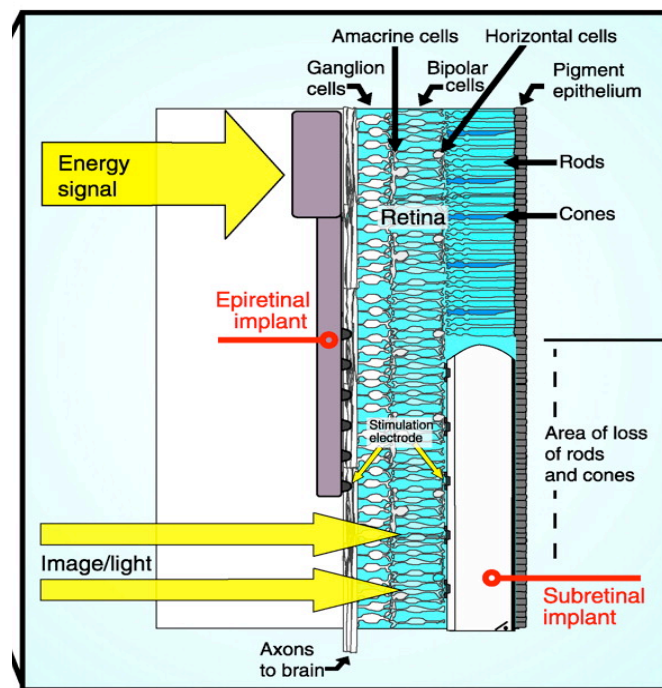


Figure 1.15 Schematic showing the placement of subretinal and epiretinal implants. With a subretinal implant, the subretinal space is placed with a silicon plate carrying light-sensitive microphotodiodes, each equipped with a stimulation electrode. Light from the image directly modulates the microphotodiodes, and the electrodes inject currents into the remaining neural cells (horizontal cells, bipolar cells, amacrine cells, and ganglion cells) of the retinal inner layer. In contrast, the epiretinal implant has no light-sensitive areas but receives electrical signals from a distant camera and processing unit outside of the body. Electrodes in the epiretinal implant (small black knobs) then directly stimulate the axons of the inner-layer ganglion cells that form the optic nerve [Adapted with permission from ⁹⁵].

Most of the components in subretinal and epiretinal implants are composed of inorganic materials or metals, which come in direct contact with the physiological media. Various reports on biocompatibility analysis of these implants have shown that these materials either degrade or result in tissue inflammation scars in the long term. Further, the silicon based microphotodiode arrays in the subretinal implants require an amplifier for delivering the threshold power for subretinal stimulation at ambient light levels⁹⁹. The mechanical and optoelectronic properties of semiconducting polymers make them suitable alternatives to the conventional semiconductor devices for development of bio-optoelectronic interfaces. The work described in this thesis converges to some of these aspects and has strong implications towards development of novel optoelectronic interfaces for artificial retina applications.

The thesis focuses on the integration of biocompatible, semiconducting polymer based photodetectors, working in physiological media, whose optoelectronic signals mimic those of the retinal photoreceptors, with a retinal tissue. The next chapter of the thesis presents the optoelectronic properties of a stable BHJ/electrolyte interface. The photocurrent and photocapacitance measurements highlight the role of bulk carrier concentration, diffusion length scales and transport mechanisms in BHJ/electrolyte structures. The optoelectronic features arising from the interface and transport properties of the BHJ/electrolyte interfaces could be utilized for fabrication of single-pixel color sensing elements and novel biomimicking photodetectors, which have features similar to various naturally occurring photoreceptors. Such photoreceptor-type sensors are suitable candidates to be used as stimulation elements upon interfacing with retinal neurons like the ganglion cells.

Chapter 3 presents the studies where the polymer BHJ layers have been interfaced with a blind retina to evoke visual cues. The BHJ layer coated on a MEA is utilized for stimulating an embryonic stage chick retina with dysfunctional photoreceptors and recording its electrophysiological activity. Our studies demonstrated that the photoexcitation of the BHJ interface with the blind retina in physiological conditions resulted in a neuronal response in the retina, highlighting the efficacy of polymer semiconductors as artificial receptors for interfacing with the visual systems. The BHJ based stimulating platform and the methodology utilized for retinal stimulation has striking advantages over the conventional ways of retinal stimulation reported previously.

Chapter 4 of the thesis discusses the biocompatibility and utilization of BHJ/electrolyte structures as smart interfaces for modifying neuronal growth patterns. The biocompatibility of BHJ layers has been studied by growing dissociated retinal cell culture on the BHJ surfaces for over 10 days *in vitro* and quantifying the cell apoptosis using TUNEL assay. The BHJ surfaces are found to be non-cytotoxic and biocompatible with the retinal cells. Further, photoillumination of BHJ layers during the cell culture period is shown to affect the neuronal growth pattern of dissociated retinal cells. The observations suggest a potential utilization of BHJ layers as interfaces for studying the various synaptic properties within retinal neuronal networks. The last chapter of the thesis covers the summary and future directions of the work.

Chapter 2

Optoelectronic Polymer Device Structures for Intelligent Sensing and Biomimicking Visual Response

The hybrid interface of organic semiconductors with electrolytes has attracted much attention in the last few years due to their potential applications in electrochemical and electrolyte-gated field effect transistors, photoelectrochemical cells, and tandem photovoltaic and dye-sensitized solar cells. Various conjugated polymers and molecules have been demonstrated to work as photosensitive layers in direct contact with aqueous electrolytes. This chapter gives an overview of the characteristic features arising from bulk and interfacial properties of semiconducting polymer/aqueous electrolyte devices. The photocurrent (I_{ph}), photovoltage (V_{ph}) and photocapacitance (C) as a function of various parameters in BHJ/EI structures are presented. The results highlight the role of bulk carrier concentration, diffusion length scales and the presence of different transport mechanisms prevalent in BHJ/EI structures. The characteristic transient profiles of the photocurrents across these device structures are then utilized for fabrication of a single-layer, multi-color detector based on the BHJ/EI interface. The detection is based on appropriate composition and thickness of the BHJ layer in contact with aqueous electrolyte, which results in characteristic polarity and temporal profile of the I_{ph} signals in response to various incident colors. The device conditions closely resemble the environment offered by physiological buffer-solutions and natural visual systems. The device characteristics presented here resemble various features observed in certain natural biological systems, such as bacteriorhodopsin, photosynthetic membranes and mammalian retinas.

BHJ based organic photodetectors have been previously utilized as pixel elements of large-area, color-image sensors in 2-D photodiode arrays^{34,72,100-105}. In general, the color sensing procedure in such devices is based on two primary approaches. The first approach involves combining three separate elements or sub-pixels with photosensitivity tuned to three primary colors¹⁰⁰. This approach involves fabricating structures through an elaborate processing scheme. The second, more common approach involves color-filter arrays (CFAs) as a mask on the monochrome sensor¹⁰⁶. The CFAs absorb a sizeable percentage of the incoming light, and the color at

each position is reconstructed through interpolation algorithms (demosaicing). In this chapter, BHJ/electrolyte based optoelectronic photodetectors are presented, which circumvent the need of sub-pixels or CFAs. The thickness dependence features of the photocurrent from BHJ/electrolyte structures are utilized to create a λ -dependent signal. Upon using an appropriate (or critical) thickness of the BHJ film in the same BHJ/electrolyte device structure, the characteristics of the $I_{ph}(t)$ upon photoexcitation with λ s corresponding to the three primary colors: red, green and blue are presented. In particular, for thick BHJ films ($> 2 \mu\text{m}$), the $I_{ph}(t)$ generated across the BHJ/aq upon photoexcitation (for all λ s) consists of a positive response while devices with BHJ film having thickness less than a critical thickness gave rise to a negative transient signal.

The use of water and aqueous electrolytes (which do not constitute a regenerative redox couple) serves as an effective barrier interface in these device structures, which modifies the electronic photocurrent to characteristic transient profiles, and also mimicks the environment offered by physiological buffer-solutions. The stability of optoelectronic polymer films in contact with water and aqueous electrolytes has been previously reported.^{107,108} The BHJ layers utilized in our experiments constituted P3HT and N2200 as the donor and acceptor polymers. P3HT has been shown to be stable in contact with de-ionized water in a water-gate field effect transistor geometry¹⁰⁹. The naphthalene derivative based polymer, N2200, has also been shown to have enhanced water stability over PC₆₀BM and larger electron mobility¹¹⁰. Even though the phototransduction efficiencies of the devices presented in this chapter are low, the signals emanating from such device structures resemble the features of certain biological visual systems. The results of these studies provide design rules for BHJ based sensors that can be utilized as stimulation elements for retinal neurons like the ganglion cells, which is discussed in the next chapter.

2.1 Details of Materials, Device Fabrication and Measurement Methods

2.1.1 Materials and device fabrication

BHJ films constituted Poly-[3-hexylthiophene] (P3HT) as the donor, and poly{[N,N'-bis(2-octyldodecyl)-naphthalene-1,4,5,8-bis(dicarboximide)-2,6-diyl]-alt-5,5'-(2,2'-bithiophene)}(N2200) as the acceptor. P3HT was procured from Sigma Aldrich, and

N2200 was obtained from Polyera ActivInk, USA. For comparison, another donor polymer, poly-[N-9''-hepta-decanyl-2,7-carbazole-alt-5,5-(4',7'-di-2-thienyl-2',1',3'-benzothiadiazole) (PCDTBT) obtained from Konarka Inc., USA was used. P3HT was occasionally replaced by poly-[3-octylthiophene] (P3OT) (Sigma Aldrich) and no change in results was observed. All polymers were used without additional purification. Chemical structures and relative energy levels of these polymers are shown in **Figure 2.1**.

BHJ blends were prepared in various donor:acceptor ratios (w/w) with chlorobenzene as the solvent (10 mg/ml concentration). However, a ratio of 4:1 (P3HT:N2200) was utilized for the color-detector characterization. Thick polymer films in the ITO/BHJ structure (1.5 μm – 4.5 μm) were prepared by drop casting the BHJ solution on pre-cleaned ITO-coated glass substrates (20 Ω/\square) while thin films (\sim 200 nm) were made by spin casting the blend solution on the substrate at 1000 rpm speed for 100 s. A variation in thickness range 200 nm – 1 μm was achieved by varying the spin coating speed of the substrate. In order to achieve critical thickness ($2 \pm 0.3 \mu\text{m}$) for 4:1 P3HT:N2200 composition, 10 μl volume of the BHJ solution was drop cast from a fixed height of 20 mm onto the ITO substrates, pre-heated at 100°C for 5 min. The thickness of the films was measured using a Dektak stylus profilometer (Veeco Instruments) with a 3 mg force, 12.5 μm tip size and a measurement error of \sim 50 nm. The absorption spectra for thin BHJ films were recorded with UV-vis spectrophotometer.

All devices were fabricated inside glove box (Mbraun Inc.), and annealed at 110°C for 10 min or 80°C for 20 min. De-ionized water, 100 mM KCl, and solvent-free 3-propyl 1-methyl imidazolium iodide (PMII) were used as electrolytes. It should be noted that the term 'aq' is interchangeably used with 'El' in the thesis to represent the interface between a BHJ layer with an aqueous (aq) medium. Polydimethylsiloxane (PDMS) circular wells (diameter \sim 1.5 mm) were used to hold the liquid electrolyte on top of polymer film. ITO, Pt coated FTO glass or Ag/AgCl pellets were used as counter electrodes in contact with electrolyte and were maintained at ground potential for all measurements. The area of these electrodes affected the $I_{\text{ph}}(t)$ magnitudes. In general, ITO glass on the top that covered the entire electrolyte was preferred so that the device area is same as the diameter of the PDMS well.

2.1.2 Fabrication of bilayer devices

Bilayer p/n devices were fabricated using lift-off technique. Due to the non-availability of orthogonal solvents for P3HT and N2200, spin coating method to prepare bilayers was not followed. To fabricate ITO/P3HT/N2200 bilayer, P3HT (10 mg/ml) was spin coated at 1000 rpm on pre-cleaned ITO substrates and annealed at 110°C for 10 min to obtain a P3HT film. Free-standing N2200 films were obtained by introducing the polymer solution (10 mg/ml) onto a layer of de-ionized water. This layer was lifted with the P3HT coated ITO substrate to obtain the P3HT/N2200 bilayer. Similar procedure was adapted to obtain ITO/N2200/P3HT. The obtained bilayer devices were annealed at 110°C for 10 min before putting the PDMS wells and liquid electrolyte for measurements.

2.1.3 Measurement of device photoresponse

Ultrafast LEDs driven by a frequency generator (Sony Tektronix AFG320) were used as light sources. The LED-spectra were measured using spectrometer (Hamamatsu TM-VIS/NIR-CCD C10083CA). The devices were tested on a translational stage with a stage opening such that LEDs could be mounted on either side. Photoillumination was from either ITO/polymer or polymer/EI side. The $I_{ph}(t)$ response across the ITO/polymer/EI structures was recorded with LeCroy (Waverunner6100A) oscilloscope across $1M\Omega$ coupling resistor in dc mode or with an electrometer (Keithley 6512). Since the device resistances were $> 500 M\Omega$, the measurements in oscilloscope are current measurements. The measurements in oscilloscope were taken with a time resolution of 100 μs , while those in electrometer with 33 ms. The $V_{ph}(t)$ response was measured using electrometer (Keithley 6512) in high impedance ($1 G\Omega$) mode. Intensity dependence studies were carried out using a set of neutral density filters with a 532 nm laser. The $C(\omega)$ and $C(V)$ sweeps were recorded with Keithley (SCS4200). The schematic of the set-ups is depicted in Figure 2.1.

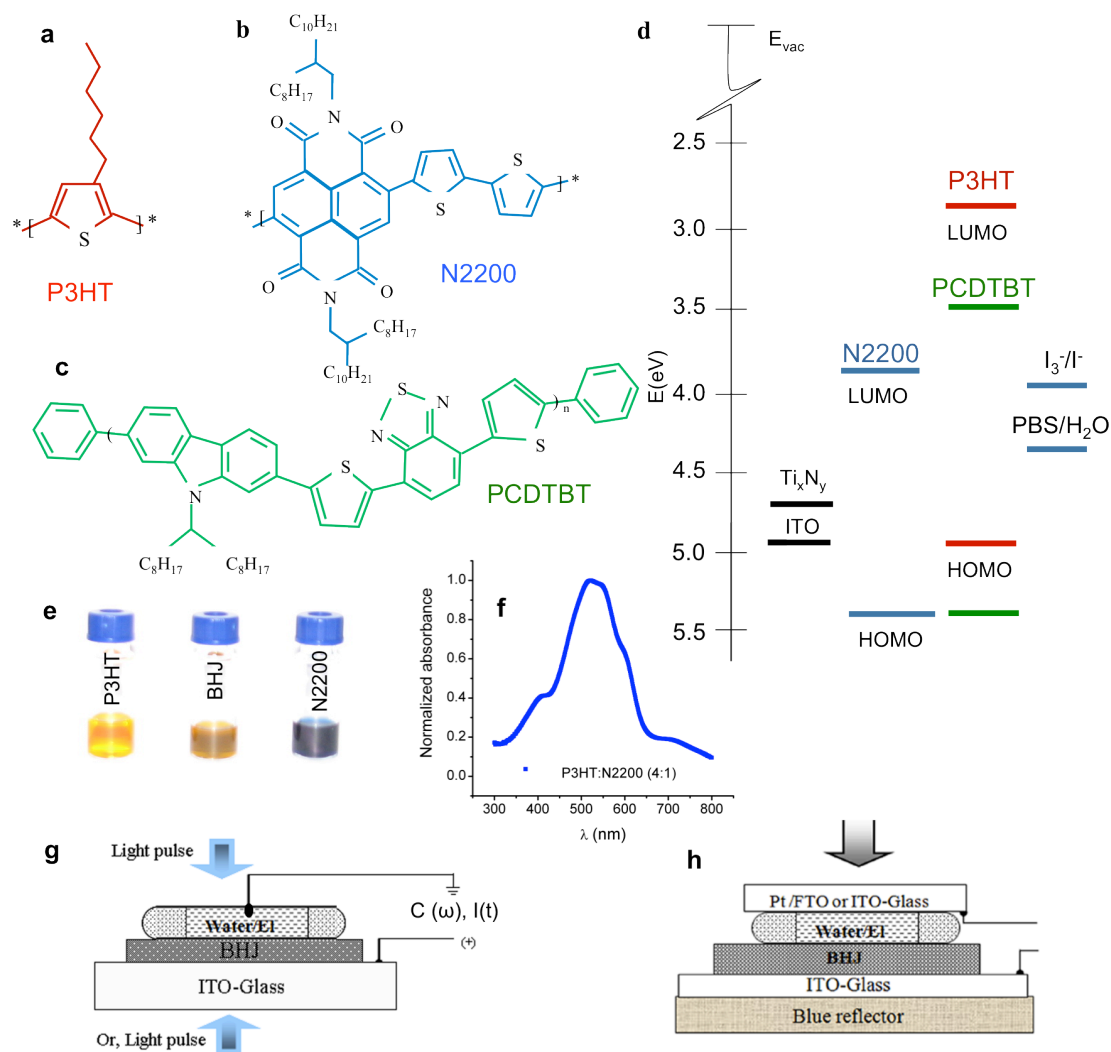


Figure 2.1 Chemical structures of (a) P3HT, (b) N2200 and (c) PCDTBT. (d) Work functions of various materials used in the experiments (e) Solution form of P3HT, N2200 and the BHJ prepared with a 4:1 P3HT:N2200 ratio in 10 mg/ml concentration (f) Absorption spectrum of a BHJ film (g) Schematic of the measurement set-up for photocurrent and photopotential characterization (h) Schematic of the device structure used for three-color sensing.

2.1.4 Device fabrication on MEA

For the multicolor sensing, recordings were done using a MEA with 60 ITO electrodes of 40 μm diameter and 200 μm inter-electrode spacing in an 8X8 arrangement (obtained from Ayanda Biosystems, Switzerland). The details of the MEA recording set-up are previously summarized in Chapter 1, section 1.4.2. The MEA electrodes were checked for any artifacts by recording the baseline with only electrolyte solution. The electrode area of the MEA was drop cast with the polymer BHJ blend at critical thickness. The polymer-coated MEA was annealed at 70°C for

20 min and mounted onto the MEA1060-BC current-voltage amplifier (MultichannelSystems, Germany). 100 mM KCl solution was used as the electrolyte and Ag/AgCl pellet was used as the counter (ground) electrode. White light source focused onto a monochromator grating was used to obtain the visible spectrum onto the MEA using a mirror assembly. The data was acquired at a sampling rate of 25 kHz using a 16-channel data acquisition card and MC_Rack software (Multichannel Systems, Germany).

2.1.5 Electrical recordings from visual photoreceptors

Bacteriorhodopsin (bR) monolayers were prepared using electrostatic layer-by-layer assembly of wild-type bR (obtained from MIB Inc.) on precleaned ITO substrates. The purple membrane patches were suspended in de-ionized water at a concentration of ≈ 0.5 mg/ml, pH ≈ 9.2 with TRIS (tris-(hydroxymethyl)aminomethane) as the buffer to maintain the pH. The pre-cleaned ITO substrates were left in 1:10 APTMS (3-aminopropyl triethoxy-silane):methanol solution for 3 hrs. The ITO substrates were then rinsed with methanol to wash off the excess APTMS and were then immersed in 0.1 M HCl solution for 10 min. This results in a positively charged surface of the substrate, which is then immersed in the purple membrane solution (15 min), by 2 min rinsing process in a buffer solution of equivalent pH and blow dry^{111,112}. These films were characterized by absorption spectroscopy to ascertain the presence of bR. The photoelectric response of unoriented bR monolayer devices in the ITO/bR/KCl geometry was measured using an electrometer and a monochromatic laser light pulse of 532 nm.

Retinal whole mounts were prepared using standard protocols from mice (BL6J/C57). The mice were taken from the postnatal age group P21-30, and sacrificed by cervical dissociation in dark. The eyes were enucleated using forceps and the retina was isolated in reconstituted Ames' Medium (Sigma Aldrich) maintained at 37°C. The explanted retina was placed ganglion side down onto the MEA with 60 ITO electrodes of 40 μm diameter and 200 μm inter-electrode spacing in an 8X8 arrangement (obtained from Ayanda Biosystems, Switzerland), mounted into MEA1060-BC voltage amplifier (Multichannel Systems, Germany). Ames' Medium was used as the perfusate and buffer medium for the retina and Ag/AgCl pellet was used as the counter (ground) electrode. White LED, driven by a function generator (Sony Tektronix AFG320), was used for photostimulation of the retina from the electrolyte side of the MEA. The Vph data was acquired using a 16-channel data

acquisition card and MC_Rack software (Multichannel Systems, Germany) at a sampling frequency of 25 kHz.

2.2 Results – Photoinduced current measurements

A typical I_{ph} response of ITO/P3HT:N2200/EI device structure to a wide square-pulse photoexcitation is shown in **Figure 2.2**. As expected, the photoresponse of the BHJ structure is greater than that from pristine donor polymer. Further, the photoexcitation of BHJ/EI device structures with aqueous electrolyte is in form of transients, and does not result in a pure electronic current (as in dye sensitized solar cells, which involve an electrolyte with a regenerative redox couple like I_3^-/I^-). In a BHJ/EI system, the charge transport in the BHJ layer is electronic, while the charge transport in the EI layer is ionic and the discontinuity at the interface results in a transient response of the I_{ph} . The pulse profiles in time scale \sim ms and negligible steady state current points to the dominant contribution from the ionic charge transport in the EI layer, which in turn results from the electronic processes in the BHJ layer and the charge redistribution at the BHJ/EI interface. These features are discussed in detail in Section 2.4. The I_{ph} measurements across the device structures were carried out upon varying various parameters like direction of photoexcitation, thickness and composition of the BHJ layer, and the wavelength of incident light. The following sections present the results from these measurements, and demonstrate features that were utilized for developing stable, single-pixel multi-color sensing platforms based on BHJ/EI structures.

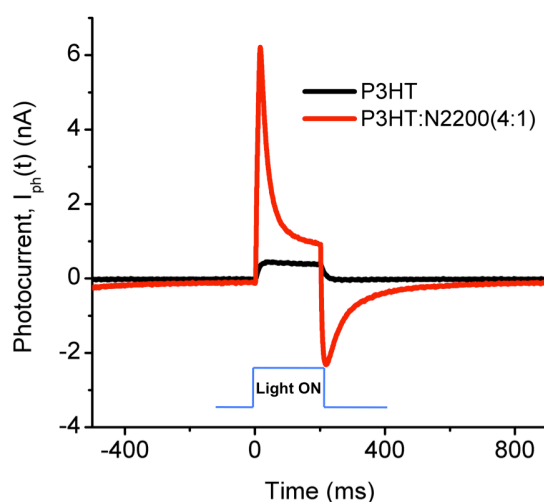


Figure 2.2 Photocurrent across ITO/polymer/PBS compared for 400 nm films of P3HT and BHJ (P3HT:N2200). Signals were measured for a 2.5 mm² area for blue incident light ($\lambda=450$ nm, 250 ms duration) intensity 2 mW/cm².

2.2.1 Direction of Photoexcitation

For light incident from the polymer/EI side, the response of BHJ/EI structures with reasonably thick BHJ layers ($> 2 \mu\text{m}$) is in form of an initial positive I_{ph} spike followed by a steady-state positive value (**Figure 2.3**). For light incident from the ITO side, the response is in form of an initial negative spike followed by a near-zero steady state value. This feature of polarity reversal with incident light direction was observed in the range $400 \text{ nm} < \lambda < 700 \text{ nm}$, which corresponds to the BHJ absorption range. However, upon replacing the donor P3HT with PCDTBT, this trend in the I_{ph} response is not observed. As shown in **Figure 2.3(inset)**, a substantially large positive I_{ph} signal is observed for the PCDTBT:N2200 based BHJ/EI devices for light incident from both directions. The positive polarity of the response from the PCDTBT based structures does not vary with this thickness range and wavelength of incident light. The polarity reversal based on direction of illumination for a thick BHJ film based on P3HT:N2200 points to the role of absorption of light within the active layer, which is a function of thickness.

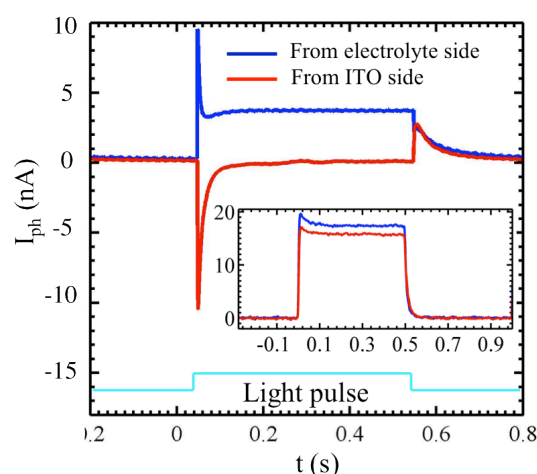


Figure 2.3 Photoresponse from P3HT:N2200 thick films ($\sim 4.5 \mu\text{m}$) in ITO/BHJ/EI structure with KCl (100 mM) electrolyte, shown for two sides of illumination. Inset: Response of the PCDTBT:N2200 based ITO/BHJ/EI device for similar active layer thickness.

2.2.2 Thickness dependent photocurrent response

In case of P3HT based BHJs, the $I_{\text{ph}}(t)$ displays an interesting behavior with respect to the film thickness (**Figure 2.4**). Upon photoexcitation from the BHJ/EI side, the photoresponse of a reasonably thick film ($\approx 4.5 \mu\text{m}$) to $\lambda = 525 \text{ nm}$ is in form of a positive I_{ph} spike followed by a steady-state value. As the film thickness is reduced,

the ratio of spike amplitude (I_{peak}) to its steady-state value (I_{ss}) reduces and for the film thickness ≈ 200 nm, the I_{ph} reverses its polarity and appears in form of a negative spike. A high sensitivity of I_{peak} and I_{ss} to the film thickness (in the 200 nm – 400 nm range) is evident in **Figure 2.4b**, where the ratio of I_{peak} to I_{ss} magnitudes ($|I_{\text{peak}}/I_{\text{ss}}|$) also demonstrates a crossover as a function of thickness. However, in case of PCDTBT:N2200/EI system, the polarity crossover as a function of thickness is not observed in the I_{ph} response within similar BHJ layer thickness range (**Figure 2.4(a-inset)**).

The direction and thickness dependent measurements suggest that the illumination from the top side of a thick BHJ film ($>4 \mu\text{m}$) with any λ results in a positive polarity, while for thin BHJ films ($<0.4 \mu\text{m}$) results in a negative polarity. These measurements point to a thickness range where high absorbing λ (green/blue) will result in a positive polarity, while a less absorbing λ (red) will result in a negative polarity. This forms the basis of two-color detection using these device structures.

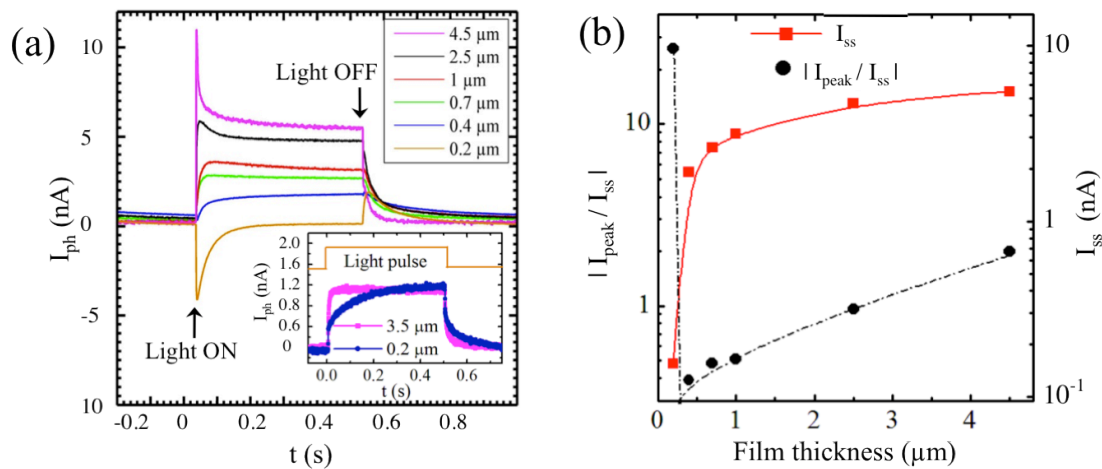


Figure 2.4 (a) Photocurrent response of ITO/P3HT:N2200/EI device structures to a white light pulse incident from electrolyte side for different BHJ layer thickness. (a)-Inset. Photocurrent response of ITO/PCDTBT:N2200/EI device structure to a similar light pulse for BHJ layer thickness 3.5 μm and 0.2 μm , depicting no reversal in polarity. (b) Ratio of the magnitude of the photovoltage spike (I_{peak}) to the steady state potential (I_{ss}) and I_{ss} , as obtained from (a), as a function of film thickness.

2.2.3 Two-color sensing procedure

Upon extending the thickness dependent measurements for $\lambda = 690$ nm, it was noted

that there existed a range of thickness ($\approx 2 \mu\text{m}$ for 4:1 donor:acceptor ratio) where $\lambda = 525 \text{ nm}$ and $\lambda = 690 \text{ nm}$ incident lights gave rise to signals with contrasting polarity – positive and negative, respectively. This criterion of appropriate thickness forms the basis for fabricating a two-color detector, where identification of blue/green and red colors is based on opposite polarity of $I_{\text{ph}}(t)$ of substantial magnitude ($\sim 5 \text{ nA/mW}$) (Error! Reference source not found.5). This phenomenon of two-color sensing was operational for a wide range of intensities ($2 \mu\text{W/cm}^2 - 20 \text{ mW/cm}^2$) and is operable in white background light.

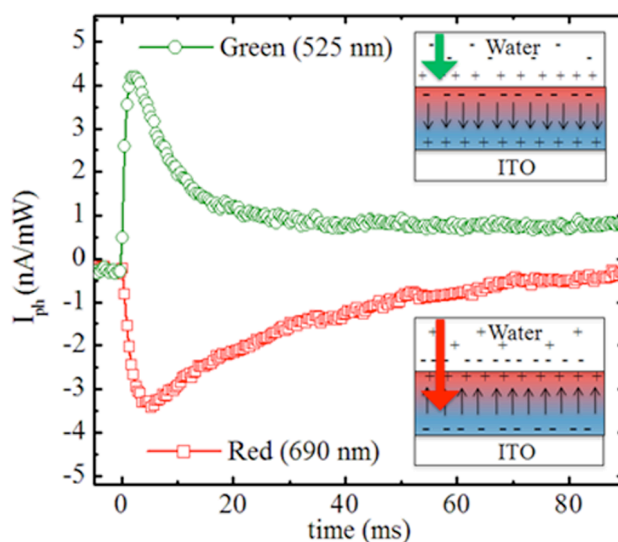


Figure 2.5 Normalized photoresponse of ITO/P3HT:N2200/aq device in a two-color (red and green) detector configuration. The thickness of the BHJ film is $\approx 2 \mu\text{m}$ and the light flash is switched ‘on’ at $t = 0 \text{ s}$. The schematics in the inset depict the mechanism of polarity reversal in response to green (high absorbing) and red (low absorbing) λ s. The color gradient depicting BHJ layer between water and ITO represents the vertical phase segregation of donor and acceptor with acceptor concentration gradient towards the ITO.

Upon measuring the photoresponse in short circuit and open circuit conditions for these device structures, it was observed that the photocurrent mode exhibits a transient signal while the photovoltage mode displays a steady-state potential with the same polarity as that of the current (**Figure 2.6**), indicating the barrier-like capacitive component at the BHJ/EI interface. Either the $V_{\text{ph}}(t)$ or the $I_{\text{ph}}(t)$ measurements are sufficient for two-color detection. However, the transient pulse parameters of $I_{\text{ph}}(t)$ are more informative and therefore used in multi-color detection using BHJ/EI device structures.

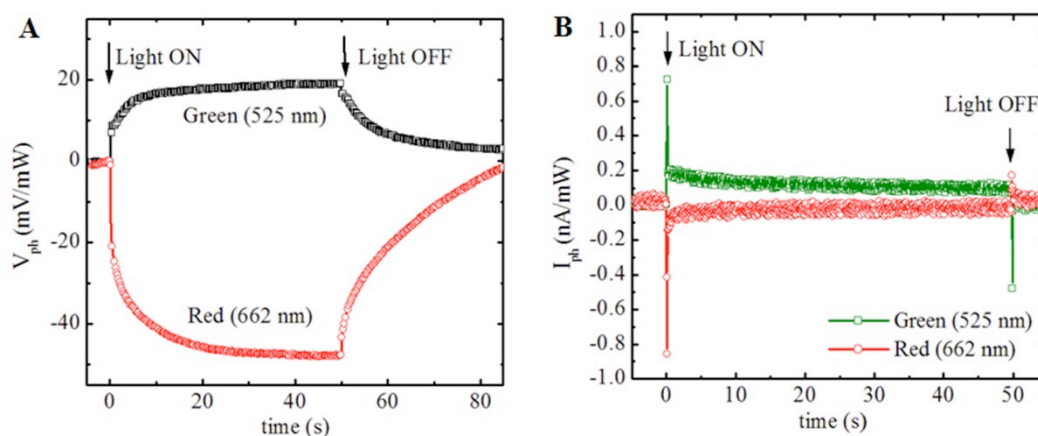


Figure 2.6. Photovoltage vs. photocurrent mode of operation. (A) The photovoltage (V_{ph}) measurement across ITO/BHJ/EI(water) device in open circuit conditions; (B) The photocurrent (I_{ph}) measurement across the same ITO/BHJ/EI(water) device in short circuit conditions, using electrometer (Keithley 6512). The composition of BHJ layer is P3OT:N2200 (4:1 w/w), the thickness of the BHJ layer is $\approx 1.9 \mu\text{m}$ and the illumination is from the aqueous-layer side.

The two-color detection was reproducible over extended cycles of operation (**Figure 2.7**). The stability analysis of the photoresponse of BHJ/aa two-color detectors was done by plotting the ratio of peak value of I_{ph} in response to red light (R_{peak}) to that of green light (G_{peak}) as a function of time (**Figure 2.7**). The ratio assumes a finite value over 1800 s of operation, demonstrating that the color detection property of the device is maintained for sustained period in a white light background.

A comparison of device response to water and KCl as the aqueous medium depicts that the presence of salt in the aqueous medium does not alter the device response. The device response is similar when de-ionized water is used in place of an electrolyte (**Figure 2.8**). Further, the absorption spectrum of BHJ layer retains similar features when the BHJ film is in contact with de-ionized water or aqueous KCl solution, confirming the stability of the BHJ films on exposure to aqueous environments.

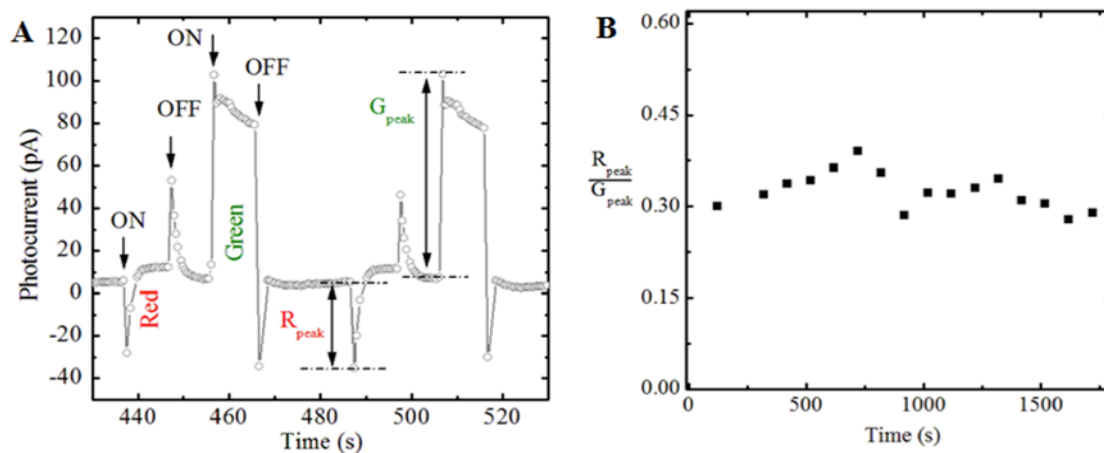


Figure 2.7 (a) The response of BHJ/waer device structure to an alternate red (690 nm) and green (525 nm) light pulse illumination under constant white background, measured using electrometer (Keithley 6512). One illumination cycle corresponds to one red and one green light flash, each for duration of 10 s. The composition of BHJ layer is P3OT:N2200 (4:1 w/w) and thickness of BHJ layer is $\approx 1.9 \mu\text{m}$. (b) The ratio of peak value of photocurrent in response to Red light (R_{peak}) to that of Green light (G_{peak}) is plotted as a function of time.

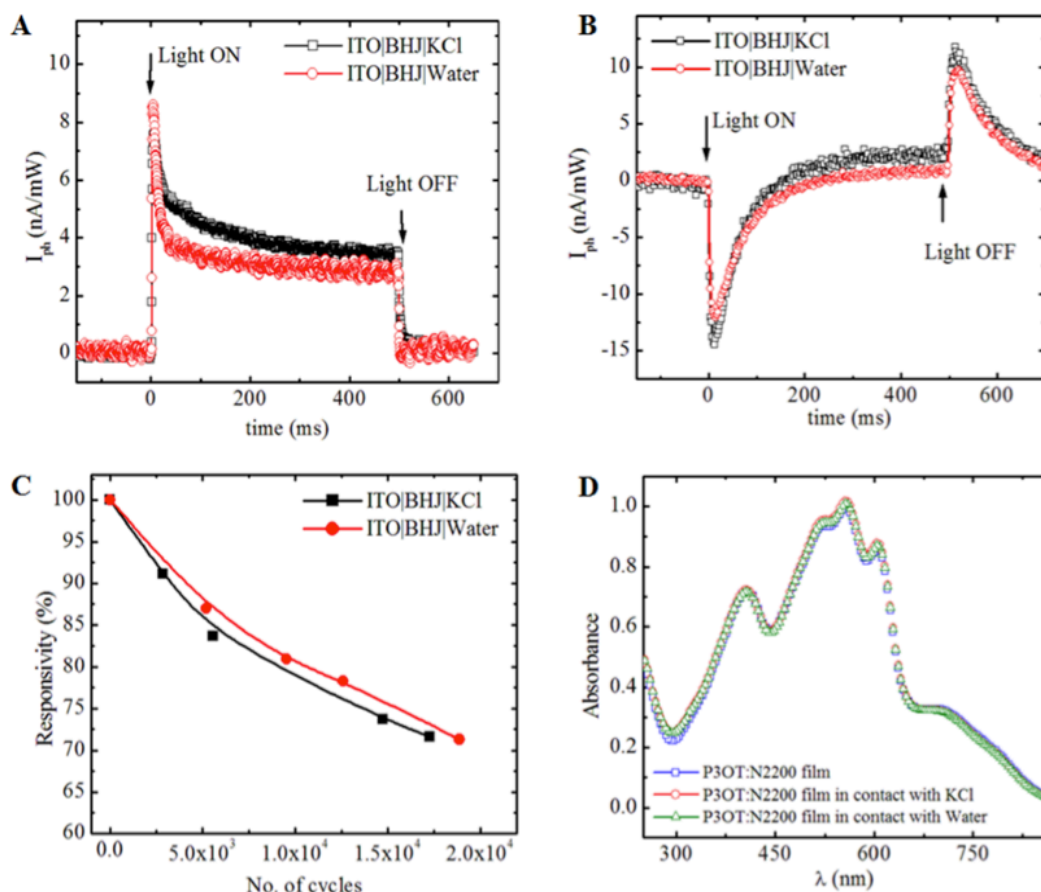


Figure 2.8 Comparison of water and aqueous KCl solution as the aqueous medium (a) The comparison of device response to illumination with $\lambda=525$ nm from the aqueous medium side. (b) The comparison of device response to illumination with $\lambda=525$ nm from the ITO side. BHJ composition is P3OT:N2200 (4:1) and thickness is $3.2 \mu\text{m}$. (c) Stability of device with de-ionized water and KCl solution. The peak value of $I_{ph}(t)$ in response to $\lambda=525$ is plotted as the number of cycles of illumination at a frequency of 3 Hz (~ 160 ms ON, 160 ms OFF). Responsivity is normalized with the peak value of the $I_{ph}(t)$ at $t=0$. (d) Absorption spectrum of P3OT:N2200(1:1) BHJ structure coated on quartz in contact with water and 100 mM aqueous KCl.

The basic two-color detection scheme can be simulated using circuit parameters (**Figure 2.9**). In our circuit simulation, the aqueous layer is taken as a high resistive component, while the BHJ/aq interface is simulated using a capacitor (space charge + Helmholtz), a diode (barrier for holes) and a resistor (leakage pathway). The BHJ layer is simulated using a resistor and a capacitor. The photocurrent I_{ph} is measured in series with a $1 \text{ M}\Omega$ coupling resistor in an oscilloscope (or with 100Ω coupling

resistor in an electrometer). The current source, I , is taken as a step-pulse of 500 ms duration (corresponding to 500 ms light ON duration) and it represents the net diffusion current in the BHJ layer upon photoexcitation. In case of illumination with high absorbing λ (blue/green) from the aqueous side, the hole mediated diffusion current is towards the ITO and is taken as positive ($I = I_{\text{green}} = 900 \text{ nA}$); while for illumination with low absorbing λ (red), the current is towards the aqueous medium side and is taken as negative ($I = I_{\text{red}} = -450 \text{ nA}$). Further, there is a barrier for hole transport towards the aqueous layer due to which the magnitude of negative current is taken smaller than that of the positive current.

The binary logic procedure of two color sensing was extended to three-color sensing. The unique temporal characteristics of I_{ph} response across these devices can be utilized for extending the color detection to multiple wavelengths, as discussed in the next sections.

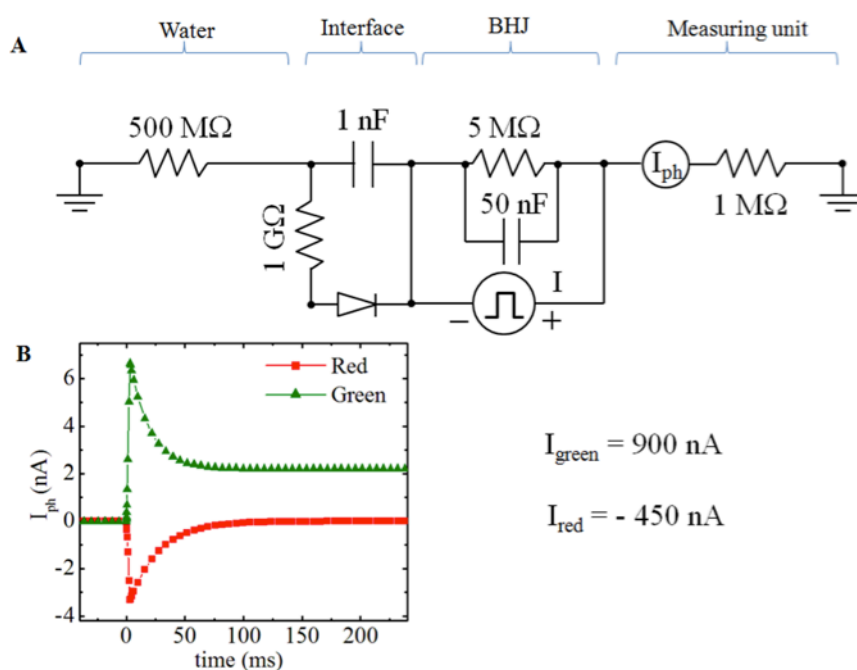


Figure 2.9 Simulation of two-color detection scheme using circuit parameters. (A) The equivalent circuit of a BHJ/aq structure. (B) The simulated response for $\lambda \sim 525 \text{ nm}$ (green) and for $\lambda \sim 630 \text{ nm}$ (red).

2.2.4 Three-color sensing using characteristic response features

As seen in the $I_{\text{ph}}(t)$ measurements, the dynamics of the current rise and decay for the two colors – blue/green and red are quite different. This difference in the

dynamics was combined with a choice of a substrate, which could bring in selectivity in form of an additional reflection of a color band, and was hence utilized to elicit a distinct response to create three-color sensing logic. Using the appropriate thickness of the BHJ layer and a blue selective reflector as the substrate, a three-color detection scheme based on a single-pixel, single-layer, and filter-free optics is demonstrated, as shown in **Figure 2.10a**. The variation of the peak value of $I_{ph}(t)$ as a function of intensity of incident light is observed to be linear at low intensities, while it saturates at higher values and follows a sub-linear behavior (**Figure 2.10a-inset**). The three-color detection can be numerically represented according to the temporal characteristics of the response.

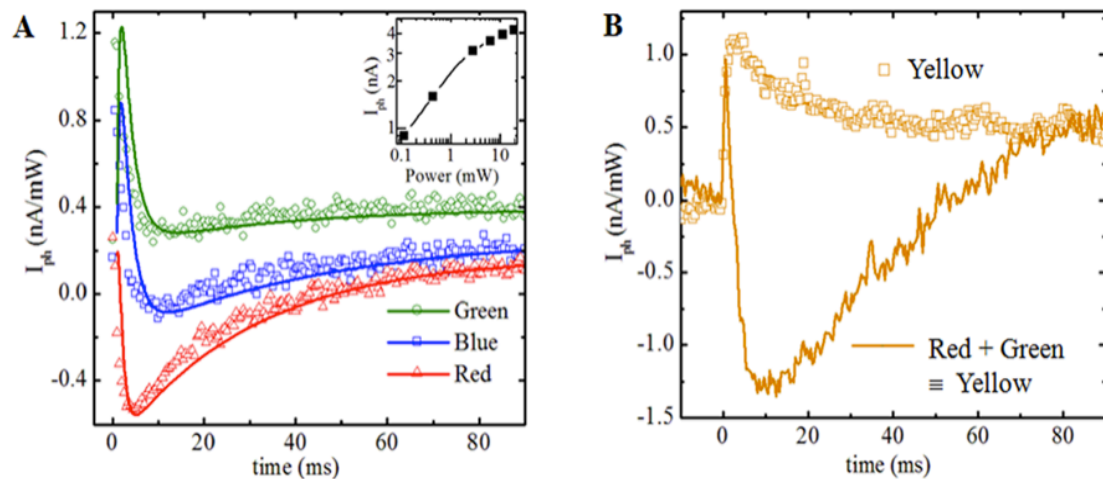


Figure 2.10 (a) Photoresponse of a three-color (red, blue, green) detector device fabricated using a blue selective ($\lambda=470\text{nm}$) Bragg reflector behind the ITO-coated glass. The solid lines correspond to the analog fit to the observed I_{ph} (see text). Inset shows the variation of the peak value of $I_{ph}(t)$ as a function of intensity of incident $\lambda = 532 \text{ nm}$. (b) The response of ITO/BHJ/aq(KCl) device structure to spectral yellow light (575 nm) and to the yellow color obtained from optically mixing the red (690 nm) and green (525 nm) colors. Thickness of the BHJ layer is $\approx 2.1 \mu\text{m}$. The light flash is switched 'on' at $t = 0 \text{ s}$.

2.2.5 Numerical representation of photocurrent profiles

The three-color detection scheme can be formulated upon numerically representing the response pulse. For example, the response to $\lambda = 525 \text{ nm}$ can be expressed as $(1 - e^{-t/\tau_1})e^{-t/\tau_2}$. The time constants τ_1 and τ_2 characterize the rise and decay dynamics of positive $I_{ph}(t)$. The response to $\lambda = 690 \text{ nm}$ can be similarly expressed as

$-(1 - e^{-t/\tau_3})e^{-t/\tau_4}$. The time constants τ_3 and τ_4 characterize the rise and decay dynamics of the negative $I_{ph}(t)$. In the case of incident blue light in presence of a Bragg reflector ($\lambda = 470$ nm) on the substrate, the response can be expressed in form of an algebraic summation of the terms for $\lambda = 525$ nm and $\lambda = 690$ nm along with an additional pre-factor, 'a' and an offset term, 'b' i.e. $I_{ph}(t) = (1 - e^{-t/\tau_1})e^{-t/\tau_2} - a(1 - e^{-t/\tau_3})e^{-t/\tau_4} + b$. This is a generic equation that could be used to fit the I_{ph} response to all three colors in Figure 2.10a, based on the parameters τ , a and b. For instance, for fitting the green color response, parameter 'a' $\rightarrow 0$, and hence the response is dominated by only τ_1 & τ_2 . Similarly, for fitting the red color response, parameter 'a' $\rightarrow 1$ and hence the response is dominated by τ_3 & τ_4 . In case of blue, 'a' assumes an intermediate value, and hence its response has a contribution from all τ_1 , τ_2 , τ_3 & τ_4 . Further, the parameter 'b' corresponds to steady state current values for any color. The relative magnitudes of the fitting parameters as a function of λ are given in **Table 2.1**. Such analog model formalism can possibly be used as a demosaicing tool for three-color detection.

Table 2.1 Parameter values for the mathematical fit for three color detection

Parameter	τ_1 (ms)	τ_2 (ms)	τ_3 (ms)	τ_4 (ms)	a	b
Blue	0.8	2.5	1.0	45	0.25	0.14
Green	0.8	2.5	1.0	34	0.09	0.2
Red	0.8	1.0	1.0	30	0.9	0.18

2.2.6 Possible demosaicing logic

The large dynamic range observed in the λ -dependent response of BHJ/aa systems can be incorporated for digital signal processing. A digital logic using a comparator (comp) circuit can provide signal processing and demosaicing to arrive at the color information (**Figure 2.11**). For the instance shown in the schematic, for green color ($\lambda \sim 530$ nm) response, comp 1 is high for all 4 clock pulses whereas comp 2 is low; for red color ($\lambda \sim 650$ nm) response, comp 2 is high for 4 clock pulses and comp 1 is low. In the case of blue color ($\lambda \sim 460$ nm) response, comp 1 and comp 2 both show high

output for certain clock pulses. The output bit pattern would then be uniquely decoded. In this procedure, the accuracy of color discrimination depends on the clock pulse and the bit size. This circuit is not unique, but a possible logic for digital color demosaicing.

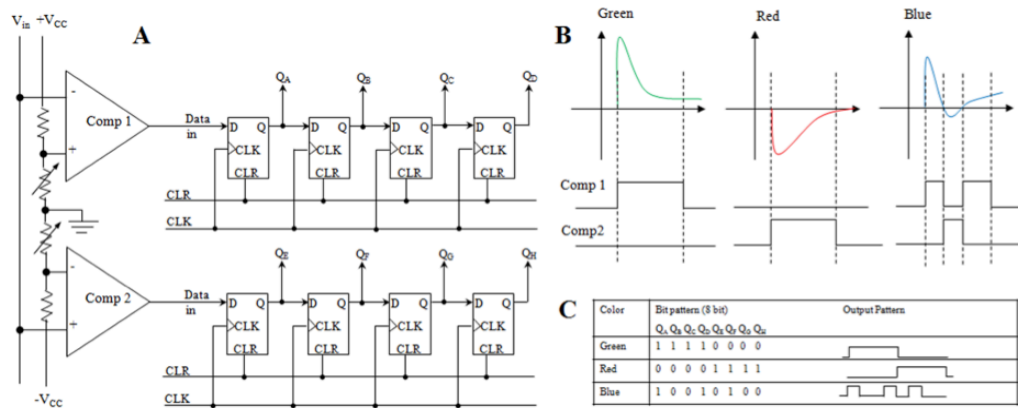


Figure 2.11 Proposed digital electronic circuit for demosaicing. (a) The digital logic circuit including comparators (comp) and 4-bit shift registers, where comp 1 is biased to detect positive photovoltage (V_{ph}) whereas comp 2 is used to detect negative V_{ph} . (b) The output response of comp 1 and comp 2 to the V_{ph} from the device to green, red and blue incident colors for certain clock pulse. (c) The possible output bit pattern of the digital circuit shown for the three colors that can be obtained by using another set of 8-bit shift registers.

2.2.7 Yellow and white color detection

The uniqueness of the analog representation further implies that a natural pure-color can be distinguished from an additive color, i.e. the response to an incident pure-yellow light is different from a response to yellow color obtained from a combination of red and green. Such a comparison from the BHJ/aq device response is depicted in **Figure 2.9b**. Further, the $I_{ph}(t)$ response to illumination with white light does not exhibit the transient spikes as observed with monochromatic pulses (**Figure 2.12**). Unlike in response to the red and green light illumination, the charge carrier generation in case of white light illumination is uniform in the bulk of the BHJ layer and hence the transient spike feature is absent. These results point to the fact that the device response characteristics are unique to the wavelength of incident light, and can be utilized for detecting multiple colors across the visible spectrum.

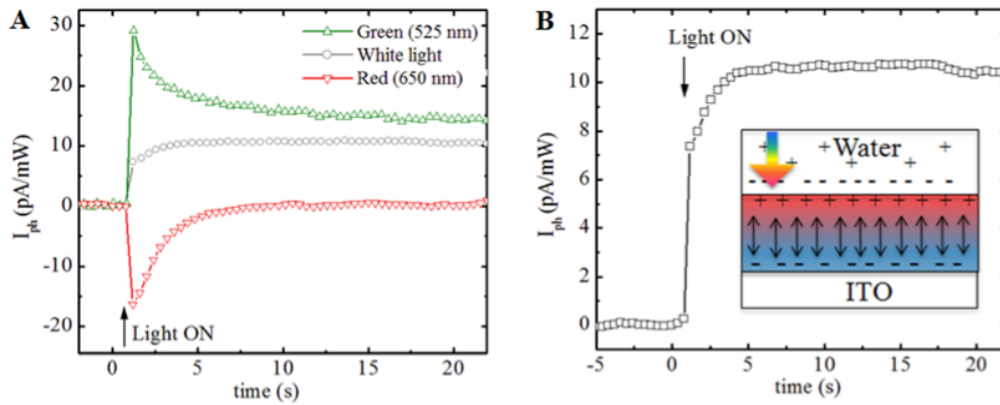


Figure 2.12 (a) The photoresponse of ITO/BHJ/EI(water) device to white light is compared with that to red and green light. The $I_{ph}(t)$ in this case is measured using an electrometer (Keithley 6512). (b) Unlike in response to the red and green light illumination, the charge carrier generation in case of white light illumination is uniform in the bulk of the BHJ layer and hence the transient spike feature is absent.

2.2.8 Multi-color Detection

The variation in pulse response parameters as a function of λ in the entire visible range was gauged by dispersing white light onto a patterned substrate (**Figure 2.13a, b**). The patterned structure consists of a MEA consisting of 60 ITO electrodes forming a square (8X8) layout, each of which are connected to an amplifier. Upon casting the BHJ film of appropriate thickness onto the MEA and using 100 mM aqueous KCl, the amplified response from each of the electrode recorded is shown in **Figure 2.13c**. Each of the pixel response in a given row of the MEA has unique characteristics since positive polarity and the negative polarity signal are not identical and do not compensate to arrive at a zero magnitude. The results validate the utility of the BHJ-based single pixel device to decipher color over a wide range. The λ sensitivity and resolution of this detection scheme are discussed in the next section.

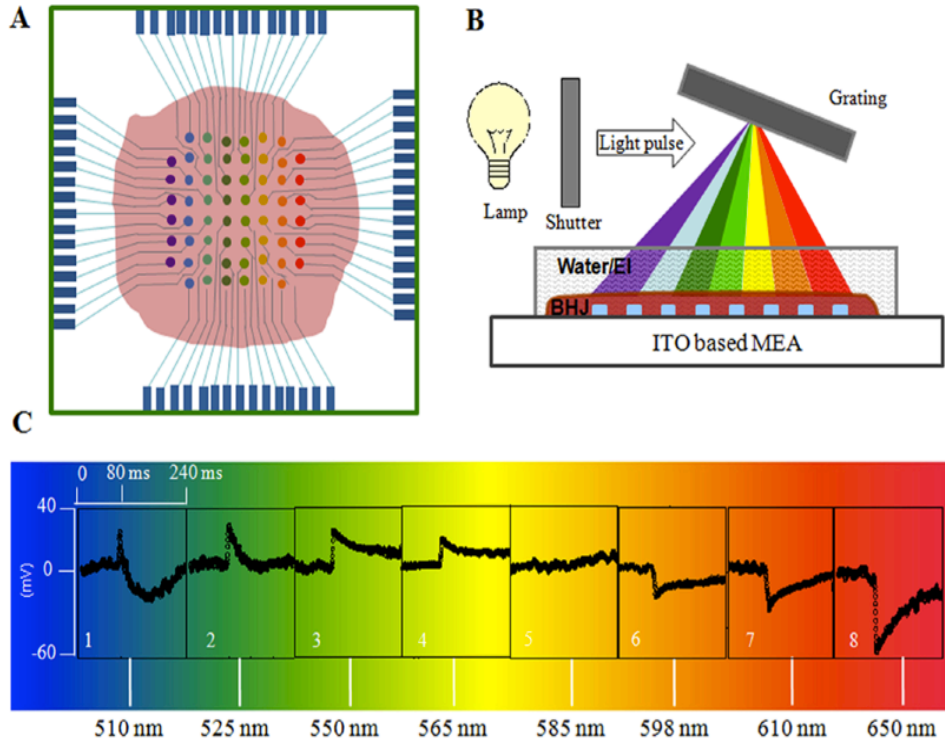


Figure 2.13 (a) Schematic of the 8X8 multi-electrode array (MEA) with 60 ITO electrodes coated with the BHJ layer of thickness $\approx 2 \mu\text{m}$ (equal to L_c , see text). 100 mM aqueous KCl solution is held on top of the polymer film. (b) Various wavelengths of the visible spectrum dispersed onto the array in the manner shown. (c) The photovoltage response of such ITO/P3OT:N2200/aq device as a function of the various λ s of the visible spectrum (λ error bar $\sim 10 \text{ nm}$). The light flash is switched 'on' at 80 ms. Eight windows correspond to the response from each row of the MEA.

2.2.9 Sensitivity and resolution

The typical wavelength resolution estimated for the measurement parameters is limited by the differential sensitivity of the device. We defined sensitivity, $S_\lambda = [I_{\text{ph}}^{\text{max}}(\lambda)]/\text{mW}$. A plot of differential sensitivity ($\Delta S/S = [I_{\text{ph}}^{\text{max}}(\lambda_2) - I_{\text{ph}}^{\text{max}}(\lambda_1)] / I_{\text{ph}}^{\text{max}}(\lambda_2)$) of the device as a function of wavelength (**Figure 2.14**) shows that the maximum sensitivity of BHJ/EI devices is around the λ range 600-625 nm, where the polarity reversal is obtained. Based on the response profiles from the array and the reflection attributes of the substrate, the color discrimination resolution of the single pixel color sensor over the range $400 \text{ nm} < \lambda < 700 \text{ nm}$ is estimated to be of the order of $\sim 20 \text{ nm}$.

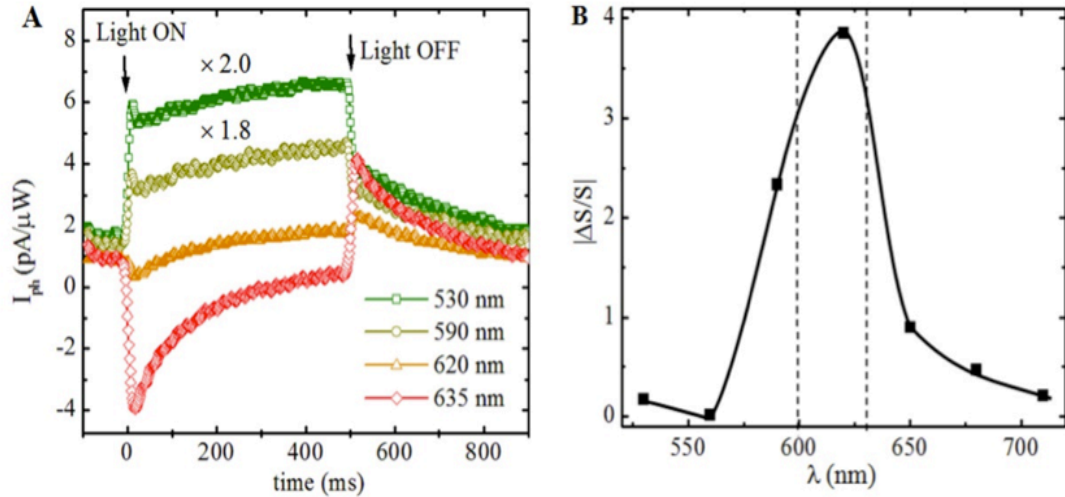


Figure 2.14 Differential sensitivity as a function of wavelength. (A) Transition from positive polarity to negative polarity as a function of wavelength for a ITO/BHJ/aq(100 mM KCl) device. The response is recorded using an electrometer (Keithley 6512). (B) Differential sensitivity, defined as $\Delta S = I_{ph}^{max}(\lambda_2) - I_{ph}^{max}(\lambda_1)$, normalized and plotted as a function of λ . The BHJ composition is P3OT:N2200 (4:1) with a thickness of $\sim 2 \mu\text{m}$.

The origin of λ -dependent polarity can be related to the bulk morphology of the BHJ films at critical thickness. In order to confirm the vertical phase segregation in the BHJ layer, it is instructive to compare the signals across the BHJ/EI devices with those arising from the bilayer structures in contact with aqueous electrolytes.

2.2.10 Response from bilayer devices

The $I_{ph}(t)$ across ITO/P/N/aq or ITO/N/P/aq were compared with that of the ITO/BHJ/aq device by illumination with $\lambda=525 \text{ nm}$ from the ITO side. The response of ITO/N2200/P3HT/aq(KCl) and ITO/BHJ/aq(KCl) devices have negative polarity of the I_{ph} while ITO/P3HT/N2200/aq exhibits a positive polarity when the illumination is from the ITO side (**Figure 2.15**). This response is consistent for all such devices as well as when water was used in place of KCl. Although the magnitudes of I_{ph} across the bilayer devices and BHJ devices are not comparable, which might be due to the poor p:n interface obtained with the transfer printing technique, same polarity of the I_{ph} in ITO/N2200/P3HT/aq and ITO/BHJ/aq devices qualitatively show that the concentration gradient of N2200 is towards the ITO electrode.

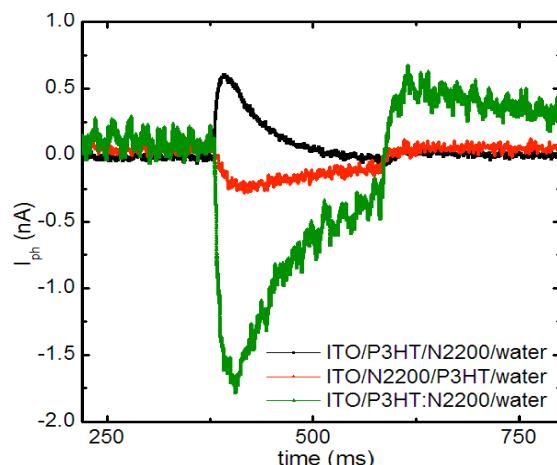


Figure 2.15 Photoresponse of bilayer structures. The response of P3HT/N2200 and N2200/P3HT bilayer structures is compared with that of P3HT:N200 (4:1) BHJ structure, in contact with water. Illumination is by $\lambda=525$ nm from the ITO side. Light pulse is ON at $t=125$ ms.

2.2.11 Photoresponse of biological photodetectors

In order to compare the response of BHJ/aq detectors with naturally occurring photodetectors, photoelectric signals from two natural systems were recorded. The electrochemical recording across a bR layer as well as electrophysiological recording from an isolated mammalian retina is shown in **Figure 2.16**. The photocurrent across the bR layers is in form of transients. The optical response of an isolated retinal tissue is shown in form of an electroretinogram (ERG), which depicts the 'a' wave arising from the stimulation of photoreceptor layer in the retina. The time scales of the pulse profiles resulting from optical excitation of both these systems is \sim ms.

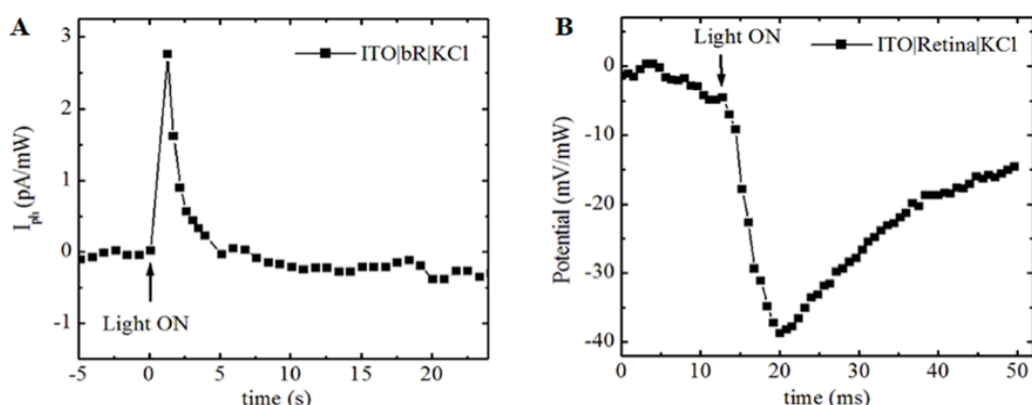


Figure 2.16 (A) Photocurrent across an ITO/bR/electrolyte(100 mM KCl) device. (B) ERG recording from an isolated retina using MEA set-up.

2.2.12 Photocurrent spectra in antagonistic backgrounds

Modulated photocurrent spectra of BHJ/aq devices in dark, blue and red background is shown in **Figure 2.17**. The spectra are taken using a monochromator source pulsed at a frequency of 5 Hz using a high-speed shutter. The modulated photocurrent is recorded using a lock-in amplifier (SRS 830), and is normalized with a silicon photodetector response. In dark background, the device response shows high responsivity in both blue-green and red wavelength region. In red light background, the amplitude of device photoresponse to blue color is a maximum, indicating the enhanced sensitivity to blue color with prior exposure to red light and vice-versa.

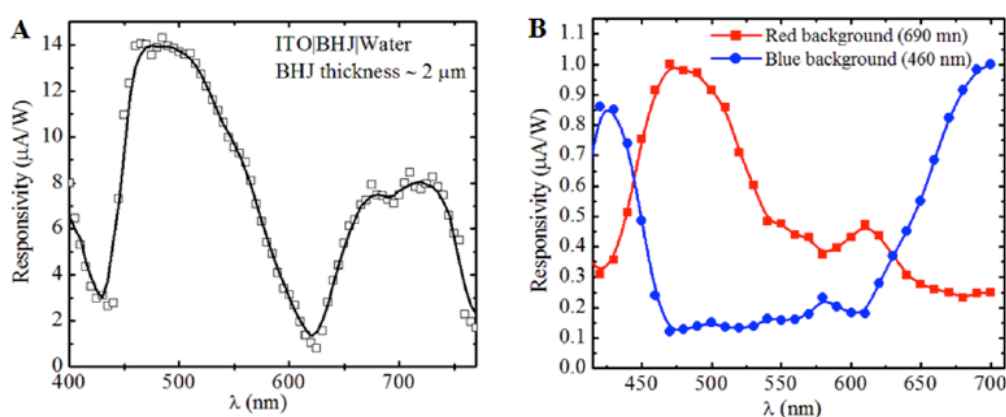


Figure 2.17 Modulated photocurrent spectrum of BHJ/aq photodetector. (A) Modulated photocurrent spectrum of the ITO/BHJ/aq(water) device with BHJ thickness $\sim 2 \mu\text{m}$ in dark background. (B) The photocurrent across the ITO/BHJ/aq(100 mM KCl) device with critical BHJ film thickness ($\sim 2.1 \mu\text{m}$) in antagonistic color backgrounds.

2.3 Results - Photocapacitance Measurements

Using differential $C(\omega)$ measurements over a large ω range (10 kHz - 1 MHz) we observed the existence of a crossover ω in BHJ/EI structures beyond which the electrolyte properties dominate the device characteristics. In general, $C(\omega)$ of BHJ/EI based devices monotonically decreases with increasing ω in 10 kHz - 1 MHz range (**Figure 2.18**). The main features of these measurements are described below.

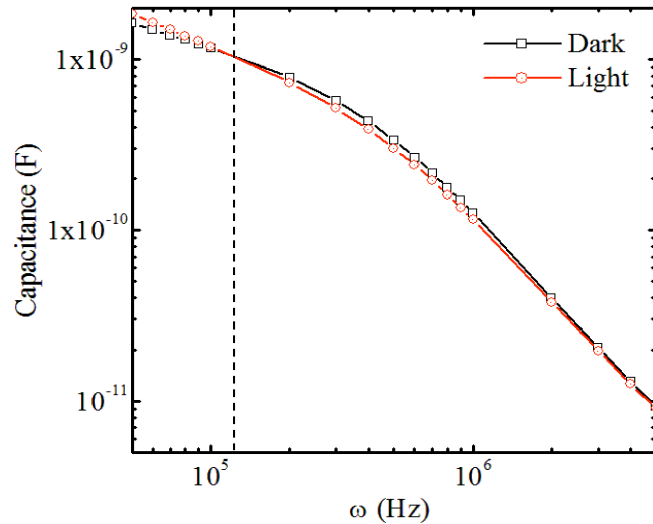


Figure 2.18 Frequency (ω) dependence of a ITO/P3HT/EI device for thin polymer film (~ 200 nm) with 100 mM KCl concentration in dark as well as under white light illumination. The crossover frequency (ω_c) is shown at 125 kHz. Capacitance follows a power law behavior as $C \propto \omega^{-\alpha}$ where $0 < \alpha < 1$ for low frequency and $1 < \alpha < 2$ for high frequency. Similar curves are obtained for thick films ($> 2 \mu\text{m}$) as well.

2.3.1 Differential photocapacitance

Photoexcitation of the P3HT:N2200 based BHJ/EI structure results in a change of $C(\omega)$, where at low ω , $C_{\text{light}} > C_{\text{dark}}$ and at high ω , $C_{\text{light}} < C_{\text{dark}}$ (**Figure 2.19a**). The differential photocapacitance $\Delta C/C_{\text{dark}}$, where $\Delta C = C_{\text{light}} - C_{\text{dark}}$, is observed to change from a positive to negative value as ω is increased from 10 kHz to 1 MHz (**Figure 2.19b**). This crossover of the polarity change of $\Delta C/C_{\text{dark}}$ occurs at a critical frequency, ω_c . The magnitude of ω_c is dependent on the following factors:

- (i) BHJ Composition: ω_c is observed to shift to the higher magnitude in the case of more efficient PCDTBT:N2200 (**Figure 2.19a(inset)**) in comparison to P3HT:N2200 BHJ/EI structures or pristine P3HT/EI structures (**Figure 2.20**).
- (ii) Film thickness: ω_c increases with increasing film thickness $200 \text{ nm} < x < 2 \mu\text{m}$) [**Figure 2.21a**].
- (iii) Electrolyte concentration: ω_c increases with the electrolyte concentration (10 mM – 100 mM) [**Figure 2.19b, Figure 2.21b**].

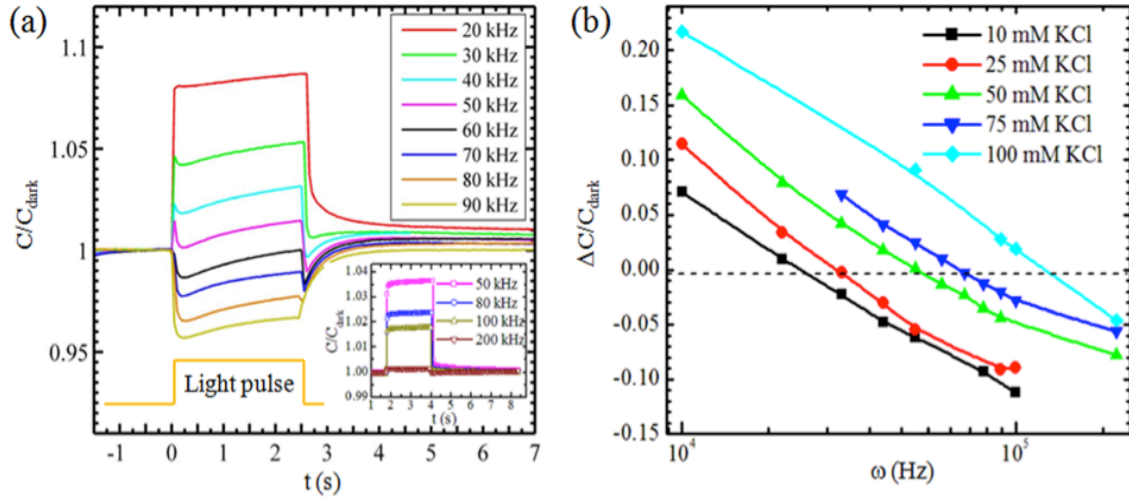


Figure 2.19 (a) Photocapacitance observed for ITO/P3HT:N2200/EI structure at different ω . Inset- Photocapacitance observed for ITO/PCDTBT:N2200/EI structures. 100 mM KCl is used as electrolytes for both cases. (b) Differential photocapacitance $\Delta C/C_{\text{dark}}$ obtained from (a) plotted as a function of ω for various electrolyte concentrations.

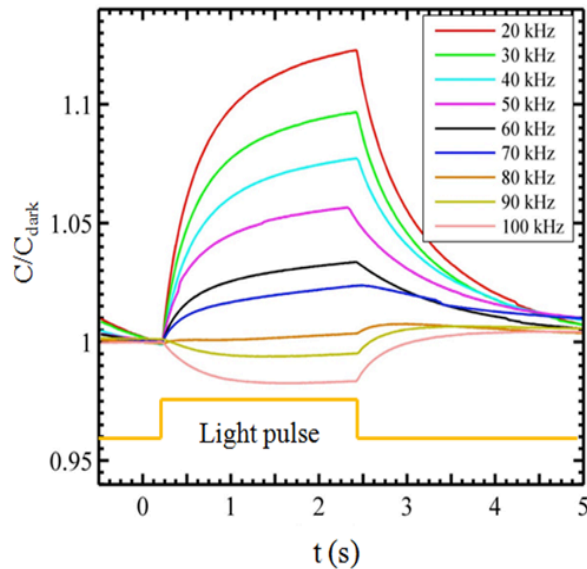


Figure 2.20 Normalized photocapacitance of a ITO/P3HT/EI structure for PMII as the electrolyte and Pt as the counter electrode. The film thickness is ~ 400 nm. The response times are observed to be slower in comparison to the BHJ/EI structures.

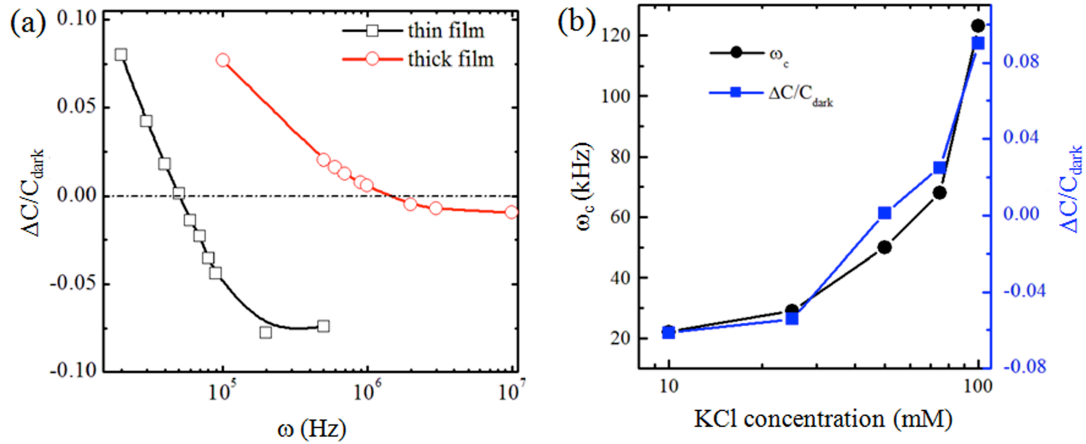


Figure 2.21 (a) The critical frequency (ω_c) shifts to a higher value with increasing thickness of the BHJ layer in ITO/P3HT:N2200/EI device with KCl electrolyte. The KCl concentration is 50 mM; thin film ~ 400 nm and thick film ~ 4 μm . (b) ω_c measured for different concentration of KCl solution for ITO/P3HT:N2200/EI device. ω_c shifts to a higher value with increasing electrolyte concentration. Also shown is the variation of differential photocapacitance ($\Delta C/C_{\text{dark}}$) with electrolyte concentration. At a fixed probe frequency (50 kHz), $\Delta C/C_{\text{dark}}$ increases with increasing electrolyte concentration.

2.3.2 Capacitance-Voltage Measurements

Considerable insight into the ω dependence is obtained from $C(V)$ measurements. Since the analysis of $C(V)$ is less complex for the unipolar pristine systems compared to the ambipolar BHJs, the trend of $C(V)$ was studied at different ω for P3HT/EI structures (**Figure 2.22**). At low ω (around 10 kHz), the $C(V)$ curve follows the expected curve for p-type semiconductor as shown in **Figure 2.27a**. At high ω (around 100 kHz), the $C(V)$ curve changes its slope in the positive bias region. There is a crossover ω at which this transition occurs and is found to be same as ω_c related to the crossover of the $\Delta C/C_{\text{dark}}$. Measurements in such high ω regimes have not been reported previously for organic semiconductors.

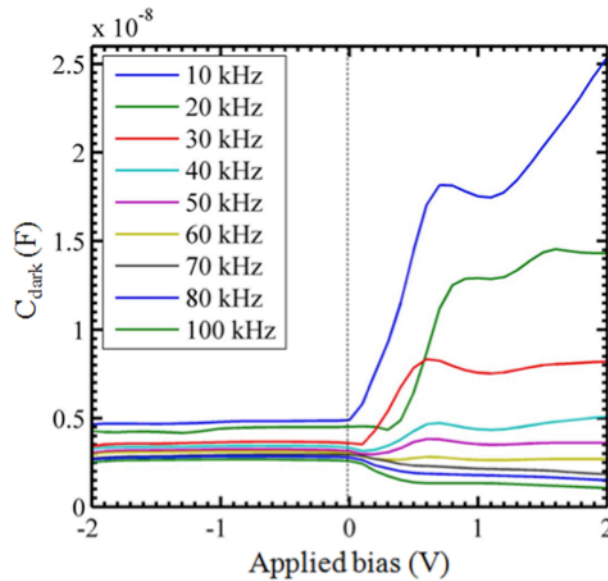


Figure 2.22 $C(V)$ plots obtained at various frequencies ω for P3HT/PMII polymer/EI structure, in non-illuminated conditions. The slope of the plot gets reversed at high ω .

2.4 Microscopic origin of the photoinduced response

The essential features arising from the measurements of the BHJ/EI structures are the following: (i) The I_{ph} spike-polarity exhibits a crossover as a function of BHJ layer thickness, and (ii) $\Delta C/C_{dark}$ and $C(V)$ exhibit a crossover as a function of ω . These results can be understood by a device model, which comprises of a photoactive layer, and discrete but coupled capacitive layers. The light incident-direction dependent polarity of the I_{ph} spike is controlled by the charge transfer/accumulation efficiency to the electrode/electrolyte along with the extent of photogenerated carrier diffusion. Photoexcitation of BHJ/EI with thick polymer films ($> 2 \mu\text{m}$) from the electrolyte side results in the generation of charge carriers largely at the polymer/EI side. The interface energetics are expected to be conducive for electron transfer from the semiconductor bulk (lowest LUMO level – 3.3 eV) to the electrolyte layer, while the photogenerated holes diffuse to the ITO electrode. The large prominent spikes associated with the initial response to the photoexcitation arise from the barrier, which facilitates the electron accumulation; and the dynamics associated with the hole collection at the electrode. The photoexcitation of BHJ/EI with thick polymer films ($> 2 \mu\text{m}$) from the ITO side results in a net positive charge accumulation at the counter electrode side relative to the ITO side in form of a negative spike.

The thickness dependent polarity reversal of I_{ph} in P3HT:N2200 structures can be

quantitatively explained by the differences in the charge transport dynamics (electrons versus holes) accompanied by the ionic processes and is a function of thickness of the BHJ layer. The I_{ph} of a device can be estimated from the electrons and holes concentrations at the ITO/polymer interface using the proposed diffusion model.

Estimation of I_{ph} and critical BHJ thickness, L_c from the diffusion equations

Light intensity at a distance x from BHJ/EI interface (neglecting the reflection term from the ITO/polymer interface) is given by $I_0 \exp(-\alpha x)$ where I_0 is the incident light intensity at the PEI and α is absorption coefficient. The exciton generation then takes

the similar form: $G = G_0 \exp(-\alpha x)$. At steady state, the carrier concentration is further modified by the monomolecular and bimolecular recombination terms. Assuming negligible trap-states, the hole concentration, p at given time can be estimated by

solving the equation: $\frac{dp}{dt} = G - \frac{p}{\tau_p} - pn\gamma$, where τ_p is the hole lifetime, n is the

electron concentration and γ is the bimolecular recombination rate. If the effective diffusion length of electrons and holes are L_n and L_p , then $p(x)$ ($x > 1/\alpha$) can be written as

$$p(x) = p_0^{eff} e^{(-x/L_p)}$$

$$n(x) = n_0^{eff} e^{(-x/L_n)}$$

where p_0^{eff} and n_0^{eff} are the effective hole and electron concentrations at the polymer/electrolyte interface at a given time (say $t = \tau_{tr}$, the transit time).

Using drift-diffusion model for electrons and holes, where μ_n and μ_p are the electrons and holes mobilities, D_n and D_p are the diffusion coefficients and E is the built-in field, the current density for electrons and holes is given by:

$$J_n = q[n(x)\mu_n E + D_n \nabla n(x)]$$

$$J_p = q[p(x)\mu_p E + D_p \nabla p(x)]$$

Total current due to electrons and holes can then be written as

$$J = J_p - J_n$$

$$= qE[p(x)\mu_p - n(x)\mu_n] + q[D_p \nabla p(x) - D_n \nabla n(x)]$$

Substituting $p(x)$ and $n(x)$, we obtain:

$$J = qE\left[p_0^{eff}(x)e^{(-x/L_p)}\mu_p - n_0^{eff}(x)e^{(-x/L_n)}\mu_n\right] + q\left[D_p \nabla p_0^{eff}(x)e^{(-x/L_p)} - D_n \nabla n_0^{eff}(x)e^{(-x/L_n)}\right]$$

Assuming drift component of the photocurrent (as film thickness is $\sim \mu\text{m}$) to be very small compared to diffusion current; and substituting $D = \frac{\mu k_B T}{q}$ we get:

$$J = -\frac{\mu_p k_B T}{L_p} p_0^{eff} e^{(-x/L_p)} + \frac{\mu_n k_B T}{L_n} n_0^{eff} e^{(-x/L_n)}$$

The photocurrent of a device can then be estimated from the electrons and holes concentrations at the polymer ITO interface. For a characteristic thickness $x = L_c$, I_{ph} is observed to be zero, which leads to:

$$L_c = \frac{\ln\left[\frac{(L_p \mu_n n_0^{eff})(L_n \mu_p p_0^{eff})}{(1/L_n - 1/L_p)}\right]}{(1/L_n - 1/L_p)}$$

As shown in Error! Reference source not found.23, the effective carrier concentration is dominated by holes for $x > L_c$ and by electrons for $x < L_c$ where x = thickness of the BHJ layer and L_c = critical thickness. Upon assuming $n_0^{eff} \approx p_0^{eff}$, L_c can be simplified to:

$$L_c \approx \frac{L_n L_p}{(L_p - L_n)} \ln\left(\frac{L_p}{L_n}\right)$$

The observed value of $L_c = 300$ nm. The presence of a finite steady state signal which appears to plateau in samples as thick as $4 - 5 \mu\text{m}$ is indicative of $L_p \sim$ film thickness. This assumption in turn leads to a value of $L_n \sim 70$ nm from the above expression.

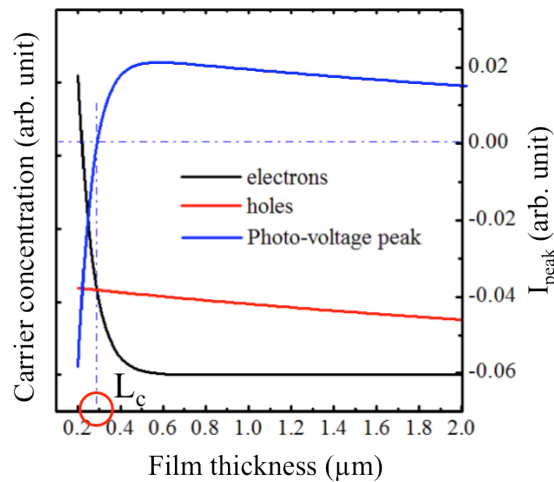


Figure 2.23 Effective carrier concentration at the ITO/BHJ interface with light incident from EI side and the photocurrent peak value (I_{peak}) as modeled from the drift-diffusion equation.

In case of the PCDTBT:N2200 structures, both the features of significant I_{ph} spike and polarity reversal are absent in the measured intensity and time scales. These trends largely point to a barrier free interface in case of PCDTBT/EI compared to P3HT/EI and can be ascribed to the lower solvent reorganization energy at the PCDTBT/EI interface. Further, the response of the BHJ/EI combination is lower than that arising from a BHJ/EI combination where the electrolyte constitutes a regenerative redox couple like I_3^-/I^- . As expected, the more sizable response of BHJ/EI(I_3^-/I^-) device does not have the feature in form of the transient I_{ph} spike observed for electrolyte devices (**Figure 2.24**). The slower photoresponse due to the presence of ionic transport in the BHJ/EI(KCl) devices obviously is not suitable for photovoltaic applications but the significant responsivity and the thickness dependent polarity features make this system an interesting photodetector that can be used in a biological environment besides its use as a model structure for understanding the limitations and transport barriers in hybrid electronic/ionic systems.

The interfacial barriers, and differences in the rate of carrier accumulation at the BHJ/aq interface and ITO/BHJ interface device structures give rise to transient form of photocurrents, and the polarity varying signals. The thickness of the BHJ layer and the absorption coefficient of the incident light, $\alpha(\lambda)$, are crucial tuning parameters for the color discrimination. Photoexcitation of thick polymer films ($> 2 \mu\text{m}$) from the aqueous-layer side (for all λ s) results in the generation of charge carriers largely at the BHJ/EI interface and hole diffusion towards the BHJ/ITO interface, resulting in a positive polarity of the $I_{ph}(t)$. For thin polymer layer devices ($< \sim 200 \text{ nm}$), the higher rate in the accumulation of excess negative charge carriers at the BHJ/ITO interface results in negative polarity of $I_{ph}(t)$. At the optimum film thickness, photoexcitation by a high and low absorbing λ appears in the form of polarity reversal. Consequently, at the critical thickness ($\sim 2 \mu\text{m}$), the charge carrier generation due to shorter λ (blue/green) produces a positive polarity of $I_{ph}(t)$, while higher λ (red) produces a negative polarity of $I_{ph}(t)$. It should be noted that the value of the critical thickness is inversely dependent upon the concentration of N2200 in the BHJ layer and can be utilized for tuning the device; for instance the critical thickness for the BHJ with P3HT:N2200 composition in the ratio 4:1 is $\sim 2 \mu\text{m}$ while the value for a 1:1 ratio was found to be $\sim 200 \text{ nm}$.

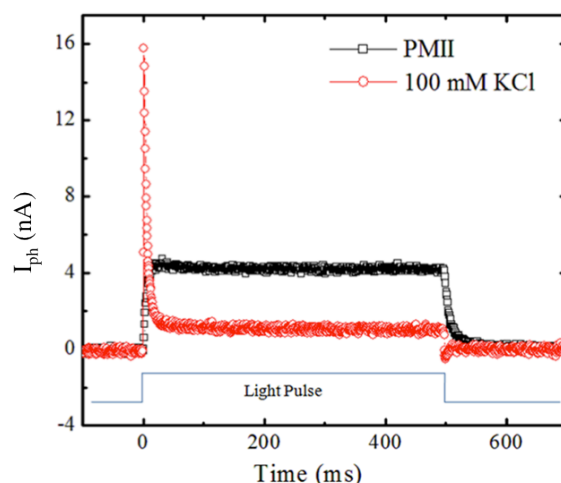


Figure 2.24 Photocurrent response of ITO/BHJ/EI device compared for two types of electrolytes : 3-propyl 1-methyl imidazolium iodide (PMII) and 100 mM KCl. The BHJ layer consists of P3HT:N2200 (1:1) with film thickness $\sim 5.4 \mu\text{m}$. Device is illuminated from electrolyte side with white LED pulsed at 1 Hz (on duration - 500 ms). PMII is a room temperature ionic liquid constituting the regenerative redox couple I^-/I_3^- . The higher magnitude of the steady state photovoltage and the absence of the transient response in BHJ/PMII devices point to the notion that the charge transport within PMII electrolyte layer is electronic, while that within KCl is ionic.

The thickness and λ dependent polarity reversal of $I_{\text{ph}}(t)$ appears to be present only in certain combination of donor-acceptor systems, for instance the features were not noticed in carbazole based PCDTBT donor systems. The λ -dependent polarity reversal at critical thickness, and direction dependent polarity reversal for thick films in the P3HT:N2200 based BHJ layers point to a vertical distribution of donor and acceptor concentrations, with the enrichment of acceptor distribution away from the aqueous layer interface, towards the ITO. The vertical distribution and the interface layer composition is evident upon comparing response of BHJ/EI devices with those of the P3HT/N200/EI and N2200/P3HT/EI bilayer structures (Figure 2.15). This type of vertical distribution is consistent with the low power conversion efficiency and low quantum yield ($< 15\%$) obtained for P3HT:N2200 solar cells¹¹³. Unlike PC_{60}BM , N2200 is a polymer with tendency to form an organized microstructure^{114,115}. In case of light with λ in the low-absorption region (690 nm) incident from the aqueous side of the BHJ/aq structure which is P3HT-rich, the absorption in the vicinity of ITO/BHJ with a predominant N2200 network then results in electron accumulation at this interface and gives rise to a negative $I_{\text{ph}}(t)$. The charge transport in the thick active layer ($\sim 2 \mu\text{m}$) is predominantly by diffusion processes, which are accompanied by the gradient in the distribution of the D/A phases. These physical processes give rise to the feature of polarity reversal for green and red light

illumination (schematically represented in **Figure 2.25**), and are consistent with all the observations. These features also suggest that upon illumination with white light, the generation of charge carriers is comparatively more uniform in the bulk of the BHJ layer resulting in the absence of the transient features in $I_{ph}(t)$ (schematically represented in **Figure 2.12b-inset**). In order to discriminate between the blue and green color responses, we utilized the fact that illumination from the ITO/BHJ side results in a negative polarity of $I_{ph}(t)$. Therefore, presence of the λ -selective reflector (470 nm) on the rear side of the ITO-coated substrate results in a characteristic signal i.e., a positive $I_{ph}(t)$ followed by a negative $I_{ph}(t)$ for $\lambda \sim 470$ nm.

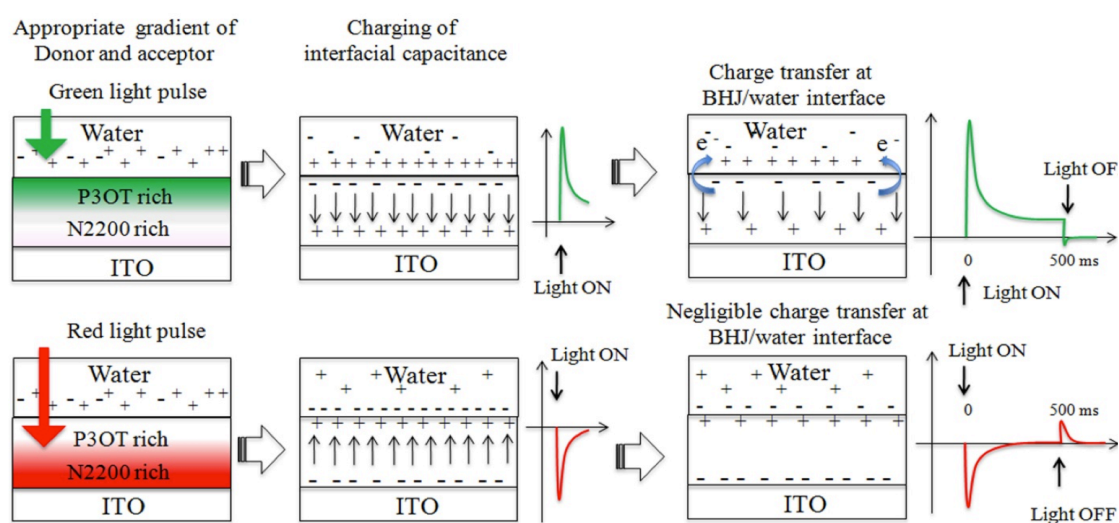


Figure 2.25 Schematic showing the mechanism of polarity dependent color discrimination using the BHJ/EI devices.

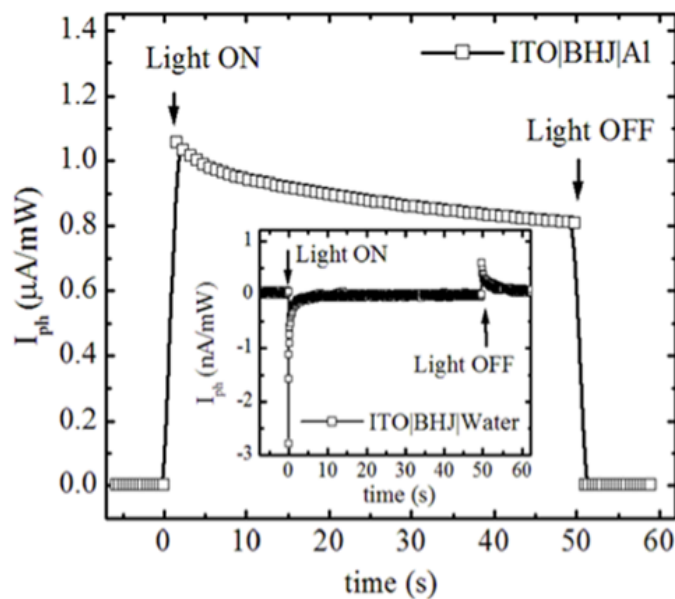


Figure 2.26 Comparison of BHJ/aq device response with that of a solid-state device is depicted. The inset shows the response of ITO/BHJ/aq(water) and ITO/BHJ/Aluminum device with $\lambda=525$ nm from the ITO side, where the thickness of the BHJ layer is ~ 450 nm.

The positive steady state I_{ph} upon illumination with shorter λ (blue/green) can arise from the energetically possible photoinduced electron transfer from the BHJ layer to the aqueous-layer. The explanation of the BHJ layer as a photoelectrode has been utilized previously in the context of interfacial redox processes ^{116,117}. The small magnitude of the steady-state current, prolonged stability and the lower intensity in the present case however points to a relatively smaller contribution from these processes.

In the absence of the aqueous layer and hence the interfacial barrier in a solid-state device, the negative polarity as well as the sharp transient spikes are absent and a huge steady state I_{ph} is observed (**Figure 2.26**). Further, $I_{ph}(t)$ arising from diffusion processes in ITO/BHJ/EI devices is lesser in magnitude compared to the solid state devices due to the presence of the BHJ/EI interface which causes accumulation of charge carriers and promotes recombination under constant illumination. The contribution of such bimolecular recombination processes can also be observed by noting the asymmetry in the charging and discharging I_{ph} profiles across the BHJ/EI devices.

The dynamics involved in the device response can modeled to arise from the

combination of intrinsic processes and the macroscopic equivalent circuit parameters¹¹⁸. The net current arising due to the electronic and hole transport in the polymer bulk in response to photoexcitation can be simulated using a current source whose polarity is dependent on λ and other relevant circuit parameters. The spectral range of operation of these devices covers the entire visible range as seen in the modulated photocurrent action spectrum of ITO/BHJ/EI detectors. Further, the observed time scales in the *ms* range are suitable for designing simple analog electronic circuits. It should be noted that the parameters of quantum efficiency and the spectral sensitivity curves used to characterize conventional photodetectors and colorimeters are not directly applicable for comparison with the present devices since the figure of merit deciding the pulse parameters in BHJ/EI devices are quite different.

The discontinuity in the structural phases in the BHJ/EI hybrid system translates as electrical discontinuities at the BHJ/EI interface in a suitable ω regime. The distribution of electrons/ions at the BHJ/EI interface produces a space charge layer (d_{SC}) in the semiconductor side in addition to the existing Helmholtz layer (d_H) and a diffuse charge layer (d_d) in the electrolyte side, giving rise to associated capacitances C_{SC} , C_H and C_d respectively⁵⁶. As shown in **Figure 2.27a** total capacitance, C_T can be expressed as a series sum of C_{SC} , C_H and C_d such that $1/C_T = 1/C_{SC} + 1/C_H + 1/C_d$, and C_T would hence be dominated by the lowest of C_{SC} , C_H and C_d . As C_H and C_d assume high values in low ω and zero bias regime, in general, C_T follows the trend of C_{SC} along the accumulation, depletion and the deep depletion regime⁵⁶. Upon photoexcitation of the interface, free charge carriers (electrons and holes) originate from the exciton dissociation at the BHJ interface. The resulting charge redistribution at the PEI thereby modifies the barrier potential at the interface, which is then reflected in the interfacial capacitance magnitudes.

In order to explain the crossover of the $\Delta C/C_{dark}$ upon photoexcitation at ω_c , the individual functional dependence of $C_{SC}(\omega)$ and $C_H(\omega)$ in the measurement range $10 \text{ KHz} < \omega < 1 \text{ MHz}$ were examined. The photogeneration of charge carriers in the semiconducting polymer film reduces d_{SC} , resulting in an increase in C_{SC} . At lower range $\omega (< \omega_c)$ where C_{SC} dominates the C_T trend, the increase in C_{SC} results in the increase in C_T upon photoexcitation and $\Delta C/C_{dark}$ is positive. The photoillumination of polymer/EI interface also generates a photopotential in a direction opposite to the existing field across the interface¹¹⁹. The decrease in the field across the Helmholtz

layer reduces the polarization of the adsorbed solvent molecules, leading to an increase in d_H and hence a decrease in C_H . At higher range ω ($> \omega_c$) where C_H dominates the C_T trend¹²⁰, the decrease in C_H upon photoexcitation therefore results in a decrease in C_T and $\Delta C/C_{\text{dark}}$ is negative. The transition from a positive to negative value of $\Delta C/C_{\text{dark}}$ at high ω can then be attributed to the change in the dominant contributing factor to C_T . The crossover from C_{SC} dominating behavior to that of C_H also surfaces in the $C(V)$ studies of pristine P3HT based polymer/EI devices where C_T follows the C_{SC} profile of a p-type semiconductor/EI interface at low ω . At high ω , C_T follows the profile of C_H . This phenomenon of crossover is depicted in the suggested **Figure 2.27b** which explains the trend of $C(V)$ observed in these device structures.

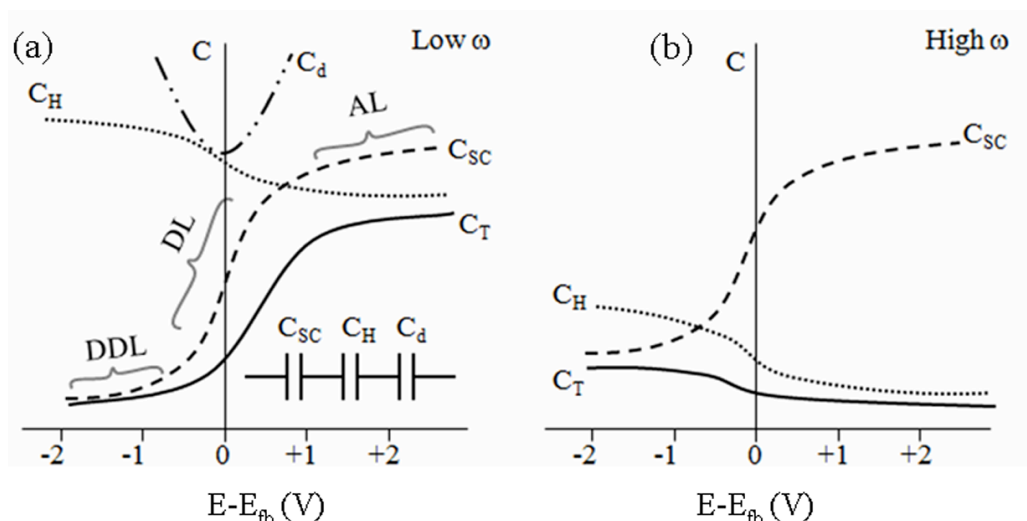


Figure 2.27 The behavior of space charge capacitances of a p-type semiconductor as a function of bias^{56,119}. C_{SC} is the space charge capacitance of the semiconductor, C_H is the Helmholtz layer capacitance, C_d is the capacitance of the diffuse layer of charges in the electrolyte and C_T is the total capacitance. E_{fb} is the flat band potential of the semiconductor and E is the applied bias. AL, DL and DDL represent the accumulation, depletion and deep depletion regimes of the space charge capacitance respectively. At low ω , C_T follows the profile of C_{SC} . (b) At much higher ω , C_H dominates the total capacitance¹²⁰ and therefore C_T would follow the profile of C_H .

2.5 Similarities to naturally occurring photoreceptors

The photosignals of BHJ/eq based photodetectors bear many interesting similarities to biological receptors. Polarity dependent color discrimination procedure has been previously demonstrated in biological systems completely different from that of the BHJ/EI: (i) In the purple membrane proteins, bacteriorhodopsin (bR) and its analogs,

there exists a photochemical cycle in response to light, which results in displacement currents. The λ -dependent direction of the displacement currents then determines the polarity of $I_{ph}(t)$ and $V_{ph}(t)$ across the oriented membranes^{121,122}. (ii) In photosynthetic membranes with chlorophyll, the polarity of $I_{ph}(t)$ in strong light absorbing regions and weak light absorbing regions is observed to be opposite¹²³. This polarity difference arises from the complex refractive indices of the various layers involved in the suspended membranes¹²⁴. In the present case, the responsivity of the BHJ/aq structures is at least an order of magnitude higher compared to these systems, along with a higher degree of control for the device parameters and more facile fabrication procedure.

More importantly, the time scales and magnitudes of the signals obtained from BHJ/EI structures are similar to those obtained from the electrochemical recording of bR monolayers as well as electrophysiological recording of an isolated mammalian retina. The detection frequencies (10 - 20 Hz) and detection thresholds ($\sim 5 \mu\text{W}/\text{cm}^2$) of BHJ/aq devices are also comparable to those in the primate vision systems at the receptor level and perception level respectively¹²⁵. The variation of $V_{ph}(t)$ and $I_{ph}(t)$ arising from the BHJ/EI devices as a function of intensity of the incident light is also similar to the dependence observed in visual processes of certain non-vertebrate and vertebrate photoreceptors¹²⁶⁻¹²⁸. These features point to the possibility of integrating these devices with visual systems and utilizing their optoelectronic properties for repairing dysfunctional visual processes.

Various advances have been made in the use of microphotodiode arrays^{90,93} and patterned stimulation electrodes^{96,97} for artificial retina devices designed to address vision related diseases arising from retinal dysfunction. However, known artificial retina devices involve conventional electronics that are based on inorganic materials such as carbon nanotubes, silicon or platinum/iridium oxide coated substrates^{90,96,97,129,130}. The advent of biocompatible photoactive optoelectronic polymers has an intrinsic advantage towards this application. The stimulation threshold levels involved within these neuronal layers are of the order of few mV, similar in magnitudes of those arising from the BHJ/aq structures. This means that a charge displacement within the polymeric bulk upon photoexcitation can induce ion redistribution at the electrolytic/neuronal membrane interface, thus leading to membrane depolarization with subsequent action potential generation in the neurons.

Indeed, the potentials arising from the conjugated polymer/electrolyte interface have been utilized for stimulation of hippocampal neurons cultured onto the polymer surfaces²⁸ and has recently been utilized for stimulating blind retinal tissues³¹. The studies related to the neuronal interfacing of the BHJ/EI structures to retinal neurons are presented in Chapter 3.

A combination of three semiconducting polymers tuned to different spectral range can *in vitro* perform the task of the natural photoreceptors, in the framework of the trichromatic theory of color vision, i.e., color detection by considering three types of cone photoreceptors: S, M and L with peak spectral sensitivities at around 430 nm, 530 nm and 560 nm respectively⁶⁰. The fuzzy logic nature of the single pixel response for color interpretation from our $I_{ph}(t)$ measurements can possibly be mapped to a combination of low-end photoreceptor process and higher end neural processes. In natural vision process, the signals arising from the S, M and L cones undergo complex processing at the ganglion cell level and this is understood on the basis of opponent-process theory of color recognition. This model explains the color vision at the perception level with its main postulate being that the visual system interprets color in an antagonistic way: red vs. green, blue vs. yellow and black vs. white^{60,75}. The photosignals from the BHJ/aq structures resemble certain outcomes from this antagonistic theory. For instance, the opposite polarity response from the red and green/blue can be equated to the antagonistic effect of the L/M cones. Further, the photosignals from BHJ/EI devices reveal higher sensitivity to blue color in a red background while a higher sensitivity to red color in a blue background (**Figure 2.17b**). Such effect of the background light persists for a finite duration corresponding to the space charge relaxation. The outcome of this effect is similar to the chromatic adaptation in the visual system, where prior exposure to red light results in higher sensitivity to green color and vice-versa¹³¹.

The modest frame rates and the wide color discrimination range of BHJ/aq devices may be adequate for certain sensor applications. While the pulse-profiling scheme may be unique for a color discrimination procedure with attributes such as identification of the spectral purity of a given source, it may have a limitation in resolving a color in situations with simultaneous colors and large intensity variation. It may however be possible to overcome this limitation with additional device-optimization and refined data/image processing algorithms.

2.6 Summary

The BHJ/EI device structures exhibit interesting set of properties that could be utilized for intelligent sensing and biomimicking visual photoresponse. The origin of the unique features across BHJ/EI device structures could be analyzed by varying various parameters in the $I_{ph}(t)$ and $\Delta C/C_{dark}(\omega)$ measurements. These measurements provide an insight into the photoinduced transport mechanisms of BHJ/EI structures. The device response features could be modeled using various microscopic parameters. The λ -dependent polarity variation and temporal characteristics of the photoresponse of BHJ/EI devices could be used for multicolor sensing and demonstrates that a single active BHJ layer of appropriate thickness in contact with an aqueous medium acts as a color discriminator device. The device features resemble various properties of the photoresponse of natural photoreceptor systems including those in the retina. The stability of the BHJ response in contact with aqueous media as well as the interesting similarities of photoresponse of such structures with that of the natural vision systems demonstrate that organic electronics and optoelectronics offer credible alternatives to materials utilized in artificial retina solutions and have the prospect of seamless integration of these devices with neural systems. The work described in the next chapter is towards this direction, and presents the utilization of these device structures for evoking visual signals in a blind retina.

Chapter 3

Optoelectronic Polymer Structures for Artificial Retina Applications

The development of bioelectronic retinal implants is aimed towards eliciting visual perception in the retina by electrically stimulating the retina either subretinally from the pigment epithelial side or epiretinally from the RGC side. Inorganic materials like silicon have been proposed and explored as photoactive layers for retinal prosthesis, and silicon photodiodes have been recently utilized in an infrared photovoltaic sub-retinal implant design. Conjugated polymers as alternative semiconducting materials have a unique combination of mechanical and optoelectronic attributes, which can be utilized for advanced bioelectronic and neuroprosthetic interfaces. Recent reports have utilized the optoelectronic properties of these materials as active triggers for neuronal stimulation and visual systems.

The resemblance of the optoelectronic features of the BHJ/EI structures to various photoreceptors suggests the possibility of integrating these structures with a blind retina and evoking visual signals in the nervous tissue. In the work described in this chapter of the thesis, BHJ/EI structures were interfaced with an embryonic stage chick retina in the early stage of development where photoreceptors are not functional. The optical stimulation of BHJ layers coated on a MEA resulted in eliciting action potentials in RGCs. The optoelectronic polymer interface presented here could provide visual cues to a blind retina and therefore can be used as a viable platform for future retinal implants.

Degenerate (rd1) mouse retinas were initially used as the model for blind retina and patch clamp recordings from the RGCs were used to characterize the retinal response. In brief, loose-patch current-clamp recordings were made on RGCs with patch electrodes of resistances 5.0–8.0 M Ω using Axopatch 200B amplifier (molecular devices). Electrodes were prepared using micropipette puller (Sutter Instruments) and were filled with AMES' medium adjusted to pH 7.4. Data were low-pass filtered at 10

kHz at the amplifier output and digitized at 50 kHz on a computer running pClamp 10 (Molecular Devices) connected to a Digidata 1440A data acquisition system (Molecular Devices). The preliminary results of these studies suggested successful stimulation of the retina with BHJ/EI structures (**Figure 3.1**). However, such studies with retinal degeneration models like rd1 in mouse, or light-induced photoreceptor degeneration in rats utilized elsewhere³¹ suffer from the issue of residual cone photoreceptors in the outer retina. It therefore becomes difficult to distinguish between the light-induced RGC response originating from the polymer layer and that originating from the residual photoreceptors.

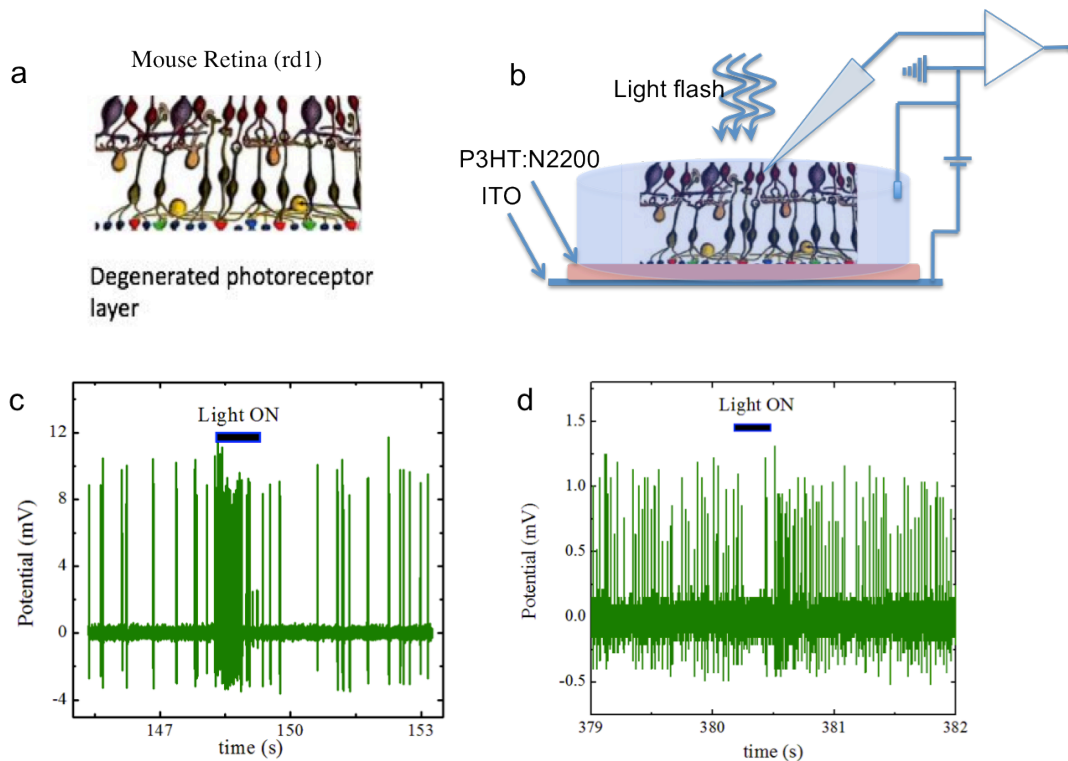


Figure 3.1 (a) Schematic showing a degenerate retina from rd1 mouse. (b) Schematic of the experimental set-up. The ITO/BHJ glass were subretinally interfaced with the retina and RGC responses were recorded using the patch clamp apparatus. (c) Increased RGC activity upon photoexcitation of the underlying BHJ layer (d) Inhibited RGC activity upon photoexcitation of the BHJ layer recorded from another cell. The spikes in (c) and (d) represent individual action potentials from the cell, measured by extracellular single unit recordings in loose patch configuration.

The embryonic-stage model of blind retina, where photoreceptors are non-functional, is advantageous over the degenerate retina model. This model gives a control over the

sensitivity of retina to light and can be used to circumvent the issue of remnant photoreceptors in the degenerate models. In this regard, the chick retina has been well studied for developmental embryonic stages and it is shown that at embryonic day 12-15, the photoreceptors are not functional, while the other retinal circuitry is developed. The embryonic stage chick retina therefore serves as a suitable platform to study the RGC response from artificial receptors like the BHJ layer. In the studies presented here, the BHJ layers were coated on a MEA and interfaced directly with the RGC layer of the chick retina. This approach allows for simultaneous stimulation and recording from the retina. Our results demonstrate that the photoexcitation of the BHJ interface with the blind retina in physiological conditions results in a neuronal response in the retina, highlighting the efficacy of polymer semiconductors as artificial receptors for interfacing with the visual systems. The features of the elicited neuronal response (latency, spike rate and spike number) were observed to depend on the incident light parameters like intensity, pulse width and rate, spatial profile, and wavelength, which control the optoelectronic response of the polymer film. Interestingly, the evoked activity resembles the natural response of the retina to light stimulation. The following sections describe the experimental methods and results in detail.

3.1 Details of device fabrication, retina preparation and recording methods

3.1.1 Polymer coating and characterization

The BHJ blend constituted P3HT (Luminescence Technology Corp., China) as the donor and N2200 (Polyera Corp., USA) as the acceptor. The donor and acceptor polymers were mixed in 4:1 by weight, respectively and dissolved in chlorobenzene (Sigma) at a concentration of 10 mg/ml. The BHJ solution was spin cast on the pre-cleaned MEA, which consisted of TiN electrodes of 30 μm diameter at an inter-electrode distance of 200 μm , at a spin coating speed of 800 rpm. The BHJ-coated MEAs were annealed at 110 $^{\circ}\text{C}$ for 15 min in air under dark conditions. This protocol resulted in a film thickness of ~ 400 nm, measured using Dektak stylus profilometer.

The $V_{\text{ph}}(t)$ for the BHJ films were measured on a BHJ-coated MEA, with TiN electrodes of diameter 10 μm . The BHJ-coated MEA was placed in contact with 1X PBS (phosphate buffer saline) and $V_{\text{ph}}(t)$ were measured across a TiN electrode and an Ag/AgCl

reference electrode in PBS using a 60-channel voltage amplifier (Multichannel systems, Germany). The photoillumination was achieved using a blue diode laser ($\lambda = 405 \text{ nm}$) whose intensities were controlled using optical filters.

3.1.2 Retina Preparation

Fertilized chick eggs were incubated at 37°C in an incubator. The chick eggs were utilized for retina isolation after 12-14 days of incubation (E12-E14). During this embryonic stage, the photoreceptor layer of the chick retina is not functionally developed. The eggs were broken, chick was decapitated, the eyes were enucleated, and hemisected, the lens and vitreous were removed from the eyecup and retina was isolated from the sclera. The dissection and retina preparation was carried out in freshly prepared artificial cerebrospinal fluid (ACSF), which constituted 124 mM NaCl, 25 mM NaHCO₃, 1.2 mM HEPES, 5 mM KCl, 1.2 mM MgSO₄, 2.5 mM CaCl₂ and 10 mM glucose at pH 7.4. Isolated retinas were then held with a supporting filter paper (Millipore 0.4 μm) on the photoreceptor-side and placed flat on the uncoated or polymer-coated MEAs with RGC side facing the electrodes. The MEA-retina system was continuously perfused with ACSF at a rate of 5 ml/min and was maintained at 32 °C throughout the experiment. The system was left to stabilize for at least 2 hours before starting the recording.

3.1.3 Multi-unit (extracellular) recordings from retina

MEAs from Multichannel Systems, Germany were used for signal recordings from the tissue. The MEAs consisted of 60 titanium nitride (TiN) electrodes on glass, 30 μm in diameter at an inter-electrode distance of 200 μm in an 8X8 square arrangement. TiN is a chemically stable metallic conductor with good biocompatibility. These electrodes are fabricated with a high surface roughness so as to have large charge-injection capacities. The electrodes were robust and checked for any artifacts before starting the retina experiments. Uncoated MEAs were used for control experiments; while BHJ-coated MEAs were used for recording RGC signals from the BHJ/retina interface. Extracellular recordings were obtained simultaneously from all 60 electrodes, which were amplified with a 60-channel amplifier (Multichannel systems, Germany). The data from the channels was digitized using a commercial multiplexed data acquisition system

(MC_Rack and MC_Card, MultiChannel Systems, Germany) at a sampling rate of 20 kHz and was stored as .mcd files for further analysis. The data acquisition was triggered with the stimulus generator and was typically recorded from 200 ms pre-stimulus and 4200 ms in total. Same stimulus generator was used to trigger the photoexcitation sources and the time stamps of trigger were recorded in one of the analog channels of the MC_Card. During experiments of retinal stimulation, Butterworth 2nd order, band-pass (1 Hz – 500 Hz) filter was turned on through the MC_Rack to suppress the enveloping $V_{ph}(t)$ from the BHJ layer.

3.1.4 Optical Stimulation of the BHJ/retina

Blue and white LEDs (Thorlabs Inc.) were used for optical excitation of the system through the upright microscope objective lens assembly. A whole-field or local spot illumination was achieved by choosing a low or high magnification objective lens respectively. The intensity, frequency and pulse duration of the LEDs were controlled using the stimulus generator (Multichannel systems, Germany), programmed through the MC_stimulus software (Multichannel systems, Germany). The wavelength and intensities were controlled using various color and neutral density filters inserted in the optical path of the light beam. A schematic of the experimental set-up is shown in **Figure 3.2**.

3.2 Results of control experiments and retina stimulation with BHJ

Certain background experiments were carried out before recording the retinal response to BHJ photoexcitation. These experiments establish the possibility of coating a BHJ layer onto an MEA, which neither affects the capability of the MEAs to record retinal activity, nor interferes with the retinal spontaneous activity. The control experiments involved the recording of retinal activity upon illumination with light on uncoated MEAs and established the optical inactivity of retina tissues in the E12-E15 stage. The retina was then interfaced with the BHJ-coated MEA for simultaneous stimulation and recording.

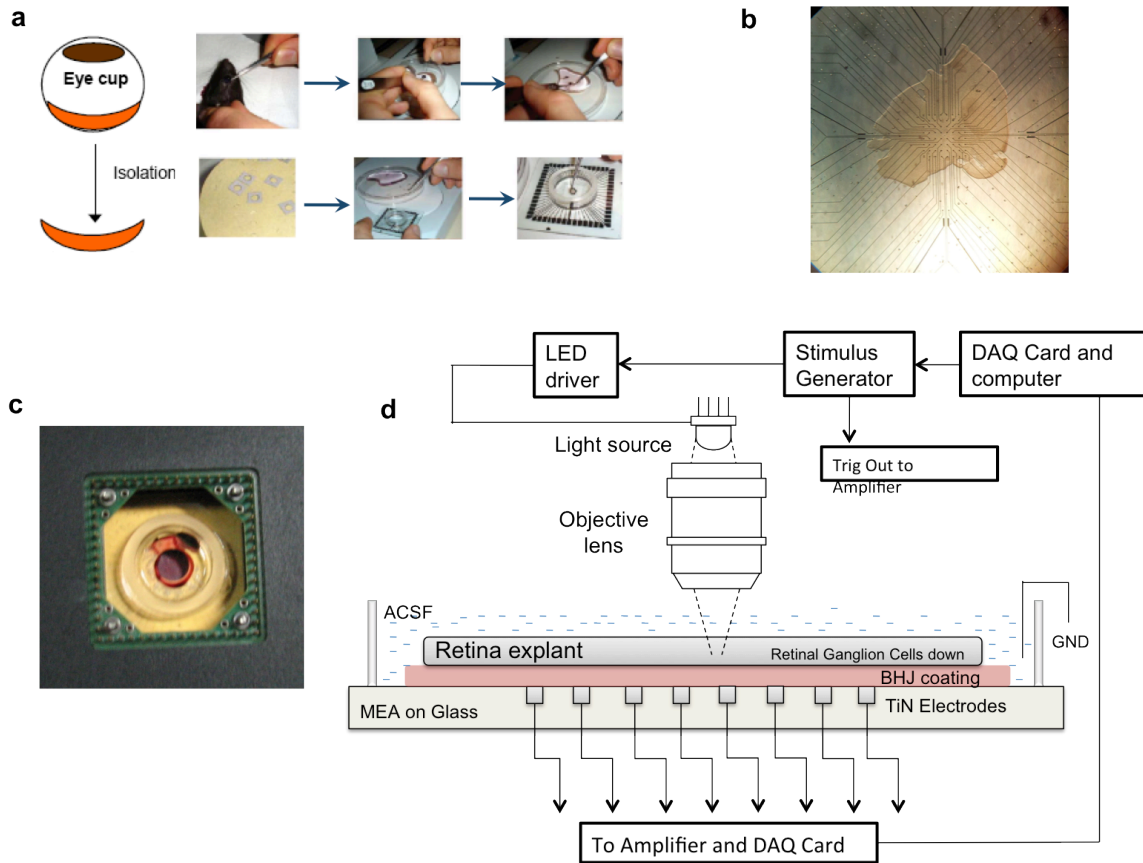


Figure 3.2 (a) Schematic of the steps involved in retina isolation from an animal (b) Snapshot of a retinal explant on a MEA (c) Snapshot of BHJ coating on a MEA placed in the amplifier (d) Schematic of the experimental set-up used for interfacing BHJ-coated MEA with the retina explant from a chick eye.

3.2.1 Background and control experiments

The following systems were studied before interfacing retina with the BHJ layer:

(i) MEA/buffer/light-pulse: The photoexcitation of the uncoated MEAs in buffer medium without the BHJ coating or the retina does not result in any stimulus artifact or electrical response from the TiN electrodes of the MEA (**Figure 3.4a**).

(ii) MEA/BHJ/buffer/light-pulse: The photoexcitation of BHJ-coated MEAs in buffer medium without the retina results in the optoelectronic response from the BHJ layer. This response is in the form of a slowly rising (during light on) and descending (during light off) photovoltage, $V_{ph}(t)$ (**Figure 3.3**). During the MEA recordings with the retina, the V_{ph} profile is suppressed using circuit filters and it appears as transients (**Figure 3.4a**).

(iii) MEA/retina or MEA/BHJ/retina: The developing chick retina on coated and uncoated

MEAs (without photoexcitation) exhibits spontaneous wave-like activity (**Figure 3.4b**). The spontaneous activity does not get altered upon introducing the polymer layer between the MEA and the retina, showing that the BHJ layers do not interfere with the retinal activity (**Figure 3.4c**). Further, the average S/N of the spontaneous activity recorded with coated and uncoated MEAs was observed to be 8.6 ± 1.1 and 10.3 ± 0.6 , respectively (**Figure 3.4d**). The retention of similar S/N magnitudes upon BHJ coating confirmed that the BHJ does not affect the capacity of the MEAs to record the retinal activity.

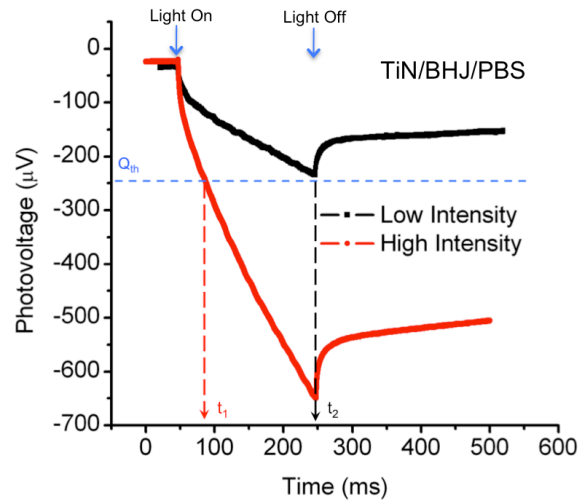


Figure 3.3 Photovoltage, $V_{ph}(t)$ profiles from a 10 μm diameter TiN electrode at $\sim 500 \mu\text{W}/\text{mm}^2$, and $1000 \mu\text{W}/\text{mm}^2$ of incident light with $\lambda=405 \text{ nm}$. Q_{th} and t represent the assumed threshold charge density required for eliciting neuronal activity and corresponding expected latency of the neuronal response, respectively.

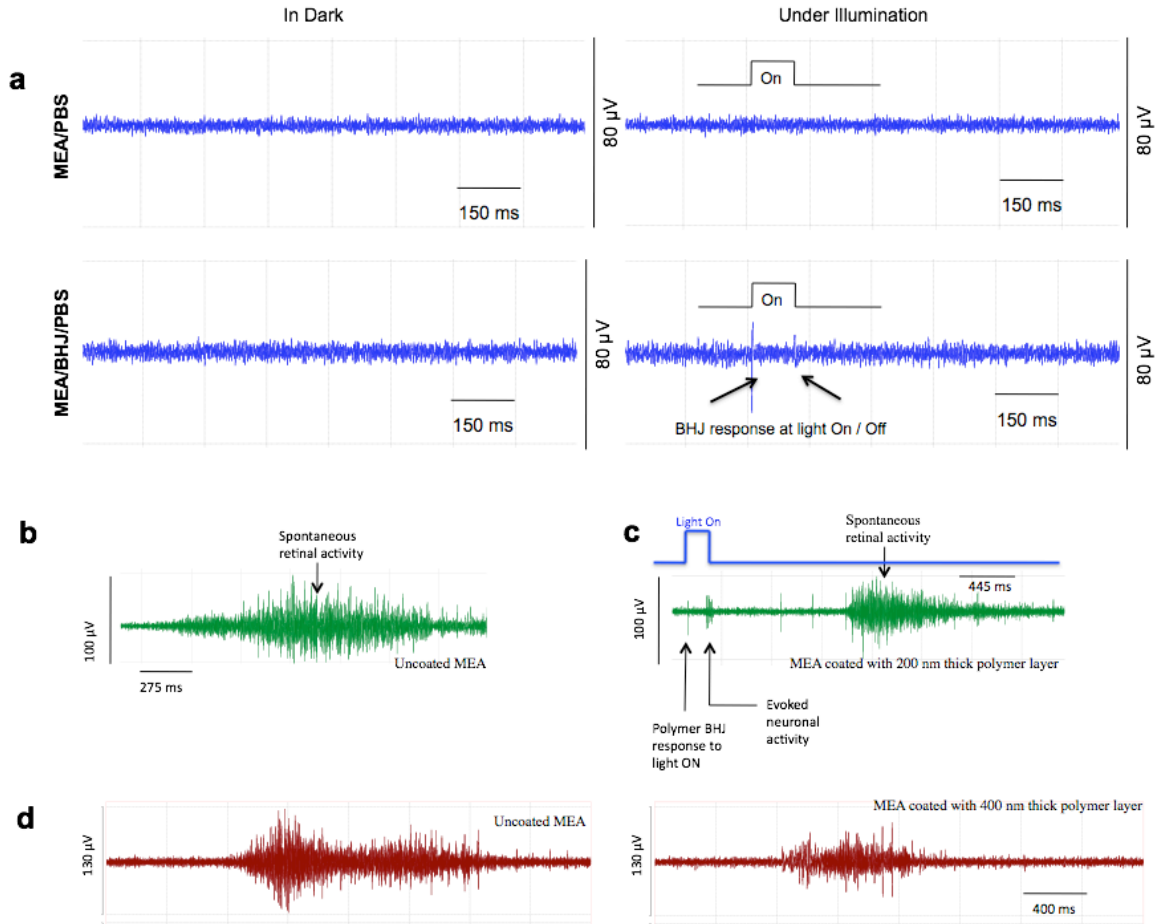


Figure 3.4 Background experiments (a) MEA recordings without the retina, for uncoated and BHJ-coated MEA electrodes. Illumination data shown for a 100 ms light pulse of $\lambda=410$ nm at $200 \mu\text{W}/\text{mm}^2$. Upon photostimulation, there is no artifact on the uncoated MEA, while for the BHJ-coated MEA, the BHJ response appears as a transient signal at the instants of light On and Off. (b) Spontaneous wave-like activity recorded on an uncoated $30 \mu\text{m}$ TiN electrode of the MEA. (c) Light-induced neuronal activity from a retina on a BHJ-coated electrode, along with a spontaneous retinal wave. The existence of the spontaneous wave confirms that the retina in contact with the BHJ retains its natural activity. Data shown for light pulse of $\lambda=410$ nm at $500 \mu\text{W}/\text{mm}^2$ (d) S/N comparison of an uncoated and BHJ-coated TiN electrode. The average S/N ratio of the spontaneous retinal activity on the BHJ-coated and uncoated MEAs is 8.6 ± 1.1 and 10.3 ± 0.6 respectively.

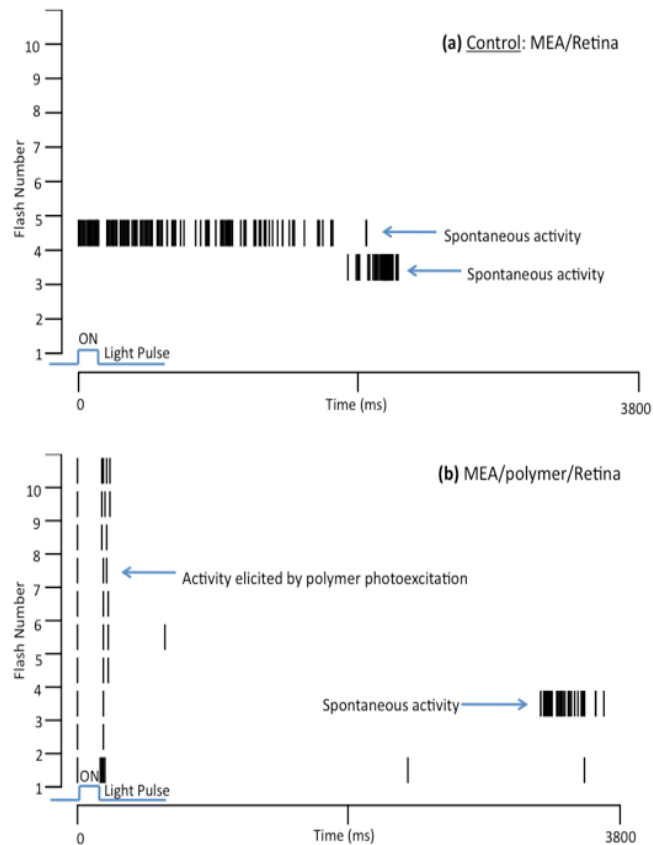


Figure 3.5 Control experiment. A representative raster plot data showing the results of the control experiment compared with the BHJ/retina experiment. (a) Successive photoexcitation of the retina on uncoated MEA does not elicit any additional neuronal activity. Only spontaneous activity exists in the experiments without the BHJ. (b) Photoexcitation of the retina on BHJ-coated MEA elicits a neuronal activity. The elicited neuronal response is consistent with successive flashes. The spontaneous activity of the retina is independent of the elicited retinal response. Each flash of light represents a 100 ms wide pulse of $\lambda=410$ nm at $500 \mu\text{W}/\text{mm}^2$, time interval between successive flashes is 10 s.

The control experiments involved recording the activity of the early stage chick retina placed on uncoated MEAs, upon photoillumination. These experiments were essential to confirm the optical inactivity of the retina. The photoillumination of the chick retina on uncoated MEAs does not elicit a neuronal response and consists of only the spontaneous activity (**Figure 3.5**). This absence of evoked neuronal signals was noted on the entire MEA, across > 15 different retina explants, to multiple wavelengths of

incident light. The presence of spontaneous retinal waves and the spike activity therein implies that the retina is adhering well to the MEA, and the absence of spikes upon photoillumination is solely due to the optical inactivity of the retina. These experiments confirmed the optical inactivity of the chick retina both from photoreceptors and from intrinsically photosensitive RGCs, which have a peak sensitivity between 476 nm - 484 nm). The retina was then interfaced with the BHJ-coated MEAs.

3.2.2 Typical response of retina to BHJ photostimulation

A typical recording snapshot from a MEA/BHJ/retina system to whole-field photoexcitation is shown in **Figure 3.6**. The retinal response in form of spikes to the photoexcitation of the BHJ layer can be seen on multiple electrodes of the MEA. A magnified time window from one of the electrodes is shown in **Figure 3.7**. Upon photostimulation of the MEA/BHJ/retina system, the photovoltage spikes from the BHJ layer are accompanied by the neuronal spikes from the retina, which appears after a certain response latency. Such retinal activity could be elicited using multiple wavelengths of the light pulse across visible spectrum (**Figure 3.8**). The neuronal signals could also be elicited under constant white background illumination (**Figure 3.9**).

The retinal response to light was observed on random but few electrodes (~ 10%) of the MEA for each set of experiment. These observations indicate that improved processing conditions that ensure intimate contact of BHJ films with the MEA could result in a neuronal response from a higher fraction of electrodes. The neuronal signals from the working electrodes were robust and persisted over a long period of time (>14 hours).

The origin of the neuronal response was traced to the semiconducting polymer by varying the incident light parameters such as intensity, duration, repetition rate and color, as described in the following sections.

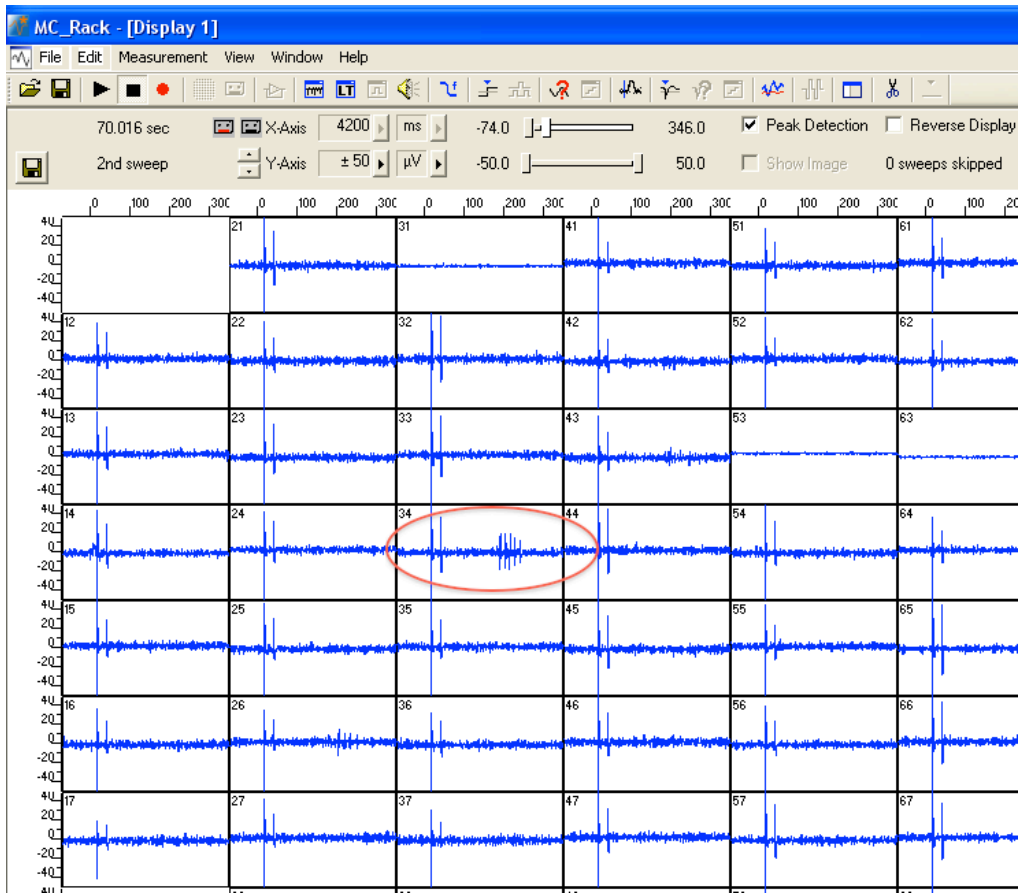


Figure 3.6 A recording snapshot of the BHJ-coated MEA system with the retina. Upon stimulation with a 50 ms wide light pulse, the BHJ response in form of initial transient spikes followed by retinal activity can be seen on many electrodes, for example, electrode #34.

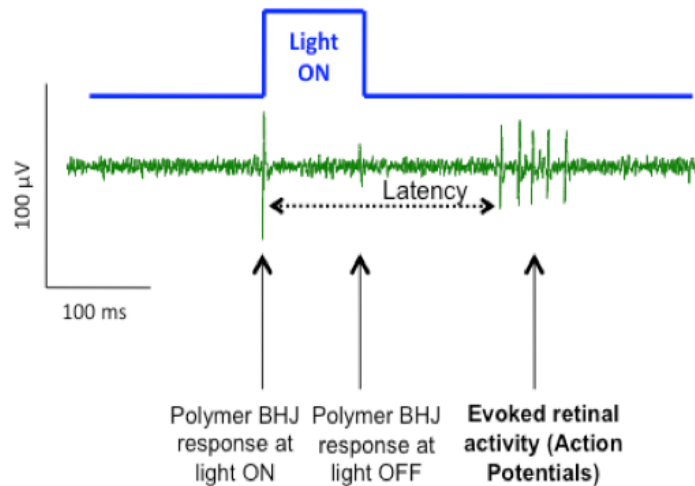


Figure 3.7 Typical neuronal response elicited in the retina upon polymer photoexcitation. The BHJ transient photovoltage signals are followed by the neuronal spikes. A magnified time window shown for $\lambda=410$ nm, at $400 \mu\text{W}/\text{mm}^2$, 200 ms pulse duration.

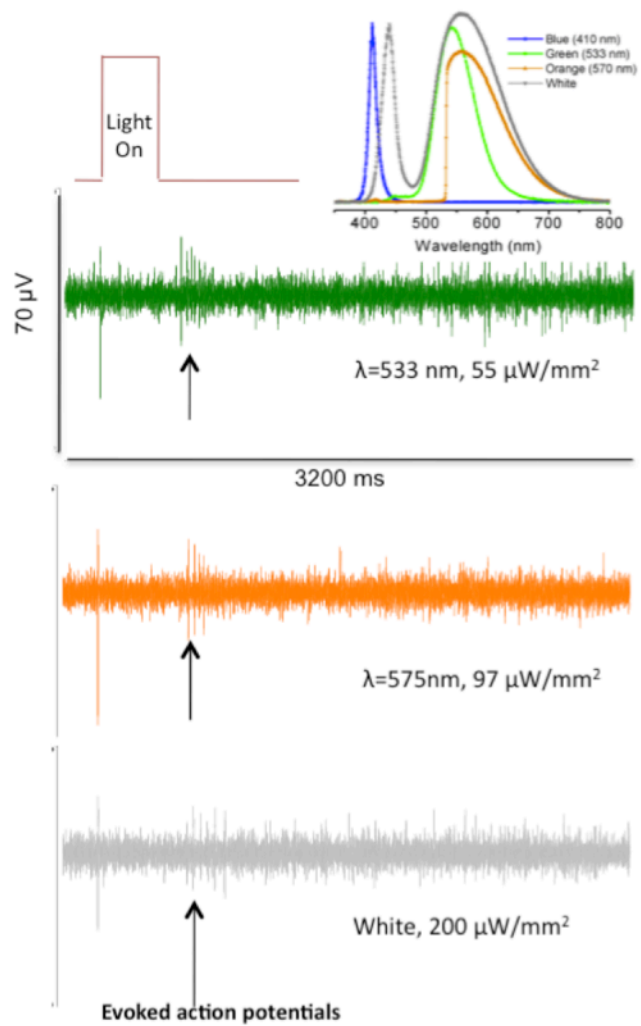


Figure 3.8 Neuronal responses to photoexcitation of the BHJ layer with green, orange and white incident light pulses. Inset shows the wavelength spectra of the incident colors.

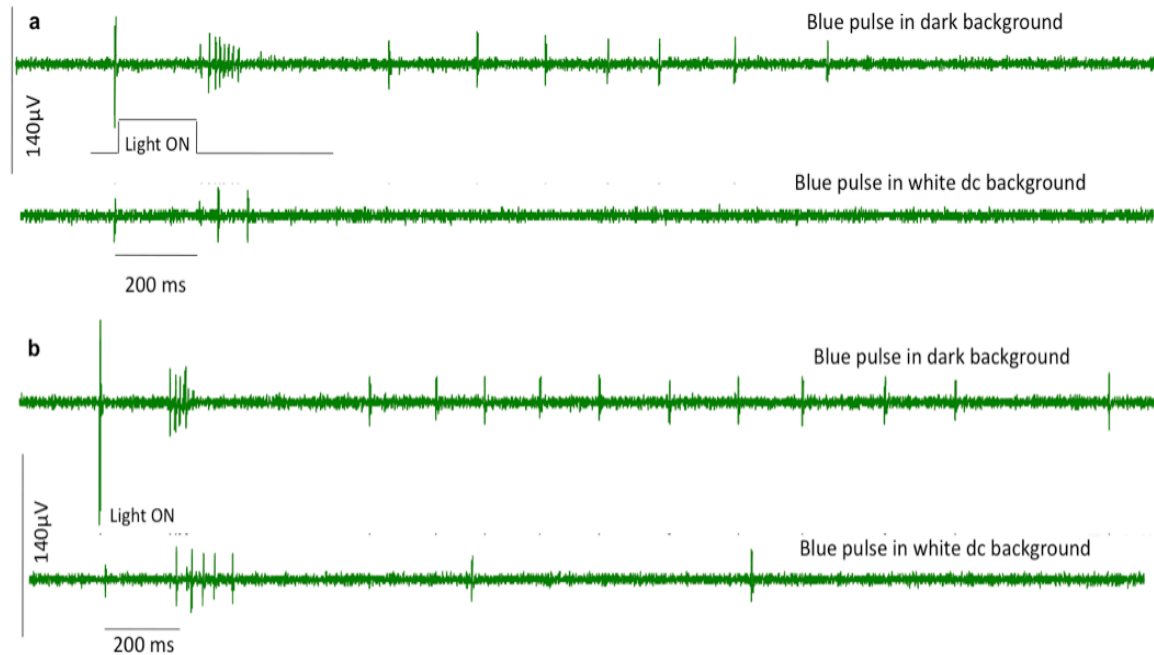


Figure 3.9 Elicited neuronal activity upon photoexcitation of the BHJ layer with a blue light pulse ($\lambda=410$ nm), under dark and white dc background (~ 200 lux) at a pulse intensity of (a) $150 \mu\text{W}/\text{mm}^2$ (b) $500 \mu\text{W}/\text{mm}^2$.

3.2.3 Intensity and duration dependence of the response

The response latency, the total number of spikes and the spike rate was observed to depend on light intensity (

Figure 3.10). With increasing intensity, the average response latency decreased from 500 to 150 ms (**Figure 3.10a,c**), with latency taking an inverse power law w.r.t intensity; Γ with $\gamma \sim 0.33$ accompanied by an increase in the number of spikes (**Figure 3.10d**). It was noted that this variation of latency can also be fitted to a $-\log(I + \text{constant})$ behavior. Beyond intensities greater than $300 \mu\text{W}/\text{mm}^2$, the average latency period gradually plateaus at ~ 150 ms. Further, at high intensities, the elicited neuronal response consists of two distinct sets of spikes: a primary response with a latency of ~ 150 ms, followed by another set of sustained, longer latency (~ 500 ms) spikes with a lower firing rate. The peristimulus time histograms (PSTH) of the action potentials (**Figure 3.10b**) demonstrate that with increasing light intensities, the total number and the rate of occurrence of the spikes increases and the spike rate follows a more uniform distribution. The duration (or

width) of the light pulse was also observed to affect the average number of spikes and the response latency (**Figure 3.11**). With increasing pulse width, the spike rate increased while the response latency decreased.

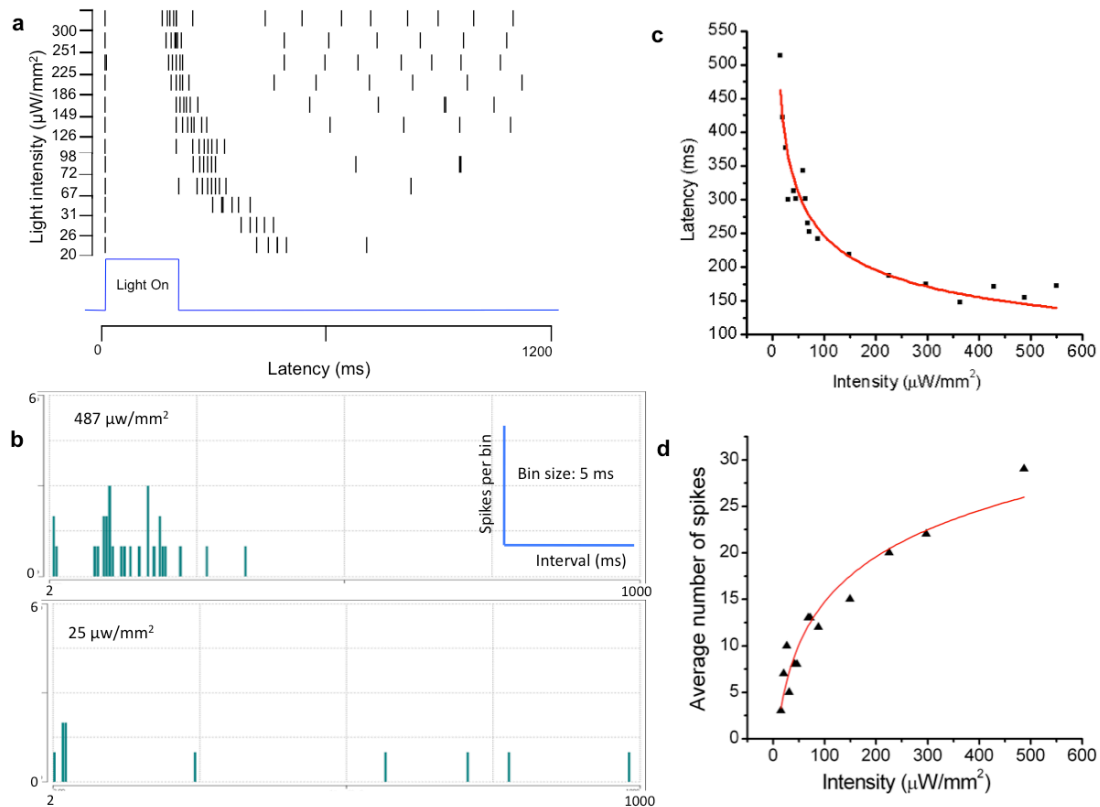


Figure 3.10 (a) A raster plot of elicited action potentials with increasing light intensities. Each marker corresponding to a specific intensity represents an action potential. (b) PSTH of the elicited activity for 2 intensities, showing increased number of spikes and rate of occurrence at higher intensity. (c) The average response latency as a function of light pulse intensity; solid line represents the power-law fit. (d) The average number of evoked spikes as a function of light pulse intensity. All data was recorded with $\lambda=410$ nm illumination, pulse duration 200 ms.

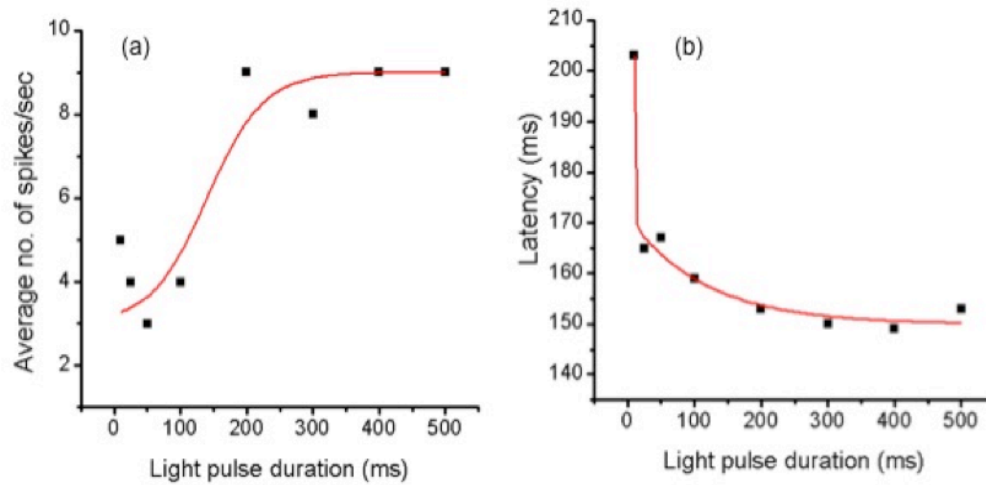


Figure 3.11. Dependence of evoked activity on duration of light pulse. (a) Average number of spikes per second (b) Average latency of the neuronal activity. Data shown for blue light pulse at $500 \mu\text{W}/\text{mm}^2$.

3.2.4 Temporal resolution

In order to estimate the minimum time interval between successive light flashes required to elicit a neuronal activity, the time interval t between subsequent light pulses was varied and the onset of action potentials was monitored. It was observed that the number of evoked spikes reduced with decreasing t (**Figure 3.12**). This variation of the activity with repetition rate depends on the pulse intensity. At low intensities ($100 \mu\text{W}/\text{mm}^2$), a temporal resolution of ~ 1 s could be achieved, while at a higher intensity the temporal resolution was in the range of ~ 5 s.

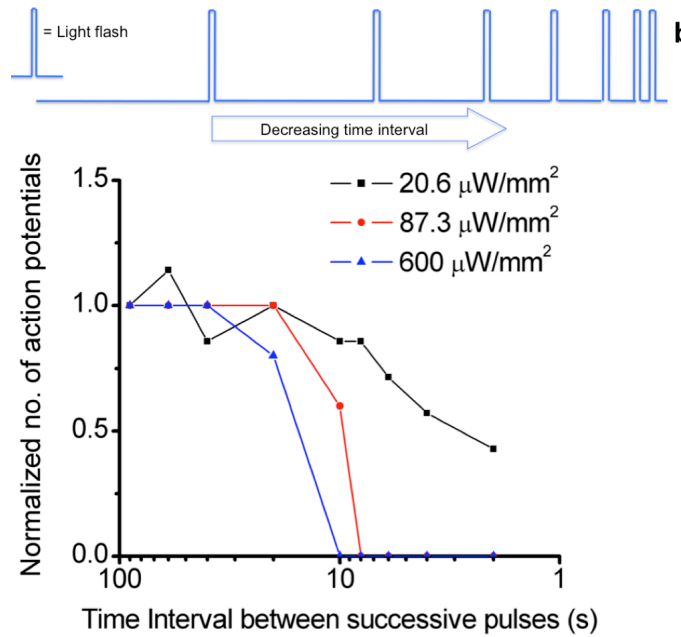


Figure 3.12 The number of action potentials as a function of time interval between successive light flashes. Light flashes of 200 ms duration, $\lambda=410$ nm, whole field illumination. Y-axis is normalized by the number of action potentials on the first flash for a specific intensity.

3.2.5 Spatial stimulation

The spatial locations of the BHJ/retina interface around the response sites could be accessed and stimulated by localizing the illumination spot to a diameter of $\sim 200 \mu\text{m}$. The spot diameter and location could be controlled by manipulating the objective lens magnification and its position, respectively. These measurements were done at intensities just above the response-threshold to minimize light scattering and cross-talk between neighboring electrodes. The neuronal activity on a responding site could be stimulated by illuminating regions at sizable distances ($> 500 \mu\text{m}$) away from the signal-acquiring electrode, with latencies ranging between 150 and 700 ms. This region was observed to be anisotropic (**Figure 3.13**).

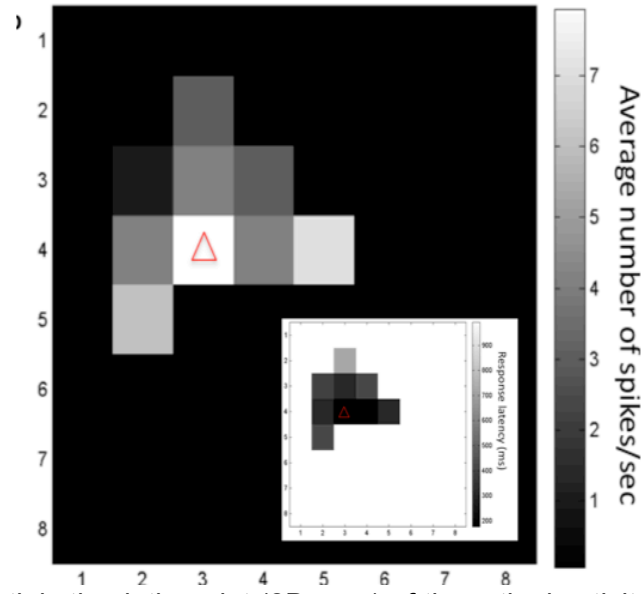


Figure 3.13 Spatial stimulation plot (2D map) of the retinal activity at a MEA electrode (# 43, marked with an open triangle). The map shows the average number of spikes/sec elicited. Inset- Response latency of the activity at the same electrode upon local photoexcitation of the BHJ layer on other MEA electrodes.

3.3 Origin of the features of retinal response to BHJ photoexcitation

An embryonic chick retina in the early stage of development where photoreceptors are not functional provides a suitable platform to prove the utility of photoactive BHJ layer for retinal stimulation. The choice of a developing chick retina with dysfunctional photoreceptors over the conventional models of retinal degeneration circumvents the issue of distinguishing the elicited neuronal response from the natural response due to remnant photoreceptors in the latter. Further, the neuronal signals arising from optical as well as electrical stimulation from developed chick retina have been well documented and can be used to compare the response invoked from the artificial receptors.

The presynaptic activation of RGCs through stimulation of inner retinal layers by optical or electrical stimulation in the *developed* chick system results in characteristic spike patterns (**Figure 3.14**). For instance, a significant population of RGCs has been shown to exhibit a dual peak response to photoillumination, where the response consists of a primary burst of spikes occurring within a short period after the stimulus, and a secondary group of spikes with a low firing rate after a certain interval¹³². Subretinal

electrical stimulation of the chick retina has been shown to exhibit similar response profiles⁹¹. The origin of neuronal signals from the RGCs in both cases is interpreted to be the subretinal signaling in the inner retinal pathways between the bipolars and RGCs, or the horizontal/amacrine cells and the RGCs.

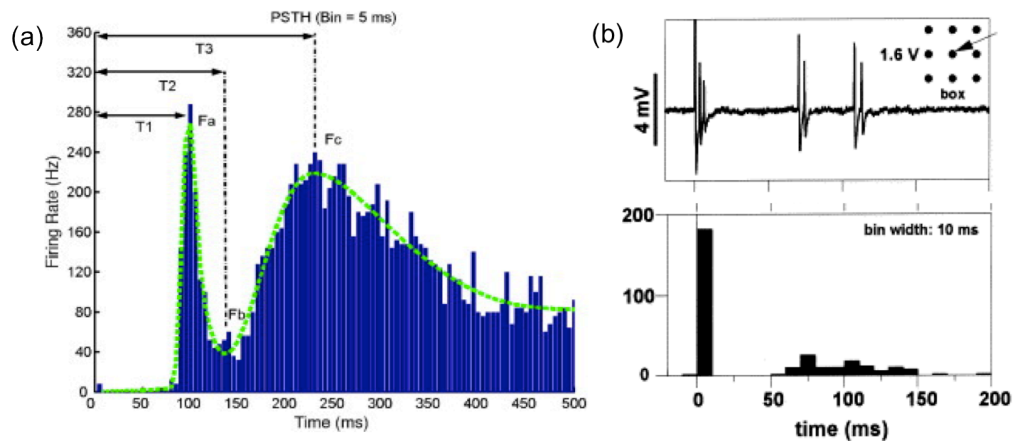


Figure 3.14 (a) Retinal ganglion cells' dual-peak response to optical stimulation from a chick retina seen in a PSTH plot. Light stimulus was given at 0 ms. Used with permission from ¹³². (b) Responses of chick retina's ganglion cells evoked by single voltage pulses of pulse duration 0.5 ms - analog trace and PSTH. Spike response pattern consisting of initial response followed by a transient inhibition and a delayed response. Used with permission from ⁹¹.

Epiretinal stimulation of retinas with pulsed current or voltage profiles are known to stimulate the RGC axons and the overall response of the RGCs is different than that observed upon subretinal stimulation¹³³. In case of the direct epiretinal RGC stimulation, the response appear withing very short latencies (0.1-5 ms) and with a temporal resolution of 2- 20 ms ^{133,134}. It has also been shown that when the input stimulating pulse is changed from a rectangular profile to non-rectangular electrical pulse profiles, the neuronal response in the RGCs arises from a non-axonal stimulation and results in a longer latency response of the RGCs ^{135,136}. The longer latency is attributed to the presynaptic stimulation of the inner retinal layers.

The response of the light insensitive chick retina to the optical stimulation of the

epiretinal BHJ interface exhibit a set of primary and secondary neuronal response and is similar to the response of the chick retina to optical and subretinal electrical stimulation. The origin of this similarity is intriguing and can be associated with the unique voltage profile, which results with a sub-retina like stimulation. The power law behavior of latency with respect to intensity of visual stimuli is also similar to some previous reports¹³⁵. The subretinal activation and long latency response of the elicited retinal activity in response to the non-pulsatile $V_{ph}(t)$ stimulation from the epiretinal side are similar to those observed recently upon stimulating the retina with a multi-capacitor array¹³⁷. These results establish that the unique pulse profiles at the capacitive interface of the polymer and the retina result in selective activation of the inner retinal layers and have implications of a better control of neuronal activation over conventional pulsed profiles. The anisotropic neuronal response with long response latencies, originating from a stimulation location across a considerable range of distances also point to stimulation of inner retinal layers.

The origin of the measured neuronal response latencies and temporal resolution in relation to the intensity and duration of the light pulse can be traced to the temporal characteristics of the photosignals from the BHJ/EI interface. The charge density (Q) at the BHJ/electrolyte interface upon photoexcitation is manifested in the $V_{ph}(t)$. A suitable magnitude of charge density at the interface and charge density gradient in the epiretinal environment can be translated to a potential difference over the cell membrane of inner retinal cells and RGCs, causing the latter to fire. The stimulation of retina with μm -sized silicon photodiodes in other optoelectronic retinal prosthesis approaches usually requires an additional power source for reaching the threshold stimulus levels with ambient light intensities, since current generated by a single microphotodiode is not sufficient^{95,138,139}. This is usually because of the distance between the electrodes and the retinal cells. For instance, the implant is separated by inner limiting membrane and nerve fiber layer in case of the epiretinal approach, and with subretinal scar tissue in the case of sub-retinal implantation. In addition, diseased retina has uneven thickness and the electrode array may not lie flat on the tissue, leading to further separation of cells from electrodes. Large distances between the cells and electrodes also result in cross-talk between neighboring electrodes, and results in a requirement of high charge density for cell stimulation. Furthermore, variability in the distance between electrodes and cells in

different parts of the implant also results in strong variations of the stimulation threshold, making it necessary to adjust the signal intensity in each pixel. The utilization of BHJ/EI interface for retinal stimulation overcomes these issues and the structures are able to stimulate the retina without any external power sources. This points to the importance of better mechanical conformity of these soft structures, as well as to the similarity between the pulse-profile characteristics of BHJ-polymer/electrolyte structures with those of natural receptors.

3.4 Summary

A BHJ polymer structure is utilized as an active photosensitive platform to stimulate an embryonic-stage blind chick retina. The photoelectric signals initiated by the BHJ layer evoke neuronal activity, whose features resemble the natural response of the retina to light stimulation. Unlike conventional epi- and sub-retinal approaches using inorganic elements and metal electrodes in contact with the tissue components, the approach presented in this work utilizes a simple, wiring free epiretinal interface. The evoked retinal response was studied as a function of the light intensity, color, light pulse-width and repetition rate, which correlates directly to the properties of BHJ/EI structures. The photosignals generated at the BHJ/EI interface can be additionally tuned by varying the thickness and composition of the active layer as discussed in the previous chapter. The possibility of patterning the BHJ layer on flexible and conformable substrates having an array of transparent electrodes could result in utilization of this polymer interface as an optoelectronic epiretinal interface for artificial retina applications. The aspects of biocompatibility and cytotoxicity of these polymer layers, along with the specific interaction between the BHJ layers and the retinal cells in culture are discussed in the next chapter.

Chapter 4

Optoelectronic Polymer Structures as Active Biocompatible Interfaces for Neuronal Networks

4.1 Introduction

Innovation of novel materials and device designs for biomedical research involves the development of stable and biocompatible biointerfaces. Interfacing a material with a tissue or organ *in vivo* results in a complex interaction of cells and tissues with the material which can evoke the release of mediators such as chemotactic and growth factors that elicit and sustain inflammatory responses at the implant site ¹⁴⁰. New generation of biomaterials and biointerfaces are being developed with suitable features that ensures better biocompatibility: surface modification to overcome nonspecific protein adsorption *in vivo*, precision immobilization of signaling groups on surfaces, development of synthetic materials with controlled properties for drug and cell carriers, and design of sophisticated three-dimensional architectures to produce well-defined patterns for diagnostics and tissue engineering ¹⁴¹. Although electrochemically active conducting polymers like PEDOT:PSS have been utilized for developing neuronal probes and biosensors and have been shown to be biocompatible, the prospect of using semiconducting polymers for biosensing or interfacing with neuronal systems like retina requires characterization of their biointerface with cells and establishing their biocompatibility. Recent studies on P3HT thin films with mouse fibroblasts have demonstrated the biocompatibility and biofunctionalization of active semiconducting polymers ¹⁴². In this chapter, the biocompatibility of the BHJ polymer layers based on P3HT:N2200 has been discussed.

The method of *in vitro* cell culture allows direct investigation of cell–material interactions and provides insight into the tissue compatibility with a material. In addition to the intrinsic cell factors, extrinsic signals to the cell from the surrounding extracellular matrix are essential in guiding it through distinct development paths (**Figure 4.1**). Cells constantly encounter and respond to biophysical cues in their extracellular environment. Substrate topographies with varying microscale dimensions have been used to better

understand cell adhesion, migration, and differentiation at the cellular and sub-cellular scales and have been utilized for neural, cardiac, and musculoskeletal tissue engineering application¹⁴³. Tissue cells including fibroblasts, myocytes and neurons have been shown to sense the substrate stiffness through molecular pathways controlled by adhesion complexes and the actinmyosin cytoskeleton^{144,145}. In particular, determining neuronal growth on artificial substrates and scaffolds is also of significant interest for neuroengineering. Neuronal cells have been cultured on a variety of scaffolds including polymers, silk, metals, semiconductors and hydrogels¹⁴⁶. Along with substrate stiffness and topography, neuronal cells have been shown to respond to electrostatics of the substrate through extracellular matrix proteins and guidance factors which provide critical signals for controlling neuronal behavior like growth cone dynamics, axonal elongation and guidance, neuronal migration and synaptic rearrangement in culture^{147,148}. However, the influence of optoelectronic properties of semiconducting substrates on neuronal networks is relatively less studied.

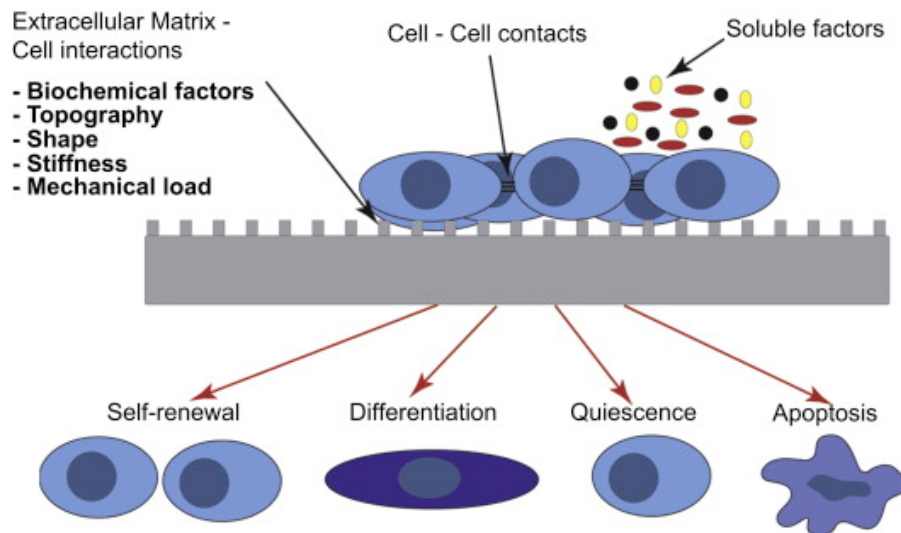


Figure 4.1 Schematic showing various factors determining the cell-material interactions. Adapted with permission from¹⁴⁹.

Cultured dissociated neurons are widely used for investigating the properties of synapses, identifying molecules involved in neural function and studying the dynamics of neural networks. Various experimental techniques of stimulating and recording activity

patterns in many neurons simultaneously have been utilized, but they have their own limitations. For instance, intracellular electrode stimulation incurs a physiological perturbation to the neuron. Culturing cells on MEAs permits a more spatially specific and noninvasive stimulation but the stimulation site is fixed by the electrode position and grid resolution within an array. Photostimulation by neurotransmitter uncaging provides a high degree of experimental flexibility, because a small beam of light can be targeted in any region of the sample. In this method, however, uncaged transmitters can activate extrasynaptic neurotransmitter receptors, thereby limiting spatial resolution and complicating data interpretation. Controlled individual neuron-to-electrode interfacing is a challenging task. The interface between silicon and neurons has been of major interest for developing bioelectronic interfaces and has been utilized to have a control over precise neuronal stimulation. The coupling between the cell membrane and the semiconductor surface can be used to stimulate the neuron through application of voltage pulses to the underlying semiconductor in a 2-terminal capacitor or 3-terminal transistor device geometry¹⁵⁰⁻¹⁵³. Interestingly, a light-addressable neuronal excitation method based on the photoconductive properties of semiconductor/electrolyte interface has also been exploited as an alternative technique for stimulating cultured neurons¹⁵⁴⁻¹⁵⁶. In this method, neuronal cells are cultured on silicon wafers, which are reverse biased with respect to the electrolyte bath. A cell body of interest is illuminated through the microscope aperture. The illumination locally excites the Si substrate, generating a local photoconductive pathway in the region directly beneath the cell and transiently creates a 'virtual' stimulation electrode at that location. The spatiotemporal activities and cellular processes in the neuronal network are then dynamically monitored through patch clamp technique or with fluorescence imaging of various molecular probes. This technique is non-invasive and gives a control over stimulation parameters with high spatiotemporal resolution. This method of photoconductive stimulation of silicon has also been used for studying the cellular and molecular mechanisms underlying the dynamic interactions between neurons, astrocytes and microglia¹⁵⁷.

Semiconducting polymer layers have recently been utilized elsewhere as an alternative to silicon for photoactivation of cultured cells. Neuronal cells cultured on a BHJ layer of P3HT:PC₆₀BM could be electrically stimulated by photoillumination of the BHJ/EI interface²⁸. Photoexcitation of P3HT nanofibres have been shown to promote

regeneration in human fibroblast cells and are shown to have potential application in photocurrent therapy for skin regeneration ¹⁵⁸. In the work described in this Chapter of the thesis, photoillumination of BHJ layers is shown to affect the neuronal growth pattern of dissociated retinal cells. The observations suggest a potential utilization of BHJ layers as interfaces for studying the various synaptic properties within retinal neuronal networks.

4.2 Experimental Methods

4.2.1 Preparation of polymer-coated substrates

Following substrates were used for cell culture: P3HT on ITO-glass, N2200 on ITO-glass, BHJ coated on ITO-glass, ITO-glass only (without polymer coating, as control) and glass coverslips (as control). Pristine polymer solutions of P3HT (from Luminescence Technology Corp., China) and N2200 (from Polyera Corp., USA) were prepared at 10 mg/ml in Chlorobenzene (Sigma Aldrich). The BHJ polymer blend was prepared with P3HT as the donor and N2200 as the acceptor, mixed in 4:1 (w/w), respectively and dissolved in chlorobenzene at a concentration of 10 mg/ml.

The ITO coated glass were cut in 1.2 cm x 1.2 cm square pieces to fit into the 24-well plate that is used for cell-culture. For the cell culture experiments where photoillumination of substrates was used during cell culture, ITO-glass was patterned as shown in **Figure 4.2**. The patterning was done by masking the ITO-glass and chemically etching the ITO using aqua regia (3:1 HCl:HNO₃). All substrates were cleaned with standard protocols (soap, acetone, chloroform, RCA treatment). The polymer solutions were coated on the pre-cleaned substrates using spin coating at 800 rpm for 60 sec. The polymer-coated substrates were annealed at 110 °C for 15 min in air in dark conditions.

4.2.2 Ornithine/Laminin coating

In order to have cell adherence and proliferation in primary cell cultures, the substrates are coated with amino acids like poly-lysine or poly-ornithine, and extracellular matrix proteins like laminin. Ornithine/laminin coatings are well established to promote cell adhesion and proliferation of retinal neurons in culture ^{159,160}.

In our experiments, all substrates were treated with alcohol and UV radiation for 10 min each for sterilization, washed with phosphate buffer saline (PBS), and then coated with L-ornithine and laminin, layer by layer, by self assembly. The working concentration of L-Ornithine (Poly-L-ornithine hydrobromide from Sigma Aldrich) and Laminin (Laminin from Engelbreth-Holm-Swarm murine sarcoma basement membrane from Sigma Aldrich) were 50 µg/ml and 5 µg/ml in PBS. The sterilized substrates were first incubated in ornithine solution for 12 hours. This was followed by washes with PBS (3 times) followed by incubation in laminin solution for 12 hours. Before plating the cells, the ornithine/laminin-coated substrates were washed with PBS (3 times). This procedure was carried out inside the laminar hood and all precautions to avoid contamination were followed. All the further protocols described below were also carried out under similar sterile conditions.

4.2.3 Cell Culture Protocol

Retinas were isolated from C57/BL6 mouse (P0-P2). Retinas from BALB/c mouse strains were also utilized. The tissues were dissociated in a 1 ml EBSS solution consisting of 50 µl of papain (400 U/ml), activated with 1 mM L-cystein and stabilized with 0.5 mM of EDTA. Dissociated cells were triturated in a 1 ml solution of EBSS containing 50 µl of DNaseI (2000 U/ml), 5 µg/ml of leupeptin and 1% Bovine serum Albumin (BSA). The cell pellet was resuspended in the culture medium (Dulbecco's modified Eagle's Medium) containing 4% fetal bovine serum, 1% N2 and 1% B27 supplement, 1% penicillin-streptomycin, and 1% glutamine. Cell density was counted using a hemocytometer and was typically ~ 10⁶/ml. The culture medium was replaced every 3rd-4th day during the growth.

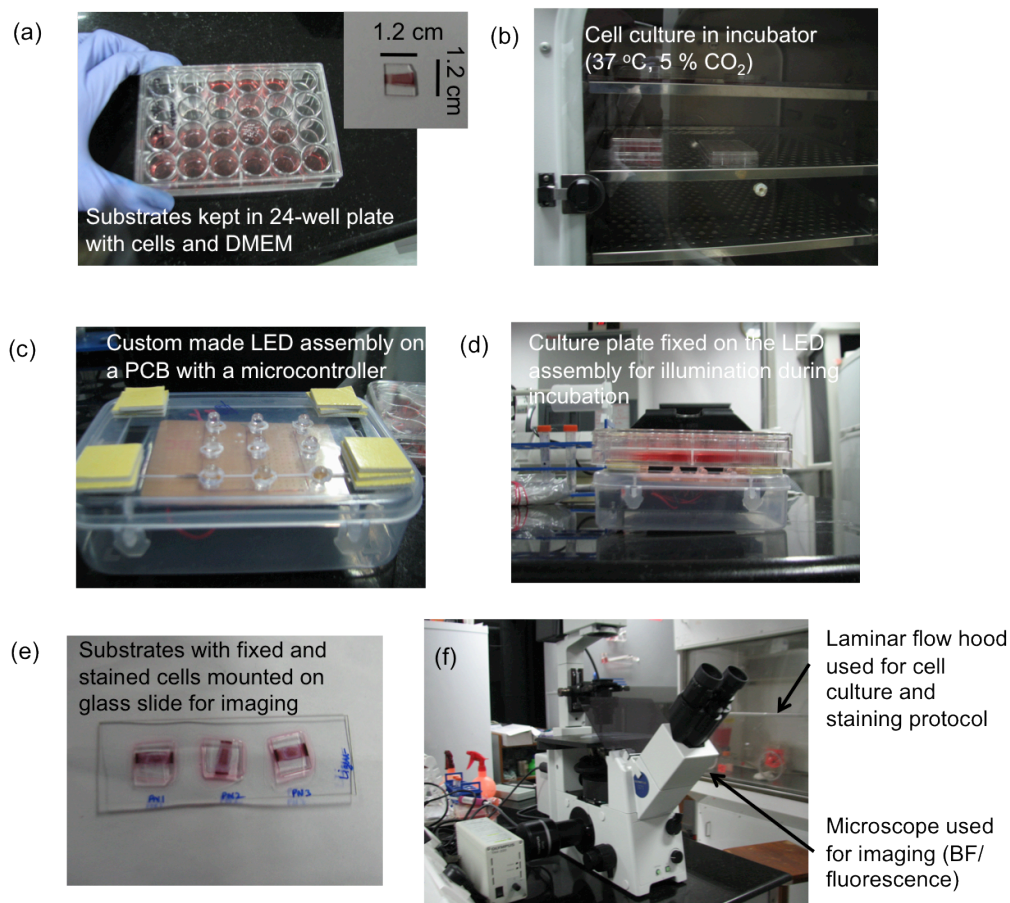


Figure 4.2 Experimental set-up used for stimulation of neurons with BHJ polymer layers during cell culture.

4.2.4 TUNEL assay protocol

In order to examine the cell viability after finite DIV, the retinal cells had to be fixed before carrying out the TUNEL Assay. The retinal cells cultured on the substrates were fixed with ice-cold 4% paraformaldehyde (PFA) solution in PBS for 30 min, followed by PBS washes. The substrates were then subjected to the blocking solution consisting of 0.3% Triton X and 3% bovine serum albumin (BSA) in PBS for 60 min followed by TUNEL stain for 60 min. The mounting solution consisting DAPI was used before imaging of the substrates under the Apotome (Carl Zeiss, Germany) fluorescence microscope.

4.2.5 Photoillumination set-up

For photoillumination of the substrates during the cell culture, a custom-made assembly of green or red LEDs was used. The LEDs were mounted on a printed circuit board with spacing equal to the well-to-well spacing in the 24-well plate. The connections were driven through an Arduino board, which was placed inside a box on which LEDs and the cell-culture plate could be placed. Photoillumination was achieved from the ITO/polymer side by programming the Arduino board with a set pulse width of 250 ms and a pulse interval of 30 sec. A snapshot of this assembly is shown in **Figure 4.2**. One set of each type of the substrates was set as controls by blocking the LED illumination using a black tape. The LED illumination was usually turned on after 12 hours of cell plating.

4.2.6 Neuronal staining protocol

In order to quantify the neuronal growth pattern, immunohistochemical protocols were followed for staining the primary cells in culture. The polymer-coated substrates in the 24-well plate were fixed and stained with neuronal markers. The cell-culture medium is aspirated, substrates washed with PBS, and left in 4% PFA at room temperature for 15 min. The fixed cells are then subjected to 10 mM NH₄Cl-PBS for 10 min, followed by 1% Triton X for 10 min, followed by blocking solution (3 % BSA) for 10 min with intermediate washes with PBS-Tween. A 10 µl solution of the primary antibody (Neuron-specific beta-III Tubulin MAb, Mouse IgG2A) with a 1:200 dilution was then dropped on the substrates and left for 60 min. After subsequent washes with PBS-Tween, secondary staining was done using Alexa Fluor 488 Goat Anti-Rabbit IgG (H+L) antibody (1:1000 dilution) in dark conditions. After washing the excess antibodies with PBS, 20 min incubation in NucBlue cell stain was used for staining the cell nuclei. The substrates were then washed with de-ionized water, aspirated, and mounted with 70% glycerol on a pre-cleaned glass slide and imaged with a fluorescence microscope (**Figure 4.2**).

4.3 Results - Cytotoxicity and Biocompatibility

In order to establish the biocompatibility of the BHJ films utilized in this study, retinal dissociated cell cultures on thin films of BHJ were monitored for up to 10 days in vitro (DIV) in dark conditions. The neuronal cell adhesion and growth was found to be similar on polymer films and the controls (ITO-glass and glass coverslips) as shown in **Figure**

4.3.

TUNEL assay was carried out to quantify the viability of cells on the polymer films (**Figure 4.4**). TUNEL (terminal deoxynucleotidyl transferase-mediated dUTP nick end-labeling) is a common technique to assess cell viability by identification and quantification of the apoptotic cell fraction in cultured cell preparations^{161,162}. The % of apoptotic cells on the BHJ films were compared with that on the control glass coverslips by counting the TUNEL stained cells (red) and the DAPI stained nuclei (blue) using ImageJ. The mean percentage of apoptotic cells on glass and BHJ films was found to be $(17.2 \pm 5.6)\%$ and $(18.8 \pm 4.2)\%$ after 10 DIV.

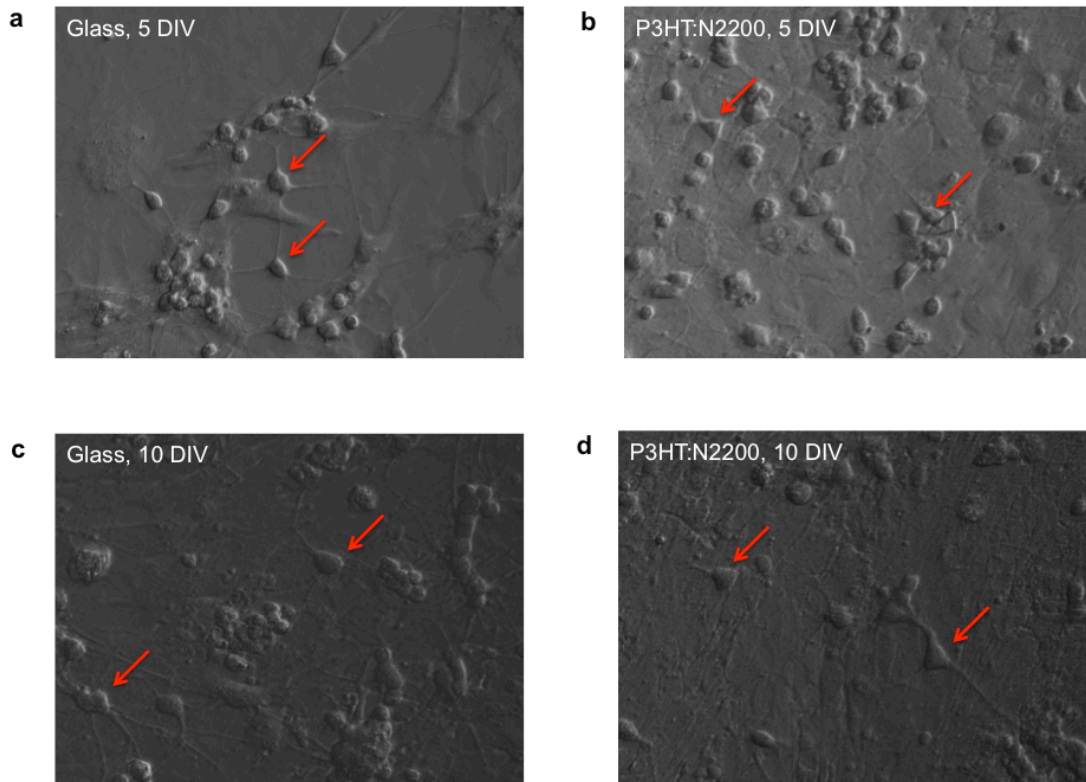


Figure 4.3. Bright field images of retinal cells after 5 DIV and after 10 DIV on Glass and BHJ layer. Some neuronal cells are marked with red arrows.

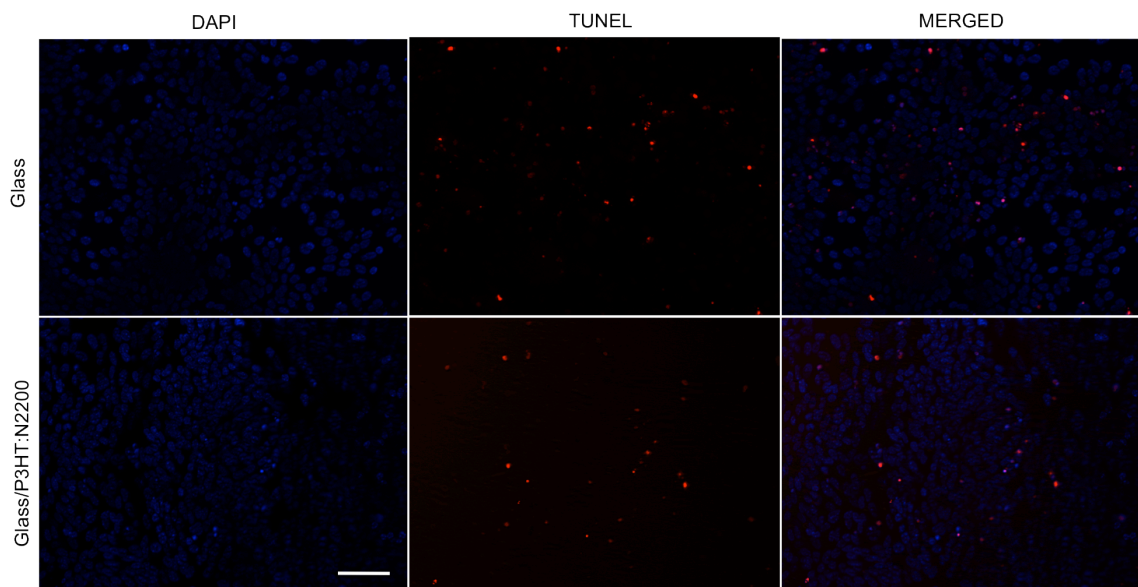


Figure 4.4 Cell viability assay. Representative fluorescence images after TUNEL staining on retinal dissociated cell cultured on (a) Glass, (b) Glass/P3HT:N2200 (4:1) after 10 DIV. Scale bar = 50 μ m. The mean percentage of apoptotic cells on the two substrates is $(17.2 \pm 5.6)\%$ and $(18.8 \pm 4.2)\%$ respectively.

4.4 Results - Cell culture under illumination

The results presented in this section specifically establish the experimental protocol to study the dynamics of interaction between retinal neurons and the active BHJ substrates. Varying photoexcitation parameters and specifically marking each biological component at various cell culture stages will be required to establish the precise mechanism of such interaction. In our experiments, the image analysis procedure after the neuronal staining involved the following steps. For each substrate, bright field images were taken under the microscope, followed by DAPI/NucBlue and β -III Tubulin. The DAPI and β -III Tubulin images were then merged to highlight the fraction of neurons in the specific region (**Figure 4.5**). Merged images of neurons on the BHJ layers are shown in **Figure 4.6**. These images show neuronal cell growth and proliferation on semiconducting polymer layers.

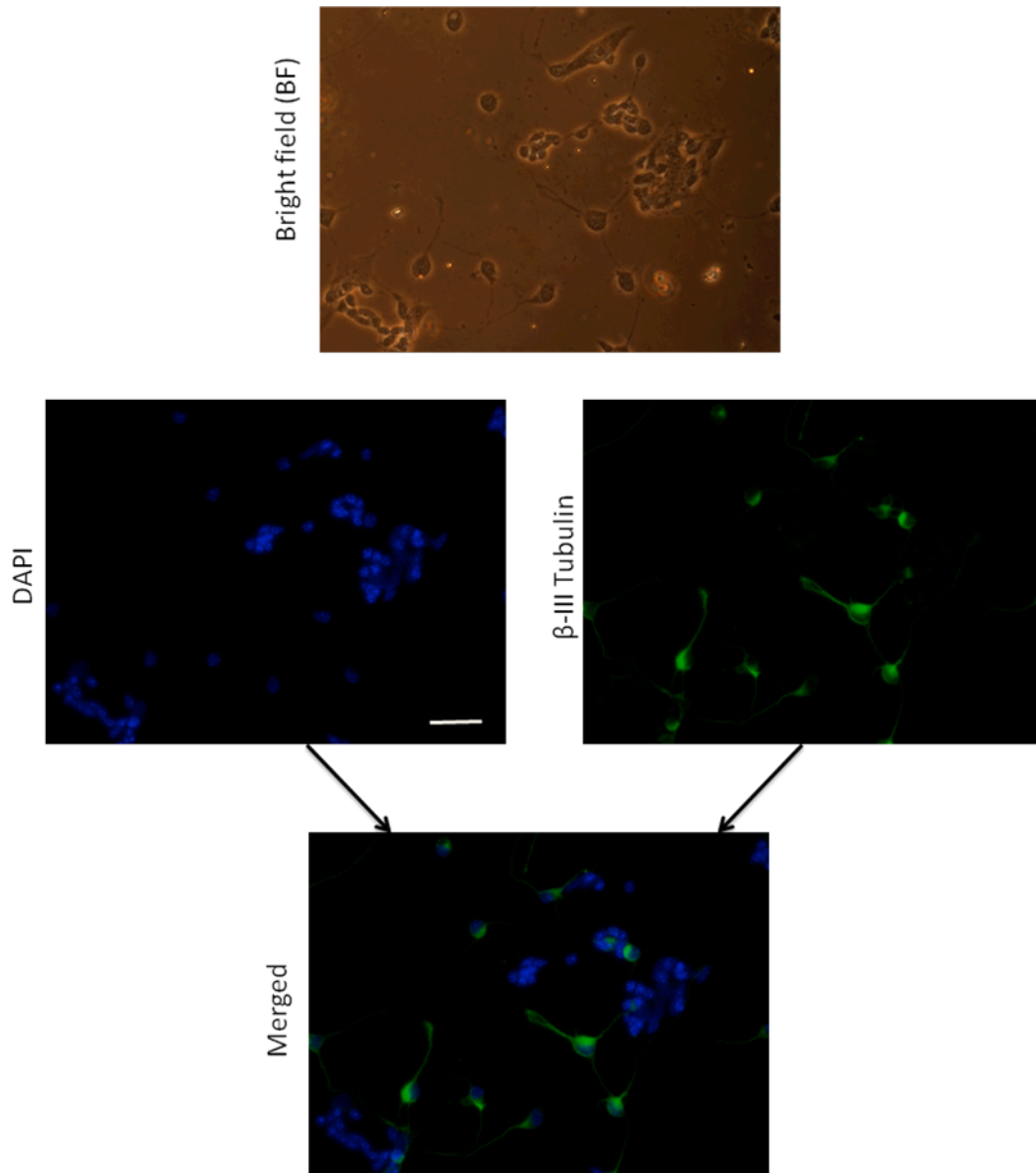


Figure 4.5 Imaging neurons after nuclear and neuronal staining. Image shown for a culture on glass coverslip after 4 DIV. Scale bar = 20 μ m.

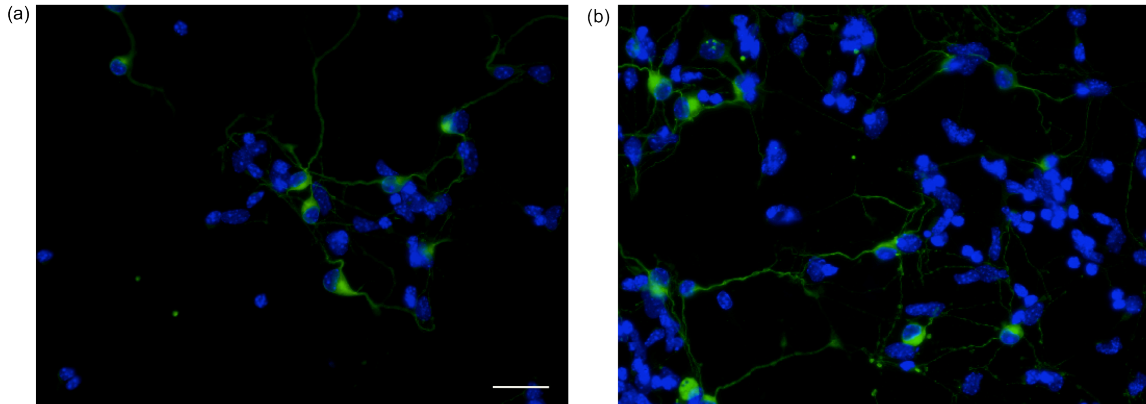


Figure 4.6 Retinal dissociated cells on a BHI layer on two different substrates after 4 DIV. Scale bar = 20 μm .

Representative merged images for the substrates in a culture are shown in **Figure 4.7**. The staining was usually done within 5 DIV to pick up the early stage growth patterns. The rapid glial and neuronal growth on the substrates after 5 DIV was observed to cause a difficulty in identifying a particular growth pattern. On an average, 3 sets of the same type of substrates are stained with markers, and such images are taken for multiple regions of a substrate for improving the statistics. The results presented here were repeated for two sets of cell culture. Due to the patterned polymer layer, cells on glass and on ITO/Polymer region could be compared simultaneously. The fraction of neurons in an image is estimated by taking the ratio of number of cells stained with β -III Tubulin (green) to the total number of cells (stained for nuclei in blue). Preliminary results show that for substrates under dark, the fraction of neurons and the network connections on polymer substrates was slightly more than that on glass. This can be attributed to the mechanical modulus difference between glass and polymer as polymers have been shown to mimic the mechanical environment of the physiological conditions of cells and hence result in a better cell attachment and proliferation. Further, the % increase in the neuronal population is maximum on the PN-type substrates ($\sim 35\%$) under illumination. Some of these preliminary results are summarized in **Figure 4.8**.

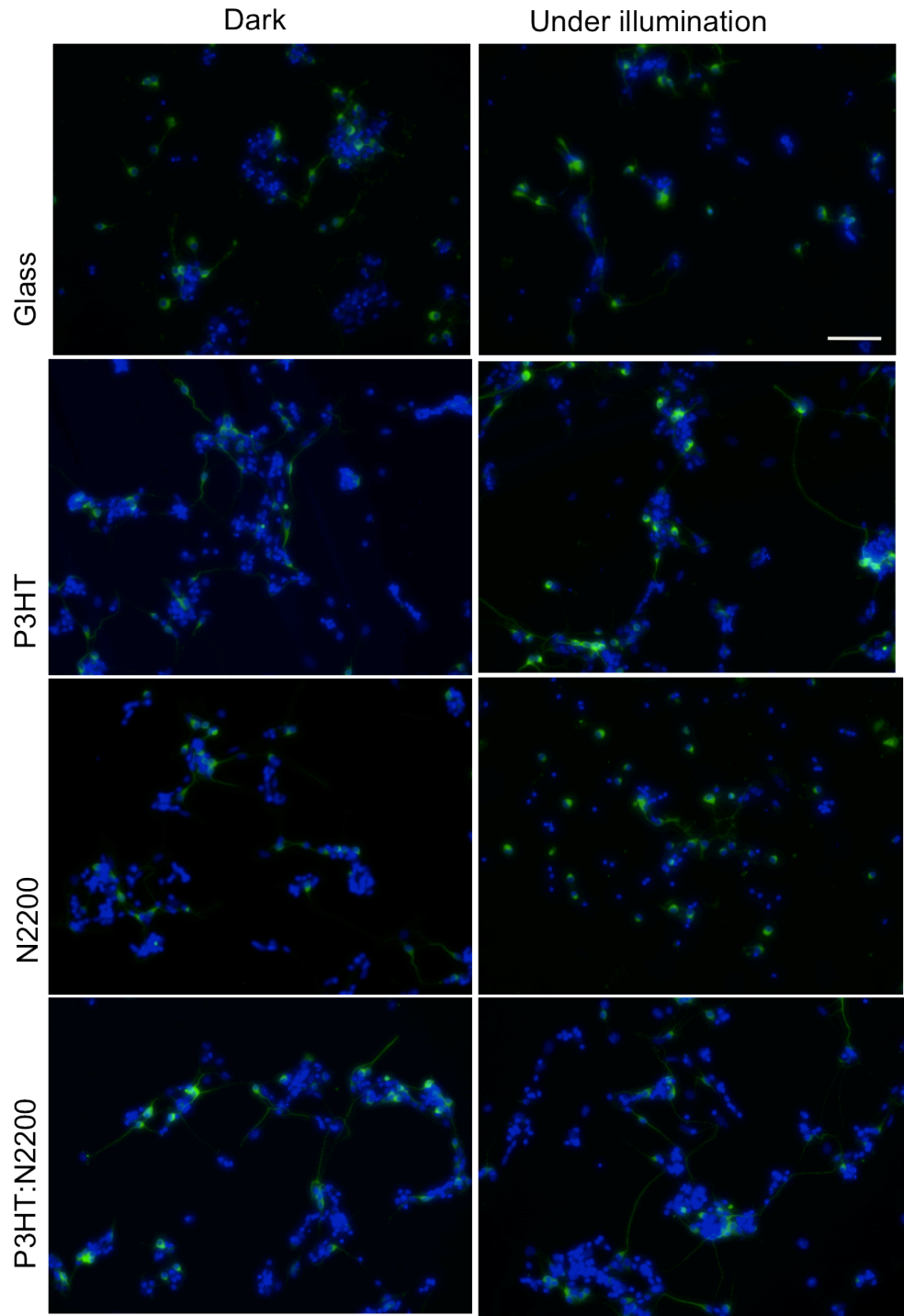
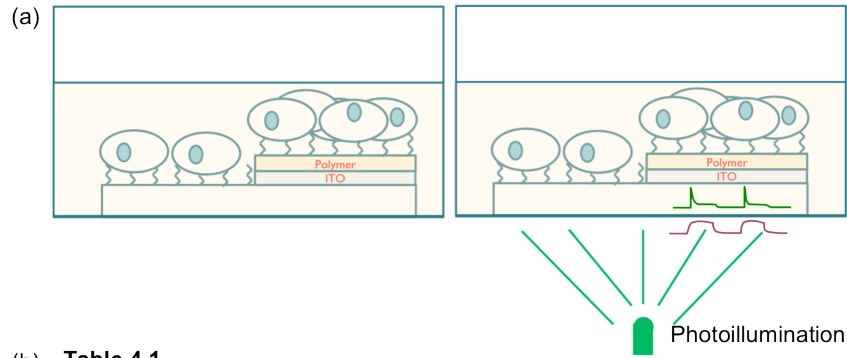


Figure 4.7 Representative images from a retinal cell culture after 4 DIV. Scale bar = 50 μm .



(b) **Table 4.1**

Fraction of Neurons	Dark	Light
Control (Glass)	0.12	0.13
Polymer (BHJ)	0.16	0.22

Figure 4.8 (a) Schematic of the experiment for stimulation of retinal cells with BHJ layers (b) An increase in the average fraction of neurons on photoilluminated BHJ coated substrates.

The optoelectronic signals from the BHJ layers affect the pattern of neuronal growth on the cell culture substrates. A corollary of the enhanced neuronal growth on BHJ layers under illumination can be drawn from previous studies on neuronal culture under electric fields. Previous studies have shown that neurite growth is enhanced on electroactive substrates, for instance the direction of neurite extension, as well as overall differentiation of cells get modified under external electric fields applied to the culturing neuronal cells¹⁴⁸. The observation of such effects is attributed to the various cell-surface interaction mechanisms, which get altered due to external currents and fields: electrophoretic redistribution of cell membrane growth factor and adhesion receptors, conformational change in an extracellular membrane protein, direct depolarization or hyperpolarization of the cell and enhancement of certain protein synthesis^{163,164}. Of these mechanisms, the field induced gradients in ions and molecules in region around the cells are shown to enhance the overall proliferation and differentiation of nerve cells¹⁶⁵. The optoelectronic signals from the BHJ layers possibly induce similar changes in the extracellular space of the nerve cells, and further studies are required to gain an insight into the specific mechanism.

The cell-culture stage chosen for the experiments is specific to the interaction between the adhesion complexes on the neuronal membranes and the active BHJ layers. The cell-surface interaction in culture conditions can usually be divided into four time scales¹⁶⁶. In the earliest stage when the spherical cells are suspended in the medium, the cells are at a distance $> 10 \mu\text{m}$ from the surface and there exist non-specific interactions between the cell membrane and material surface. In the next, early attachment stage, the cells come within 100 nm of the materials surface, and cell membrane proteins like integrins interact with the molecular motifs on the material surface. This stage takes place within seconds of suspending the cells. The intermediate attachment stage is where cells build up more complex molecular anchorages on the materials surface and adhere to it, and completes in the time scale of seconds. The last stage involves a dynamic crosstalk between the cell cytoskeleton and the material surface and involves cell spreading with help of focal adhesion complexes. This process extends from minutes to days of cells in culture. The effect of photoillumination on the increased % neurons on the BHJ layers within 4 DIV arises from the possible modification of the adhesion complexes in the late adhesion stage, which results in attachment of more neurons on the BHJ surface with active optoelectronic signals. Studies involving staining of the cytoskeleton proteins at various stages of the experiment should give a further insight into the precise interaction and adhesion mechanism of neurons on BHJ layers.

4.5 Summary

The retinal dissociated cell culture could be done on pristine and BHJ-polymer layers. Extended duration of cell culture and cell viability assays establish the non-cytotoxicity of these semiconducting polymers towards retinal cells. A method of using the polymer layers as active substrates for neuronal culture has been developed and standardized. Preliminary results show that the photoexcitation of the polymer layers during late-attachment stages of cell culture result in the modification of neuronal network, with higher fraction of neurons growing on the BHJ layers. Studies with varying parameters of intensity, wavelength and duration of photoexcitation could yield interesting insights into these growth patterns on active BHJ substrates. Further studies with specific markers for each-type of retinal cells and cytoskeletal proteins can also give an insight into the kind of networks formed, the fate of photoreceptors and other retinal cells in culture, and the

precise mechanism of the focal adhesion complexes getting affected by the optoelectronic signals of the semiconducting polymer layers.

Chapter 5

Summary and Future Perspective

Advanced polymeric materials can serve as a keystone of new medical technologies and therapies. Selection of appropriate materials and the characterization of the bioelectronic interface play a central role in the prospective success and impact of many of these emerging technologies. Semiconducting polymers have been an attractive choice as active materials for a wide variety of optoelectronic applications and provide suitable alternatives to conventional semiconductor materials, in particular for use as bioelectronic interfaces. This thesis presents the utility of optoelectronic polymer device structures as neuroprosthetic interfaces based on their photodetection capability, which mimics the visual response in natural photosystems. The tunable photoresponse profiles from these artificial receptors could be explored for stimulating a retinal explant and evoking neuronal activity in the blind tissue (**Figure 5.1**). These results have implications towards the development of novel optoelectronic polymer devices for artificial retina applications.

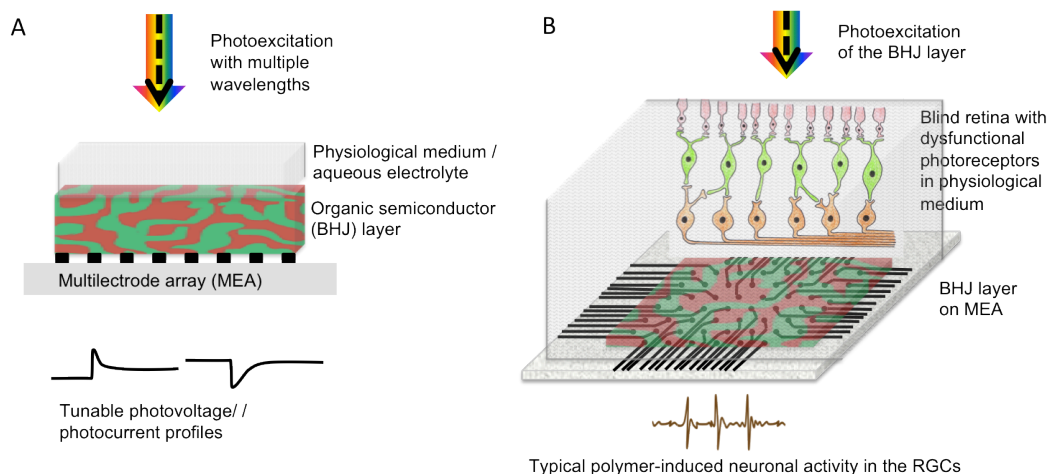


Figure 5.1 Schematic showing (a) Optoelectronic features across the BHJ/electrolyte interface having characteristic transient pulse profiles. (b) The photoexcitation of the BHJ/electrolyte interface resulting in stimulation of a blind retina with dysfunctional photoreceptors.

The research problems addressed in the thesis covered different aspects in this broad pursuit. The initial studies focused on the optoelectronic properties of the interface between BHJ-based semiconducting polymer layers and aqueous electrolytes and physiological media. The photoexcitation of the BHJ/EI interface results in interesting photophysical features, such as crossover in polarity of photocurrent as a function of thickness of the active layer and a crossover in photocapacitance as a function of frequency. These features were modeled to arise from various microscopic transport and morphology characteristics within these device structures, for instance, bulk carrier concentration, diffusion length scales and the presence of different transport mechanisms. Appropriate thickness of the P3HT:N2200 based BHJ layer in these device structures could then be used as a single-pixel, multi-color sensor device. The photodetection properties of these devices resemble natural vision processes and provide a suitable alternative to materials used as artificial photoreceptors. A more detailed optoelectronic characterization of these devices could offer interesting insights into the interfacial and bulk properties of the semiconducting polymer/electrolyte based hybrid devices and could also establish the proposed models for the observed photophysical features arising across these devices. For instance, surface-specific studies like modulation spectroscopy and electroreflection can be implemented to quantify the interfacial charge carrier transport and accumulation at the polymer/EI interface. Further, Kelvin-probe studies on the surface of the BHJ layer in contact with aqueous electrolyte could yield exact values of surface potentials arising at the BHJ/EI interface. A justification based on quantitative assessment of the surface potential and how it can be translated to a proximal neuronal layer to trigger biochemical changes needs to be studied.

The BHJ based photosensitive platform was integrated with a blind chick retina and the interface could stimulate and evoke neuronal activity in the RGCs. The wire-free, solution processable epiretinal approach presented in the thesis simulates the natural response of the retina in absence of an additional power source. The observations demonstrate the use of high sensitivity in semiconducting polymer materials for artificial retina applications. A wide range of other available polymer semiconductors can be tapped in for wider range of spectral response and sensitivity. For instance, future work with alternative strategies of using a BHJ layer with absorption in the NIR spectrum to stimulate the retina could be a possible way to provide augmented vision in retinal

degenerative cases. This approach is specifically advantageous in laboratory in vitro experiments, as it would completely circumvent the issue of remnant photoreceptors in blind retina models.

The cell culture studies and cell viability assays on the BHJ films establish their non-cytotoxicity towards the retinal cells. Previous studies from our laboratory have also shown a stable lipid layer formation on P3HT surfaces (that could be used in a water-gated transistor geometry)⁴², and that P3HT layers could support differentiation of stem cells into neurons¹⁶⁷. These results show the biocompatibility of P3HT in physiological conditions. The application of optoelectronic platforms of semiconducting polymers for artificial retina should involve future studies of establishing in-vivo biocompatibility of these materials. These studies could involve fabricating BHJ layers on flexible substrates with transparent conducting polymer electrodes and implanting them into the ocular space of higher animals like rabbits. Previous studies from our laboratory which involved interfacing the conducting polymer PEDOT:PSS with retinal tissues and stem cells have shown that PEDOT:PSS improves the mechanical modulus mismatch between metal electrodes and a retina¹⁶⁸ and also influences the differentiation of embryonic stem cells into retinal neurons¹⁶⁹. Experiments from our laboratory have also established SEBS as a novel flexible, stretchable and biocompatible substrate¹⁶⁹. The biocompatibility studies of these in-vivo implants should consider the effect of implant on the retinal tissue, for instance a scar or inflammation, as well as the effect of the tissue medium on the implant, for instance degradation of the optoelectronic properties of the polymer layer after being implanted over weeks in physiological medium. Though the stability with physiological media is covered in the work carried out in this thesis, the effect of fibrosis, gliosis and other physiological processes on the polymer layers will have to be established. In addition, encapsulation methods of such implants should be developed so that they can be used for durations of up to years without undergoing degradation due to mechanical and corrosion effects.

The optoelectronic signals from these device structures also manipulate the neuronal networks in primary retinal cell culture. By staining retinal cells with specific markers for each type, and combining the fluorescence imaging with a z-stack confocal microscopy, information on the 3-D neuronal networks growing on the BHJ layers can be extracted.

Specific cytoskeleton markers in cell culture could further be used to study the cell-polymer interaction at early attachment stages and the interaction between molecular motifs on the polymer layer and cell membrane proteins could be quantified. These studies can be extended to picking up activity in neuronal cells using a combination of optical stimulation of the BHJ polymers and probing the neuronal activity using scanning probe microscopy techniques.

Advancements in organic electronics, biomaterials, and flexible devices can improve the integration of synthetic devices with tissues in vivo. Novel biomaterials, new device designs and innovative methods are necessary for rapid and efficient integration of electronic devices and physiological processes to create new medical device technologies. Polymeric optoelectronic devices with intelligent sensing capabilities for repairing and augmenting visual processes in the retina can serve as a suitable alternative to presently used materials as artificial photoreceptors. With the Argus II epiretinal implants and the Alpha IMS subretinal implants demonstrating limited successful results with patients suffering from retinal pigmentosa, the advent of semiconducting polymers with promising virtues should catalyze the pursuit of alternate materials technology for artificial retina applications.

List of References

- 1 Heeger, A. J., Sariciftci, N. S. & Nardas, E. B. *Semiconducting and metallic polymers*. (Oxford University Press, 2010).
- 2 Forrest, S. R. The path to ubiquitous and low-cost organic electronic appliances on plastic. *Nature* **428**, 911-918 (2004).
- 3 Brabec, C. J., Sariciftci, N. S. & Hummelen, J. C. Plastic Solar Cells. *Adv. Funct. Mater.* **11**, 15-26 (2001).
- 4 Gates, B. D. Flexible Electronics. *Science* **323**, 1566-1567 (2009).
- 5 Kim, Y. H. *et al.* Highly Conductive PEDOT:PSS Electrode with Optimized Solvent and Thermal Post-Treatment for ITO-Free Organic Solar Cells. *Adv. Funct. Mater.* **21**, 1076-1081 (2011).
- 6 Yoo, J. E. *et al.* Directly patternable, highly conducting polymers for broad applications in organic electronics. *Proc. Natl. Acad. Sci.* **107**, 5712-5717 (2010).
- 7 Heeger, A. J. Nobel Lecture: Semiconducting and metallic polymers: The fourth generation of polymeric materials. *Rev. Mod. Phys.* **73**, 681-700 (2001).
- 8 Gandhi, M. R., Murray, P., Spinks, G. M. & Wallace, G. G. Mechanism of electromechanical actuation in polypyrrole. *Synthetic Metals* **73**, 247-256 (1995).
- 9 Berggren, M. *et al.* Bi-stable and dynamic current modulation in electrochemical organic transistors. *Adv. Mater.* **14**, 51-54 (2002).
- 10 Chao, S. & Wrighton, M. S. Characterization of a solid-state polyaniline-based transistor: water vapor dependent characteristics of a device employing a poly(vinyl alcohol)/phosphoric acid solid-state electrolyte. *J. Am. Chem. Soc.* **109**, 6627-6631 (1987).
- 11 Zhu, Z. *et al.* A simple poly(3,4-ethylene dioxythiophene)/poly(styrene sulfonic acid) transistor for glucose sensing at neutral pH. *Chem. Commun.*, 1556-1557 (2004).
- 12 Krishnamoorthy, K., Gokhale, R. S., Contractor, A. Q. & Kumar, A. Novel label-free DNA sensors based on poly(3,4-ethylenedioxythiophene). *Chem. Commun.*, 820-821 (2004).

- 13 Berggren, M. & Richter-Dahlfors, A. Organic Bioelectronics. *Adv. Mater.* **19** (2007).
- 14 Richardson-Burns, S. M. *et al.* Polymerization of the conducting polymer poly(3,4-ethylenedioxythiophene) (PEDOT) around living neural cells. *Biomaterials* **28**, 1539-1552 (2007).
- 15 Abidian, M. R., Ludwig, K. A., Marzullo, T. C., Martin, D. C. & Kipke, D. R. Interfacing Conducting Polymer Nanotubes with the Central Nervous System: Chronic Neural Recording using Poly(3,4-ethylenedioxythiophene) Nanotubes. *Adv. Mater.* **21**, 3764-3770 (2009).
- 16 Hyodo, K. Electrochromism of conducting polymers. *Electrochim. Acta.* **39**, 265-272 (1994).
- 17 Somani, P., Mandale, A. B. & Radhakrishnan, S. Study and development of conducting polymer-based electrochromic display devices. *Acta. Mater.* **48**, 2859-2871 (2000).
- 18 Sapp, S. A., Sotzing, G. A. & Reynolds, J. R. High contrast ratio and fast-switching dual polymer electrochromic devices. *Chem. Mater.* **10**, 2101-2108 (1998).
- 19 Gunes, S., Neugebauer, H. & Sariciftci, N. S. Conjugated polymer-based organic solar cells. *Chem. Rev.* **107**, 1324-1338 (2007).
- 20 Brabec, C. J. Organic photovoltaics. *Sol. Energy Mater. Sol. Cells* **83**, 273 (2004).
- 21 Demming, A., Krebs, F. C. & Chen, H. Organic photovoltaics. *Nanotechnology* **24**, 480201 (2013).
- 22 Kulkarni, A. P., Tonzola, C. J., Babel, A. & Jenekhe, S. A. Electron transport materials for organic light-emitting diodes. *Chem. Mater.* **16**, 4556-4573 (2004).
- 23 Burroughes, J. *et al.* Light-emitting diodes based on conjugated polymers. *Nature* **347**, 539-541 (1990).
- 24 Dodabalapur, A. Organic light emitting diodes. *Solid State Commun.* **102**, 259-267 (1997).
- 25 Sirringhaus, H. Device physics of solution processed organic field effect transistors. *Adv. Mater.* **17**, 2411-2425 (2005).
- 26 Horowitz, G. Organic field-effect transistors. *Adv. Mater.* **10**, 365-377 (1998).

- 27 Benfenati, V. *et al.* A transparent organic transistor structure for bidirectional stimulation and recording of primary neurons. *Nat. Mater.* **12**, 672-680 (2013).
- 28 Ghezzi, D. *et al.* A hybrid bioorganic interface for neuronal photoactivation. *Nat. Commun.* **2**, 166 (2011).
- 29 Toffanin, S. *et al.* N-type perylene-based organic semiconductors for functional neural interfacing. *J. Mater. Chem. B* **1**, 3850-3859 (2013).
- 30 Cramer, T. *et al.* Organic ultra-thin film transistors with a liquid gate for extracellular stimulation and recording of electric activity of stem cell-derived neuronal networks. *Phys. Chem. Chem. Phys.* **15**, 3897-3905 (2013).
- 31 Ghezzi, D. *et al.* A polymer optoelectronic interface restores light sensitivity in blind rat retinas. *Nat. Photon.* **7**, 400-406 (2013).
- 32 Campbell, I. H., Haggler, T. W., Ferraris, D. L. & Smith, J. P. Direct measurements of conjugated polymer electronic excitation energies using metal/polymer/metal structures. *Phys. Rev. Lett.* **76(11)**, 1900-1903 (1996).
- 33 Heeger, A. J. 25th Anniversary Article: Bulk Heterojunction Solar Cells: Understanding the Mechanism of Operation. *Adv. Mater.* **26**, 10-28 (2014).
- 34 Halls, J. J. M. *et al.* Efficient Photodiodes From Interpenetrating Polymer Networks. *Nature* **376**, 498-500 (1995).
- 35 Yu, G., Gao, J., Hummelen, J. C., Wudl, F. & Heeger, A. J. Polymer Photovoltaic Cells - Enhanced Efficiencies Via a Network of Internal Donor-Acceptor Heterojunctions. *Science* **270**, 1789-1791 (1995).
- 36 Clarke, T. M. & Durrant, J. R. Charge Photogeneration in Organic Solar Cells. *Chem. Rev.* **110**, 6736-6767 (2010).
- 37 Blom, P. W. M., Mihailetschi, V. D., Koster, L. J. A. & Markov, D. E. Device Physics of Polymer:Fullerene Bulk Heterojunction Solar Cells. *Adv. Mater.* **19**, 1551-1566 (2007).
- 38 Koch, N. Organic electronic devices and their functional interfaces. *Chem. Phys. Chem* **8**, 1438-1455 (2007).
- 39 Licht, S. Multiple band gap semiconductor/electrolyte solar energy conversion. *J. Phys. Chem. B* **105**, 6281-6294 (2001).

- 40 Sergawie, A., Yohannes, T., Gunes, S., Neugebauer, H. & Sariciftci, N. S. Photoelectrochemical cells based on emeraldine base form of polyaniline. *J. Braz. Chem. Soc.* **18**, 1189-1193 (2007).
- 41 Yohannes, T., Solomon, T. & Inganas, O. Polymer-electrolyte-based photoelectrochemical solar energy conversion with poly(3-methylthiophene) photoactive electrode. *Synthetic Metals* **82**, 215-220 (1996).
- 42 Narayan, K. S., Madhushankar, B. N., Gautam, V., Senanayak, S. P. & Shivanna, R. Water-Gated Phospholipid-Monolayer Organic Field Effect Transistor Through Modified Mueller-Montal Method. *Electron Device Letters, IEEE* **34**, 310-312 (2013).
- 43 Ofer, D., Crooks, R. M. & Wrighton, M. S. Potential dependence of the conductivity of highly oxidized polythiophenes, polypyrroles, and polyaniline - finite windows of high conductivity. *J. Am. Chem. Soc.* **112**, 7869-7879 (1990).
- 44 Xia, Y., Xie, W., Ruden, P. P. & Frisbie, C. D. Carrier Localization on Surfaces of Organic Semiconductors Gated with Electrolytes. *Phys. Rev. Lett.* **105** (2010).
- 45 Mora-Sero, I. & Bisquert, J. Breakthroughs in the Development of Semiconductor-Sensitized Solar Cells. *J. Phys. Chem. Lett.* **1**, 3046-3052 (2010).
- 46 Nattestad, A. *et al.* Highly efficient photocathodes for dye-sensitized tandem solar cells. *Nat. Mater.* **9**, 31-35 (2010).
- 47 Balasingam, S. K., Lee, M., Kang, M. G. & Jun, Y. Improvement of dye-sensitized solar cells toward the broader light harvesting of the solar spectrum. *Chem. Comm.* **49**, 1471-1487 (2013).
- 48 Lai, Q. *et al.* Ionic/Electronic Hybrid Materials Integrated in a Synaptic Transistor with Signal Processing and Learning Functions. *Adv. Mater.* **22**, 2448-2453 (2010).
- 49 Memming, R. & Schwandt, G. Potential distribution and formation of surface states at the siliconelectrolyte interface. *Surface Science* **4** (1996).
- 50 Tan, M. X., Lewis, C. N. & Kenyon, N. S. Experimental measurement of quasi-Fermi levels at an illuminated semiconductor/liquid contact. *J. Phys. Chem.* **98**, 4959 (1994).
- 51 Gerischer, H. & Lubke, M. On the etching of silicon by oxidants in ammonium fluoride. *J. Electroanal. Chem.* **135**, 2782 (1995).

- 52 Kovacs, I. K. & Horvai, G. Possibilities of chemical sensing at the semiconductor/electrolyte interface. *Sensors and Actuators B* **18**, 315-320 (1994).
- 53 Tomkiewics, M. Impedance spectroscopy of rectifying semiconductor-electrolyte interfaces. *Electrochim. Acta* **35**, 1631-1635 (1990).
- 54 Arutyunyan, V. M. Physical Properties of the semiconductor-electrolyte interfaces. *Sov. Phys. Usp* **32(6)**, 521 (1989).
- 55 Bressers, P. M. M., Meulenlamp, J. W. J. & Knapen, E. A. Visible light emission from a porous silicon/solution diode. *J. Electroanal.Chem.* **61**, 108 (1992).
- 56 Gerischer, H. Impact of semiconductors on the concepts of electrochemistry. *Electrochim. Acta* **35**, 1677-1699 (1990).
- 57 Kandel, E. R., Schwartz, J. & Jessell, T. *Principles of Neural Science*. (Mc-Graw Hill, 2000).
- 58 Kolb, H. How the Retina Works. *Amer. Sci.* **91**, 28-35 (2003).
- 59 Rabinovich, M. I., Varona, P., Selverston, A. I. & Abarbanel, H. D. I. Dynamical principles in neuroscience. *Rev. Mod. Phys.* **78**, 1213-1265 (2006).
- 60 Solomon, S. G. & Lennie, P. The machinery of colour vision. *Nature Rev. Neuroscience* **8**, 276-286 (2007).
- 61 Hodgkin, A. F. & Huxley, A. F. Measurement of current-voltage relations in the membrane of the giant axon of Loligo. *J. Physiol.* **116**, 424-448 (1952).
- 62 Hodgkin, A. F. & Huxley, A. F. The components of membrane conductance in the giant axon of Loligo. *J. Physiol.* **116**, 473-496 (1952).
- 63 Hodgkin, A. F. & Huxley, A. F. Currents carried by sodium and potassium ions through the membrane of the giant axon of Loligo. *J. Physiol.* **116**, 449-472 (1952).
- 64 Hodgkin, A. F. & Huxley, A. F. A quantitative description of membrane current and its application to conduction and excitation in nerve. *J. Physiol.* **117** (1952).
- 65 Neher, E. & Sakmann, B. Single-channel currents recorded from membrane of denervated frog muscle fibres. *Nature* **260**, 799-802 (1976).
- 66 Molleman, A. *Patch Clamping: An Introductory Guide To Patch Clamp Electrophysiology* (John Wiley and Sons Ltd., 2003).

- 67 Thomas, C. A., Springer, P. A., Loeb, G. E., Berwald-Netter, Y. & Okun, L. M. A miniature microelectrode array to monitor the bioelectric activity of cultured cells. *Exp. Cell. Res.* **74**, 61-66 (1972).
- 68 Stett, A. *et al.* Biological application of microelectrode arrays in drug discovery and basic research. *Anal. Bioanal. Chem.* **377**, 486-495 (2003).
- 69 Spira, M. E. & Hai, A. Multi-electrode array technologies for neuroscience and cardiology. *Nature Nanotechnol.* **8**, 83-94 (2013).
- 70 Gong, X. *et al.* Semiconducting polymer photodetectors with electron and hole blocking layers. *Sensors* **10**, 6488-6496 (2010).
- 71 Kraft, T., Schneeweis, D. & Schnapf, J. Visual transduction in human rod photoreceptors. *J. Physiol.* **464**, 747-765 (1993).
- 72 Gong, X. *et al.* High-Detectivity Polymer Photodetectors with Spectral Response from 300 nm to 1450 nm. *Science* **325**, 1665-1667 (2009).
- 73 Bowmaker, J. K. & Dartnall, H. J. Visual pigments of rods and cones in a human retina. *J. Physiol.* **298**, 501-511 (1980).
- 74 Schilinsky, P., Waldauf, C., Hauch, J. & Brabec, C. J. Polymer photovoltaic detectors: progress and recent developments. *Thin Solid Films* **451**, 105-108 (2004).
- 75 Nassi, J. J. & Callaway, E. M. Parallel processing strategies of the primate visual system. *Nature Reviews Neuroscience* **10**, 360-372 (2009).
- 76 Mazzoni, F., Novelli, E. & Strettoi, E. Retinal Ganglion Cells Survive and Maintain Normal Dendritic Morphology in a Mouse Model of Inherited Photoreceptor Degeneration. *J. Neuroscience* **28**, 14282-14292 (2008).
- 77 Weiland, J. D., Cho, A. K. & Humayun, M. S. Retinal Prostheses: Current Clinical Results and Future Needs. *Ophthalmology* **118**, 2227-2237 (2011).
- 78 Ramsden, C. M. *et al.* Stem cells in retinal regeneration: past, present and future. *Development* **140**, 2576-2585 (2013).
- 79 Otani, A. *et al.* Rescue of retinal degeneration by intravitreally injected adult bone marrow derived lineage-negative hematopoietic stem cells. *J. Clinical Invest.* **114**, 765-774 (2004).

- 80 Enzmann, V., Yolcu, E., Kaplan, H. J. & Ildstad, S. T. Stem cells as tools in regenerative therapy for retinal degeneration. *Arch. Ophthalmol.* **127**, 563-571 (2009).
- 81 Busskamp, V. *et al.* Genetic Reactivation of Cone Photoreceptors Restores Visual Responses in Retinitis Pigmentosa. *Science* **329**, 413-417 (2010).
- 82 Cepko, C. L. Emerging Gene Therapies for Retinal Degenerations. *J. Neuroscience* **32**, 6415-6420 (2012).
- 83 Busskamp, V., Picaud, S., Sahel, J. A. & Roska, B. Optogenetic therapy for retinitis pigmentosa. *Gene Ther.* **19**, 169-175 (2012).
- 84 Williams, S. C. P. & Deisseroth, K. Optogenetics. *Proc. Natl. Acad. Sci.* **110**, 16287 (2013).
- 85 Cronin, T. & Bennett, J. Switching on the Lights: The Use of Optogenetics to Advance Retinal Gene Therapy. *Mol. Ther.* **19**, 1190-1192 (2011).
- 86 Takano, Y. *et al.* Study of drug effects of calcium channel blockers on retinal degeneration of rd mouse. *Biochem. Biophys. Res. Commun.* **313**, 1015-1022 (2004).
- 87 Delyfer, M.-N. *et al.* Inherited retinal degenerations: therapeutic prospects. *Biology of the Cell* **96**, 261-269 (2004).
- 88 MacLaren, R. E. *et al.* Retinal repair by transplantation of photoreceptor precursors. *Nature* **444**, 203-207 (2006).
- 89 Little, C. W. *et al.* Transplantation of human fetal retinal pigment epithelium rescues photoreceptor cells from degeneration in the Royal College of Surgeons rat retina. *Invest. Ophthalmol. Vis. Sci.* **37**, 204-211 (1996).
- 90 Chow, A. Y. *et al.* The artificial silicon retina microchip for the treatment of vision loss from retinitis pigmentosa. *Arch. Ophthalmol.* **122**, 460-469 (2004).
- 91 Stett, A., Barth, W., Weiss, S., Haemmerle, H. & Zrenner, E. Electrical multisite stimulation of the isolated chicken retina. *Vision Res.* **40**, 1785-1795 (2000).
- 92 Stett, A., Mai, A. & Herrmann, T. Retinal charge sensitivity and spatial discrimination obtainable by subretinal implants: key lessons learned from isolated chicken retina. *J. Neural Eng.* **4**, S7 (2007).
- 93 Zrenner, E. *et al.* Subretinal electronic chips allow blind patients to read letters and combine them to words. *Proc. R. Soc. B: Biological Sciences* (2010).

- 94 Mathieson, K. *et al.* Photovoltaic retinal prosthesis with high pixel density. *Nature Photon.* **6**, 391-397 (2012).
- 95 Zrenner, E. Will Retinal Implants Restore Vision? *Science* **295**, 1022-1025 (2002).
- 96 Rizzo, J. F., Wyatt, J., Loewenstein, J., Kelly, S. & Shire, D. Methods and perceptual thresholds for short-term electrical stimulation of human retina with microelectrode arrays. *Invest. Ophthalmol. Visual Sci.* **44**, 5355-5361 (2003).
- 97 Humayun, M. S. *et al.* Visual perception in a blind subject with a chronic microelectronic retinal prosthesis. *Vision Res.* **43**, 2573-2581 (2003).
- 98 da Cruz, L. *et al.* The Argus II epiretinal prosthesis system allows letter and word reading and long-term function in patients with profound vision loss. *British J. Ophthalmol.* (2013).
- 99 Stingl, K. *et al.* Artificial vision with wirelessly powered subretinal electronic implant alpha-IMS. *Proc. R. Soc. B: Biological Sciences* **280** (2013).
- 100 Antognazza, M. R., Scherf, U., Monti, P. & Lanzani, G. Organic-based tristimuli colorimeter. *Appl. Phys. Lett.* **90**, 163509-163511 (2007).
- 101 Chen, E. *et al.* Polymer photodetector with voltage-adjustable photocurrent spectrum. *Appl. Phys. Lett.* **96**, 043507-043509 (2010).
- 102 Punke, M. *et al.* Dynamic characterization of organic bulk heterojunction photodetectors. *Appl. Phys. Lett.* **91**, 071118-071120 (2007).
- 103 Schilinsky, P., Waldauf, C. & Brabec, C. J. Recombination and loss analysis in polythiophene based bulk heterojunction photodetectors. *Appl. Phys. Lett.* **81**, 3885-3887 (2002).
- 104 Wang, X. *et al.* Integrated thin-film polymer/fullerene photodetectors for on-chip microfluidic chemiluminescence detection. *Lab. Chip* **7**, 58-63 (2007).
- 105 Nalwa, K. S. *et al.* Polythiophene-Fullerene Based Photodetectors: Tuning of Spectral Response and Application in Photoluminescence Based (Bio)Chemical Sensors. *Adv. Mater.* **22**, 4157-4161 (2010).
- 106 Yu, G. *et al.* Large area, full-color, digital image sensors made with semiconducting polymers. *Synthetic Metals* **111**, 133-137 (2000).

- 107 Antognazza, M. R., Ghezzi, D., Musitelli, D., Garbugli, M. & Lanzani, G. A hybrid solid-liquid polymer photodiode for the bioenvironment. *Appl. Phys. Lett.* **94**, 243501-243503 (2009).
- 108 Chen, Z., Zheng, Y., Yan, H. & Facchetti, A. Naphthalenedicarboximide- vs Perylenedicarboximide-Based Copolymers. Synthesis and Semiconducting Properties in Bottom-Gate N-Channel Organic Transistors. *J. Am. Chem. Soc.* **131**, 8-9 (2009).
- 109 Kergoat, L. *et al.* A Water-Gate Organic Field-Effect Transistor. *Adv. Mater.* **22**, 2565-2569 (2010).
- 110 Yan, H. *et al.* A high-mobility electron-transporting polymer for printed transistors. *Nature* **457**, 679-U671 (2009).
- 111 Cahen, Y. J. N. F. M. S. T. H. D. Bacteriorhodopsin (bR) as an electronic conduction medium: Current transport through bR-containing monolayers. *Proc. Natl. Acad. Sci. U.S.A.* **103**, 8601-8606 (2006).
- 112 He, T., Friedman, N., Cahen, D. & Sheves, M. Bacteriorhodopsin Monolayers for Optoelectronics: Orientation and Photoelectric Response on Solid Supports. *Adv. Mater.* **17**, 1023-1027 (2005).
- 113 Fabiano, S. *et al.* Role of photoactive layer morphology in high fill factor all-polymer bulk heterojunction solar cells. *J. Mater. Chem.* **21**, 5891-5896 (2011).
- 114 Rivnay, J. *et al.* Unconventional Face-On Texture and Exceptional In-Plane Order of a High Mobility n-Type Polymer. *Adv. Mater.* **22**, 4359-4363 (2010).
- 115 Schuettfort, T. *et al.* Surface and Bulk Structural Characterization of a High-Mobility Electron-Transporting Polymer. *Macromolecules* **44**, 1530-1539 (2011).
- 116 Abe, T. & Nagai, K. Novel photofunctions of bilayer composed of p-type phthalocyanine and n-type organic semiconductor as photoelectrodes in the water phase. *Organic Electronics* **8**, 262-271 (2007).
- 117 Abe, T. *et al.* An efficient oxidation at photofunctional interface of phthalocyanine in combination with fullerene. *J. Electroanal. Chem.* **599**, 65-71 (2007).
- 118 Bag, M. & Narayan, K. S. Universality in the intensity-modulated photocurrent in bulk-heterojunction polymer solar cells. *Phys. Rev. B* **82**, 075308 (2010).
- 119 Sato, N. *Electrochemistry at metal and semiconductor electrodes.* (Elsevier, 2003).

- 120 Wang, Y. B., Yuan, R. K. & Willander, M. Capacitance of semiconductor-electrolyte junction and its frequency dependence. *Appl. Phys. A* **63**, 481-486 (1996).
- 121 Boyer, A., Dery, M., Selles, P., Arbour, C. & Boucher, F. Color Discrimination By Forward And Reverse Photocurrents In Bacteriorhodopsin-Based Photosensor. *Biosensors Bioelectron.* **10**, 415-422 (1995).
- 122 Lörinczi, É. *et al.* Voltage- and pH-Dependent Changes in Vectoriality of Photocurrents Mediated by Wild-type and Mutant Proteorhodopsins upon Expression in *Xenopus* Oocytes. *J. Mol. Biol.* **393**, 320-341 (2009).
- 123 Gräber, P. & Trissl, H.-W. On the rise time and polarity of the photovoltage generated by light gradients in chloroplast suspensions. *FEBS Lett.* **123**, 95-99 (1981).
- 124 Paillotin, G., Dobek, A., Breton, J., Leibl, W. & Trissl, H. W. Why does the light-gradient photovoltage from photosynthetic organelles show a wavelength-dependent polarity? *Biophys. Journal* **65**, 379-385 (1993).
- 125 Loop, M. S. & Crossman, D. K. High color-vision sensitivity in macaque and humans. *Vis. Neuroscience* **17**, 119-125 (2000).
- 126 Bader, C. R., MacLeish, P. R. & Schwartz, E. A. Responses to light of solitary rod photoreceptors isolated from tiger salamander retina. *Proc. Natl. Acad. Sci.* **75**, 3507-3511 (1978).
- 127 Bader, C. R., Macleish, P. R. & Schwartz, E. A. A voltage-clamp study of the light response in solitary rods of the tiger salamander. *J. Physiol.* **296**, 1-26 (1979).
- 128 Lisman, J. E. & Brown, J. E. Light-induced changes of sensitivity in *Limulus* ventral photoreceptors. *J. General Physiol.* **66**, 473-488 (1975).
- 129 Butterwick, A. *et al.* Effect of shape and coating of a subretinal prosthesis on its integration with the retina. *Exp. Eye Res.* **88**, 22-29 (2009).
- 130 Shoval, A. *et al.* Carbon nanotube electrodes for effective interfacing with retinal tissue. *Frontiers Neuroeng.* **3**, 12 (2010).
- 131 Boynton, R. M. Rapid Chromatic Adaptation and the Sensitivity Functions of Human Color Vision. *J. Opt. Soc. Am.* **46**, 172-179 (1956).
- 132 Zhou, Y., Liu, X. & Liang, P.-J. The dual-peak light response of ganglion cells in chicken retina. *Brain Res.* **1138**, 104-110 (2007).

- 133 Daniel, K. F., Joseph, F. R., III & Shelley, I. F. Encoding visual information in retinal ganglion cells with prosthetic stimulation. *J. Neural Eng.* **8**, 035005 (2011).
- 134 Sekirnjak, C. *et al.* Electrical Stimulation of Mammalian Retinal Ganglion Cells With Multielectrode Arrays. *J. Neurophysiol.* **95**, 3311-3327 (2006).
- 135 Greenwald, S. H. *et al.* Brightness as a Function of Current Amplitude in Human Retinal Electrical Stimulation. *Invest. Ophthalmol. Vis. Sci.* **50**, 5017-5025 (2009).
- 136 Mesut, S. & Yanmei, T. Non-rectangular waveforms for neural stimulation with practical electrodes. *J. Neural Eng.* **4**, 227 (2007).
- 137 Eickenscheidt, M., Jenkner, M., Thewes, R., Fromherz, P. & Zeck, G. n. Electrical Stimulation of Retinal Neurons in Epiretinal and Subretinal Configuration using a Multi-Capacitor-Array. *J. Neurophysiol.* (2012).
- 138 Zrenner, E. *et al.* Can subretinal microphotodiodes successfully replace degenerated photoreceptors? *Vision Res.* **39**, 2555-2567 (1999).
- 139 Palanker, D., Vankov, A., Huie, P. & Baccus, S. Design of a high-resolution optoelectronic retinal prosthesis. *J. Neural Eng.* **2**, S105 (2005).
- 140 Ziats, N. P., Miller, K. M. & Anderson, J. M. In vitro and in vivo interactions of cells with biomaterials. *Biomaterials* **9**, 5-13 (1988).
- 141 Ratner, B. D. & Bryant, S. J. Biomaterials: Where We Have Been and Where We are Going. *Ann. Rev. Biomedical Engg.* **6**, 41-75 (2004).
- 142 Scarpa, G., Idzko, A.-L., Götz, S. & Thalhammer, S. Biocompatibility Studies of Functionalized Regioregular Poly(3-hexylthiophene) Layers for Sensing Applications. *Macromolecular Bioscience* **10**, 378-383 (2010).
- 143 Nikkhah, M., Edalat, F., Manoucheri, S. & Khademhosseini, A. Engineering microscale topographies to control the cell-substrate interface. *Biomaterials* **33**, 5230-5246 (2012).
- 144 Saxod, R. & Bizet, M.-C. Substrate effects on the dynamics of neurite growth in vitro: A quantitative multi-parametric analysis. *Intl. J. Dev. Neuroscience* **6**, 177-191 (1988).
- 145 Discher, D. E., Janmey, P. & Wang, Y.-I. Tissue cells feel and respond to the stiffness of their substrate. *Science* **310**, 1139-1143 (2005).
- 146 Khan, S. & Newaz, G. A comprehensive review of surface modification for neural cell adhesion and patterning. *J. Biomedical Mater. Res. A* **93**, 1209-1224 (2010).

- 147 Lander, A. D. Understanding the molecules of neural cell contacts: emerging patterns of structure and function. *Trends in Neurosciences* **12**, 189-195 (1989).
- 148 Patel, N. & Poo, M. Orientation of neurite growth by extracellular electric fields. *J. Neuroscience* **2**, 483-496 (1982).
- 149 Kolind, K., Leong, K. W., Besenbacher, F. & Foss, M. Guidance of stem cell fate on 2D patterned surfaces. *Biomaterials* **33**, 6626-6633 (2012).
- 150 Fromherz, P., Offenhausser, A., Vetter, T. & Weis, J. A neuron-silicon junction: a Retzius cell of the leech on an insulated-gate field-effect transistor. *Science* **252**, 1290-1293 (1991).
- 151 Zeck, G. n. & Fromherz, P. Noninvasive neuroelectronic interfacing with synaptically connected snail neurons immobilized on a semiconductor chip. *Proc. Natl. Acad. Sci.* **98**, 10457-10462 (2001).
- 152 Patolsky, F. *et al.* Detection, Stimulation, and Inhibition of Neuronal Signals with High-Density Nanowire Transistor Arrays. *Science* **313**, 1100-1104 (2006).
- 153 Vassanelli, S. & Fromherz, P. Transistor Probes Local Potassium Conductances in the Adhesion Region of Cultured Rat Hippocampal Neurons. *J. Neuroscience* **19**, 6767-6773 (1999).
- 154 Starovoytov, A., Choi, J. & Seung, H. S. Light-directed electrical stimulation of neurons cultured on silicon wafers. *J. Neurophysiol.* **93**, 1090-1098 (2005).
- 155 Goda, Y. & Colicos, M. A. Photoconductive stimulation of neurons cultured on silicon wafers. *Nature Protocols* **1**, 461-467 (2006).
- 156 Giacomello, M. *et al.* Stimulation of Ca²⁺ signals in neurons by electrically coupled electrolyte-oxide-semiconductor capacitors. *J. Neuroscience Methods* **198**, 1-7 (2011).
- 157 Hung, J., Chansard, M., Ousman, S. S., Nguyen, M. D. & Colicos, M. A. Activation of microglia by neuronal activity: Results from a new in vitro paradigm based on neuronal-silicon interfacing technology. *Brain, Behavior and Immunity* **24**, 31-40 (2010).
- 158 Jin, G., Prabhakaran, M. P., Kai, D., Kotaki, M. & Ramakrishna, S. Electrospun photosensitive nanofibers: potential for photocurrent therapy in skin regeneration. *Photochem. Photobiol. Sci.* **12**, 124-134 (2013).
- 159 Smalheiser, N. R., Crain, S. M. & Reid, L. M. Laminin as a substrate for retinal axons in vitro. *Dev. Brain Res.* **12**, 136-140 (1984).

- 160 Adler, R., Jerdan, J. & Hewitt, A. T. Responses of cultured neural retinal cells to substratum-bound laminin and other extracellular matrix molecules. *Dev. Biol.* **112**, 100-114 (1985).
- 161 Gavrieli, Y., Sherman, Y. & Ben-Sasson, S. A. Identification of programmed cell death in situ via specific labeling of nuclear DNA fragmentation. *J. Cell Biol.* **119**, 493-501 (1992).
- 162 Negoescu, A. *et al.* In situ apoptotic cell labeling by the TUNEL method. *J. Histochem. Cytochem.* **44**, 959-968 (1996).
- 163 Messerli, M. A. & Graham, D. M. Extracellular Electrical Fields Direct Wound Healing and Regeneration. *Biol. Bull.* **221**, 79-92 (2011).
- 164 McCaig, C. D., Rajnicek, A. M., Song, B. & Zhao, M. Controlling Cell Behavior Electrically: Current Views and Future Potential. *Physiological Rev.* **85**, 943-978 (2005).
- 165 Zhao, M., Forrester, J. V. & McCaig, C. D. A small, physiological electric field orients cell division. *Proc. Natl. Acad. Sci.* **96**, 4942-4946 (1999).
- 166 Ventre, M., Causa, F. & Netti, P. A. Determinants of cell-material crosstalk at the interface: towards engineering of cell instructive materials. *J. Roy. Soc. Interface* **9**, 2017-2032 (2012).
- 167 Gautam, V., Rand, D., Hanein, Y. & Narayan, K. S. A Polymer Optoelectronic Interface Provides Visual Cues to a Blind Retina. *Adv. Mater.* DOI: 10.1002/adma.201304368 (2013).
- 168 Gautam, V. Studies on Semiconducting Polymer-Electrolyte and Conducting Polymer-Retinal Tissue Interfaces. *M.S. Thesis, JNCASR* (2010).
- 169 Srivastava, N. *et al.* Neuronal Differentiation of Embryonic Stem Cell Derived Neuronal Progenitors Can Be Regulated by Stretchable Conducting Polymers *Tissue Eng. A* **19**, 1984-1993 (2013).